EVEN SPIN-PARITY $K\bar{K}$ SYSTEMS

by

DAVID MARSHALL WEBSDALE

A Thesis submitted

for the Degree of

Doctor of Philosophy

in the

University of London

Department of Physics,

Imperial College,

London, S.W.7.

December, 1966.

ABSTRACT

This thesis is an account of an experiment performed at the CERN proton synchrotron. More than 2,600 reactions of the type

$$\pi^- + p \longrightarrow K^o + \bar{K}^o + n$$

and 130 of the type

$$\pi^- + p \longrightarrow \Lambda + \bar{\Lambda} + n$$

were detected in a magnet spark chamber.

The apparatus and its performance are described. Problems specifically related to the automatic measurement of spark chamber photographs, and their geometrical and kinematic analysis, are discussed.

Emphasis is placed on the physical interpretation of the $K_1^o K_1^o n$ final state; in particular on the peripheral production and decay correlations of the S^*, f_o, A_2 and f' mesons.

From a study of the $\Lambda\bar{\Lambda}$ system in $\Lambda\bar{\Lambda}n$ final states there is no evidence to indicate the production of a heavy boson.

CONTENTS

ABSTRACT page 2

PREFACE 7

Chapter 1. INTRODUCTION 8

1.1 The $K\bar{K}$ system 8

1.2 $K\bar{K}$ states within SU(3) 11

1.3 Phenomenology of high energy inelastic collisions 13

Resonances 13

The Peripheral Model 18

Resonance production and decay 21

1.4 Devices used for the detection of particle interactions 23

Chapter 2. THE MAGNET SPARK CHAMBER SYSTEM 26

2.1 Beam, beam chambers and counter telescope 26

2.2 Target and anticoincidence system 28

2.3 Counter logic 30

2.4 Magnet 33

2.5 Magnet spark chamber 33

Construction 33

Operation 35

Time resolution and track recording efficiency 36

2.6 The optical system 37

Chapter 3. ANALYSIS OF DATA page 49

3.1 Scanning 49

3.2 The flying spot digitiser 50

3.3 Spatial reconstruction of an event 52

Optical distortions 52

Systematic errors resulting from spark displacement 54

Apex reconstruction 55

Beam reconstruction and interaction in the target 57

3.4 Kinematics 59

The fitting procedure 59

Hypothesis testing 61

Error assignment 65

3.5 Statistical analysis 66

Chapter 4. EXPERIMENTAL RESOLUTION 73

4.1 Introduction 73

4.2 Spatial resolution 73

4.3 Momentum resolution 74

4.4 Summary 77

Chapter 5. EVENT SELECTION, BIASES AND THE EVALUATION OF TOTAL CROSS SECTIONS 81

5.1 Introduction 81

5.2 Event selection 82

5.3 Bias and contamination in the kinematic fit 83

page

5.4 Corrections for biases and losses from HPD measurements 85

5.5 The detection efficiency 87

The fiducial volume and biases introduced by the counter geometry 87

Absorption of K^o and $\overline{K}^o$ 88

Absorption of neutrons 91

Absorption of beam in the target 91

5.6 The weight of an event 92

5.7 Total cross sections 94

Chapter 6. RESONANCE PRODUCTION IN $K_1^oK_1^o$ FINAL STATES 109

6.1 Introduction 109

6.2 Background 112

6.3 The broad enhancement at ~ 1300 MeV 114

Kinematic effects 114

A fit to the data of Breit-Wigner peaks 116

6.4 The f_o meson 121

6.5 The A_2 meson 126

6.6 An enhancement at 1435 MeV (E ?) 130

6.7 The enhancement close to threshold : S^* 132

6.8 The f' meson 135

SUMMARY 138

APPENDICES page 157

1. The Maximum Likelihood 157

2. The Spin Density Matrix 158

3. The Peripheral Model 159

4. Decay Angular Distributions of $J = 0$ and 2 Resonances 162

ACKNOWLEDGEMENTS 164

REFERENCES 165

PREFACE

This thesis describes one of a series of experiments performed at CERN between 1962 and 1966. I have tried to present a complete report of the experiment. Inevitably the work of many people with whom I collaborated is included; this explains the very brief descriptions of the logic circuitry and anticoincidence counters. I have emphasised those features of the magnet spark chamber system with which I was directly involved, namely the construction, operation and performance of the chambers and the development of a series of computer programmes for the geometrical and kinematic analysis of the photographs. The physical interpretation of neutral final states produced in pion-proton interactions, which provides the material for the last two chapters, has been my own work.

CHAPTER 1

INTRODUCTION

1.1 The $K\bar{K}$ system

The physics of elementary particles is a study of matter and its interactions - not only of those particles observed in classical phenomena but of matter in all its forms. This thesis considers only one aspect of the subject, the hadrons and their strong interactions. Although the nucleon and the pion appear, at a first glance, to be the most important hadrons, they occupy no privileged position in present ideas on the classification of strongly interacting matter. We have no reason, therefore, to suppose that a detailed study of any one particular system should be more profitable than any other in establishing an understanding of matter. We have studied the $K\bar{K}$ system.

The object of this introductory section is to show that the system which consists of a K meson together with a $\bar{K}$ meson exhibits some unique features, particularly with respect to the correlations which exist between its quantum numbers. We shall first consider the effect of isotopic-spin symmetry.

The K meson and its antiparticle will be represented by spinors

$$|K\rangle = \begin{pmatrix} K^+ \\ K^o \end{pmatrix} \quad ; \quad |\bar{K}\rangle = \begin{pmatrix} \bar{K}^o \\ -K^- \end{pmatrix}$$

The $K\bar{K}$ system can exist in states with $I = 0$ or 1. We may write for the $I = 1$, $I_3 = 1$ states:

$$|I = 1, I_3 = 1\rangle = \frac{1}{\sqrt{2}} (|K_a^+ \bar{K}_b^o\rangle \pm |\bar{K}_a^o K_b^+\rangle)$$

Where K_a^+ refers to a K^+ with momentum $\underline{a}$ etc.

From this state the $I_3 = 0$ states are generated by applying the lowering operator

$$T^- = \tau_-^a + \tau_-^b$$

$$|I = 1, I_3 = 0\rangle^+ = \tfrac{1}{2}(|K_a^o \bar{K}_b^o\rangle - |K_a^+ K_b^-\rangle - |K_a^- K_b^+\rangle + |\bar{K}_a^o K_b^o\rangle)$$

$$|I = 1, I_3 = 0\rangle^- = \tfrac{1}{2}(|K_a^o \bar{K}_b^o\rangle - |K_a^+ K_b^-\rangle + |K_a^- K_b^+\rangle - |\bar{K}_a^o K_b^o\rangle)$$

and the orthogonal states with $I = 0$ are

$$|I = 0, I_3 = 0\rangle^+ = -\tfrac{1}{2}(|K_a^o \bar{K}_b^o\rangle + |K_a^+ K_b^-\rangle + |K_a^- K_b^+\rangle + |\bar{K}_a^o K_b^o\rangle)$$

$$|I = 0, I_3 = 0\rangle^- = -\tfrac{1}{2}(|K_a^o \bar{K}_b^o\rangle + |K_a^+ K_b^-\rangle - |K_a^- K_b^+\rangle - |\bar{K}_a^o K_b^o\rangle)$$

States $|\ \rangle^{+(-)}$ are symmetric (antisymmetric) with respect to the exchange of charge variable, i.e. of even (odd) C parity.

The K^o and $\bar{K}^o$ are observed, not directly, but through the weak decays of the CP eigenstates K_1^o and K_2^o.

$$K^o = \frac{1}{\sqrt{2}} (K_1^o + i K_2^o)$$

$$\bar{K}^o = \frac{1}{\sqrt{2}} (K_1^o - i K_2^o)$$

(The recently discovered CP violation is a very small effect ; it is not considered here.)

The decay of the neutral $K\bar{K}$ system is observed, therefore, as

$$|1, 0\rangle^{+} = \tfrac{1}{2}(|K_1^0K_1^0\rangle + |K_2^0K_2^0\rangle - |K^+K^-\rangle - |K^-K^+\rangle)$$

$$|1, 0\rangle^{-} = \tfrac{1}{2}(i\,|K_2^0K_1^0\rangle - i\,|K_1^0K_2^0\rangle - |K^+K^-\rangle + |K^-K^+\rangle)$$

$$|0, 0\rangle^{+} = -\tfrac{1}{2}(|K_1^0K_1^0\rangle + |K_2^0K_2^0\rangle + |K^+K^-\rangle + |K^-K^+\rangle)$$

$$|0, 0\rangle^{-} = -\tfrac{1}{2}(i\,|K_2^0K_1^0\rangle - i\,|K_1^0K_2^0\rangle + |K^+K^-\rangle - |K^-K^+\rangle)$$

It is seen that $K_1^0\,K_1^0$ and $K_2^0\,K_2^0$ result only from the decay of $C = +1$ systems and $K_1^0\,K_2^0$ only from $C = -1$ systems.

Since the relative intrinsic parity of a boson anti-boson pair is positive the requirement of Bose statistics, that states are symmetric under exchange of the two particles, implies:

$$C\,(-1)^J = +1$$

i.e. for $K_1^0\,K_1^0$ and $K_2^0\,K_2^0$

$C = +1$

$J^P = 0^+,\ 2^+,\ 4^+,\ \ldots$

$G = (-1)^I$

and for $K_1^0\,K_2^0$

$C = -1$

$J^P = 1^-,\ 3^-,\ 5^-,\ \ldots$

$G = (-1)^{I+1}$

This thesis describes an experiment in which $K^0\,\bar{K}^0\,n$ final states are produced in $\pi^- - p$ collisions. Only the short lived components of the $K^0\bar{K}^0$ system decay in the detector. By requiring the observation of $K_1^0\,K_1^0$ the detector, a magnet spark

chamber, can project out the $K\bar{K}$ states of even spin, positive parity and $G = (-1)^I$.

1.2 $K\bar{K}$ states within SU(3)

Since 1960 there has been a prolific increase in the population of the so called elementary particles; states, defined by a unique set of quantum numbers, with mean lifetimes comparable or longer than the nuclear 'year' $\sim 10^{-23}$ seconds. The present status of these particles can be assessed from the tables which are regularly compiled.[1] Most of these particles have been successfully accommodated within representations of the unitary group SU(3).[2,3] Our interest in the $K\bar{K}$ states narrows the field to those representations of SU(3) with the allowed spin-parity, 0^+, 1^-, 2^+, 3^- etc.

The 1^- nonet (the vector mesons) is composed of $K^*(890)$, ρ, ω and ϕ, all well established particles. Every non-strange member can, in principle, exist as a $K\bar{K}$ state but only the ϕ is of sufficient mass for the decay into $K\bar{K}$ to be allowed energetically. With $J^P(\phi) = 1^-$ the $K\bar{K}$ has negative C parity and the decay is observed as $K_1^o K_2^o$ and K^+K^- in the ratio 1:1 (the ratio is slightly distorted by the $K^\pm$, K^o mass difference).

It is generally accepted that the nonet of 2^+ mesons is composed of $K^*(1400)$, A_2, f_o and f', although there remain some doubts concerning the spin-parity assignments of the A_2; these are

discussed in Chapter 6. The $K\bar{K}$ decay of each non-strange member is energetically permitted, and the positive C parity states $K_1^o K_1^o$, $K_2^o K_2^o$ and K^+K^- appear in the ratio 1:1:2. The $K\bar{K}$ decay modes of these particles compete with the pionic decays. Only in the decay of the f' does the $K\bar{K}$ mode dominate. The branching ratios can be predicted from SU(3). Each member of the 2^+ nonet decays into either two pseudoscalars or a vector and pseudoscalar. These two couplings can be calculated from any $2^+ \rightarrow 0^- 0^-$ and $2^+ \rightarrow 1^- 0^-$ decay rate.[4]

There is some evidence for a scalar, 0^+, nonet. The particles which can be assigned to this representation are $\varkappa(727)$,[5] S_1 (the I = 1, $K\bar{K}$ threshold enhancement[6]), S_o[7] and S^*. None of these particles could be classed as established. The S_o has been predicted to explain an asymmetry in the ρ^o decay angular distribution, though not observed directly. Its mass lies below the $K\bar{K}$ threshold. The S_1 may be a strong s-wave attraction and not a definite particle. The S^* is observed in this experiment.

No clear evidence exists for representations with $J^P = 3^-, 4^+$ etc. nor for higher representations than the singlet and octet. In conclusion, our analysis of $K_1^o K_1^o n$ final states must consider the possible contribution from f_o, A_2, f', S_1 and S^*.

1.3 Phenomenology of high energy inelastic collisions

Resonances

The use of high energy accelerators and the associated development of techniques in the field of particle detectors (notably the bubble chamber) has been responsible for the discovery of the particles mentioned in the previous section and of another hundred or more whose existence, before the beginning of this decade, was not even suspected.

Except for the η and the Ω^- all the 'new' particles have a mean life $\sim 10^{-23}$ seconds, consistent with decay via the strong nuclear interaction. During one mean lifetime the distance travelled by such particles is too small to be observed directly; e.g. a 7 GeV/c ρ meson with $\gamma = E/m \sim 10$ will have a mean path length in the laboratory $\sim 3 \times 10^{-12}$ cm. In the discussion which follows we shall describe how those particles were originally discovered and some methods employed in their identification.

The nucleon and hyperon isobars reveal themselves as a peak in meson-nucleon scattering cross sections plotted as a function of the total centre of mass energy. The peak suggests a resonance phenomenon. In the case of purely elastic scattering the effect is formally identical with a classical resonance in the sense that the phase shift appropriate to the spin of the isobar passes through 90°. The distinction between the words resonance and particle (a system of definite quantum numbers which can exist beyond the range of the

nuclear force) is blurred in the case of most strongly decaying systems. Both terms are recognised and interchangeable.

The peaks found in an experiment of this type result from the formation of resonances in the intermediate state. A formation experiment will not, however, reveal a meson resonance (direct meson-meson scattering is not yet a practical proposition). The meson resonances are found in 'production' experiments.

The cross section for an inelastic collision between a meson and a target nucleon

$$m + N \rightarrow N + m_1 + m_2 + \ldots.$$
$$\text{is } \sigma \sim |T|^2 \rho\ (E, m_1, m_2 \ldots.)$$

T is the matrix element for the transition from the initial to the final state;

ρ , the density of states factor, is the total volume in momentum space available to the particles in the final state. It is a function of the total energy of the system, E, and the masses of the individual particles in the final state.

Matrix elements, calculated according to the Feynman rules, are Lorentz invariant. Since the cross section is independent of a frame of reference ρ will also be a Lorentz invariant.

In general the matrix elements for transitions caused by strong interactions are unknown. The simplest assumption, the Statistical Model,[8] uses a matrix element independent of the momenta of the

particles in the final state. In this case the transition rate and the final state momentum distribution are described by the phase space factor alone.

If Q is the total four momentum of an n particle system[9)]

$$\rho_n(E) = \int \prod_{i=1}^{n} d^4q_i \, \delta(q_i^2 - m_i^2) \, \delta^4\left(\sum_{i=1}^{n} q_i - Q\right) \qquad \ldots(1.1)$$

The δ-functions impose energy-momentum conservation and the constraint on m_i such that

$$m_i^2 = E_i^2 - \underline{p}_i^2$$

We shall define the 'effective mass' of a system of k particles selected from an n body final state

$$M_k^{n2} = \left(\sum_{i=1}^{k} q_i\right)^2 = \left(Q - \sum_{i=K+1}^{n} q_i\right)^2 \quad \ldots. (1.2)$$

The expression $P(\mu) = \dfrac{d\rho_n}{d M_k^n}$ .... (1.3)

is the probability distribution for the effective mass of the k particle subsystem having the value μ. It will be referred to as the phase space distribution, i.e. the effective mass distribution expected from the statistical model. Any deviation from phase space of an experimental mass distribution implies a 'structure' in T and dynamic features of the interaction are indicated.

In a two particle final state the phase space distribution

reduces to a δ-function. This is a trivial result; it simply states that the mass of one of the two particles, m_1 say, has the value m_1. In a three particle final state of total energy E the effective mass of particles 1 and 2 is obtained by integrating (1.1)

$$P(\mu) = \frac{d\sigma}{dM_{12}} = \frac{2\mu\pi}{2\mu^2}\left\{[\mu^2 - (m_1 + m_2)^2][\mu^2 - (m_1-m_2)^2]\right\}^{\frac{1}{2}}$$

$$\times \frac{\pi}{2E^2}\left\{[E^2 - (m_3 + \mu)^2][E^2 - (m_3-\mu)^2]\right\}^{\frac{1}{2}}$$

This is a continuous distribution in μ between the kinematic limits

$$\mu_{min} = m_1 + m_2 \quad \text{(threshold)}$$

$$\text{and} \quad \mu_{max} = E - m_3$$

Similar expressions for more complex final states are obtained by means of recursion relations[9] which can be set up for the evaluation of (1.1). Deviations from these expressions, in the form of peaks superimposed on the continuous distribution, are frequently observed. The peak suggests a preference of the k particle sub-system to emerge from the interaction with a definite effective mass; a situation which is similar to the δ-function obtained in a two body final state distribution. If these peaks possess a definite set of quantum numbers they are called resonances and are parametrised by their mass M and width Γ. The width of

the resonance is related through the uncertainty principle to its mean life. A natural width of about 100 MeV/c^2 is characteristic of a decay via strong interactions.

To illustrate the effect we consider a specific three body final state. At 3 GeV/c incident momentum the reaction

$$K^+ + p \rightarrow K^o + \pi^+ + p \qquad 10)$$

exhibits a resonance, K^{*+}, in the $K^o\pi^+$ effective mass distribution and a resonance, N^{*++}, in the $p\,\pi^+$ effective mass distribution. More information is contained in the 'Dalitz-Plot'. This is a two dimensional plot of $M_{K\pi}$ against $M_{p\pi}$. The statistical model ($T \equiv 1$) predicts a uniform population within the kinematic boundary. A resonance appears as a concentration of events along a band centred at the resonance mass. In the above reaction the population of the Dalitz plot is very nearly completely confined to the two resonance bands and one refers to such a process as a quasi-two-body reaction:

$$K^+ + p \rightarrow K^{*+} + p \qquad \ldots\ldots (1.4a)$$

$$K^+ + p \rightarrow N^{*++} + K^o \qquad \ldots\ldots (1.4b)$$

By excluding those events from the overlapping bands of the Dalitz plot a pure sample of reaction (a) or (b) is obtained. This is a very 'clean' process. It will be seen that in the $K^o\bar{K}^o n$ final states described in this thesis the quasi-two-body r reactions are not so clearly defined.

The Peripheral Model

Inelastic collisions at incident momenta greater than 1 GeV/c exhibit two characteristic features. There is a tendency to proceed to the final state via the production of resonances, as described above, and secondly there is a preferential grouping of the secondaries in the forward-backward direction of the centre of mass system.

The collision can be pictured in terms of the interaction of an incident particle with the 'meson cloud' of the target nucleon, rather than with the nucleon itself. The directions of the secondary particles are not changed very much from the original direction of the incident primaries. These ideas are expressed quantitatively in terms of the peripheral model. The meson cloud interaction is represented by the exchange of a virtual particle. The lighter the particle, the longer the range of the interaction and the more peripheral the collision. In the Feynman diagram below a particle 'a' incident on a target 'b' produces two systems of secondaries, c and d. The interaction proceeds via the exchange of a particle 'e'.

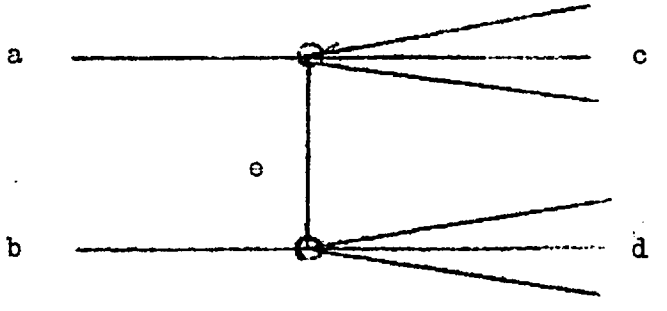

The fundamental parameter in such a diagram is the squared four-momentum transfer

$$t = (p_c - p_a)^2 = (p_d - p_b)^2$$
$$= (M_a^2 + M_c^2) - 2\,(E_a E_c - p_a p_c \cos\theta^*)$$

t can be interpreted as the square of the virtual mass of the exchanged particle. θ^* is the centre of mass scattering angle.

The matrix element for the process is obtained from the Feynman rules

$$T = V_{aec}(t)\ \frac{1}{M_e^2 - t}\ V_{bed}(t) \qquad \ldots\ (1.5)$$

where M_e is the physical mass of the exchanged particle. The vertex factors are related to the matrix elements for the physical processes

$$c \longrightarrow a + e$$

$$d \longrightarrow b + e$$

which, if c and d are particles (or resonances) with definite quantum numbers, can be written down explicitly. This is the Born-Term Model.

The dependence of the matrix element on the propagator will give a maximum in the differential cross section as $-t$ falls to its smallest value in the physical region (i.e. $\cos\theta^* = 1$). In this way the peripheral model accounts for the characteristic forward-backward peaking. The success is, however, only qualitative. The experimental differential cross sections of two body and

quasi-two-body reactions have exhibited a peaking stronger than that predicted by a matrix element of the form given by (1.5).

The Absorption Model, as developed by Sopkovich,[11] Gottfried and Jackson,[12] is a refinement to the peripheral model which has had some success in quantitatively explaining high energy collisions.

At high energies many inelastic channels are open to the final state. They all contribute to the total inelastic cross section. The quasi-two-body processes in particular must be regarded as being in competition with the other 'absorptive channels'. Intuitively one might expect the absorptive effects to be stronger when the incident particles are close together in the collision. Thus small impact parameter collisions leading to quasi-two-body final states are absorbed. This effectively means that: (a) the reaction cross section is reduced and that; (b) the low angular momentum partial waves in the scattering process are suppressed. It is these waves which lead to the high t values in the angular distribution. (S-wave scattering is isotropic in cos θ^*). This argument explains qualitatively how the peripheral model can be modified to agree with the experimental data. The theoretical formulation is based on the following diagram.

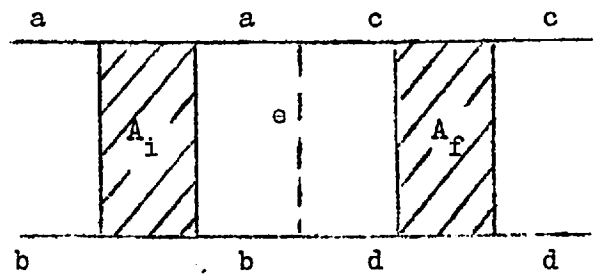

The absorptive effects are introduced by initial and final state interactions A_i and A_f. The parameters of the 'absorbing discs' would be completely determined from a knowledge of the diffraction scattering between a and b and between c and d. In general it is only the former which can be measured experimentally. For lack of better the final state absorption parameters are assumed equal to those in the initial state. Precisely how the Born-Term partial waves are modified by the diffraction scattering is shown in Appendix 3 where we have written down some of the useful results necessary in a quantitative comparison between theory and experiment.

Resonance Production and Decay

This section, together with the Appendices, contains a discussion of the angular correlations exhibited in the decay of resonances and their relation to the mechanism of the production process and to the spin and parity of the resonance.

We assume that 'c' is a resonance of spin J. In general it will be produced in a mixture of pure spin states. This mixture is defined by the spin density matrix (see Appendix 2), whose elements $\rho_{mm'}$ (m, m' run from $-J$ to $+J$) will depend on the spin and parity of the exchanged particle. From the decay angular distributions of c we can infer something of the mixture of spin states of c and hence of the quantum numbers of the exchanged

particle.

The specific examples relevant in this thesis, namely the decay of resonances with $J^P = 0^+$ or 2^+ into two 0^- particles (K mesons) are treated in Appendix 4. Without going into any algebra we can examine the density matrix of c when it is produced in a one pion exchange Born-Term Model. Suppose $J^P(c) = 2^+$. Then in the rest frame of c

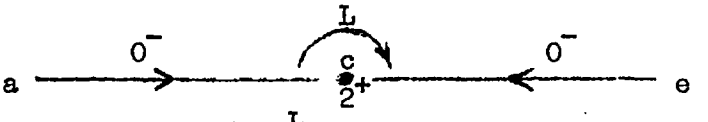

parity conservation: $(-1)^L$ is even and if we choose the quantisation axis parallel to the incident direction $\underline{a}$

$$L = 2 \quad \text{with} \quad L_z = 0$$

i.e. none of the spin states for c with $m \neq 0$ are populated and the density matrix reduces to

$$\rho_{oo} = 1 \text{ : all other elements are zero.}$$

If the exchanged particle is a vector meson a similar argument gives:

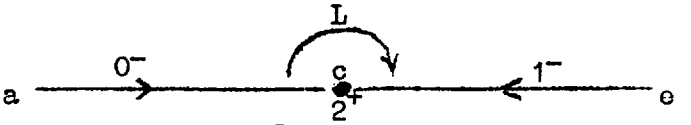

$(-1)^L$ is even

Vectors $\underline{L}$ can be combined with $J_e = \underline{1}$ to give a resultant $J_c = \underline{2}$ as follows:

$$\underline{2} = \underline{L} + \underline{1}$$

$$\text{i.e. } 2 = L + 1,\ L,\ L - 1$$

hence $L = 2$ with $L_z = 0$

Conservation of the z component gives $m = 0$ or ± 1 but only the states $|1, \pm 1>$ can couple with the orbital $|2, 0>$ to produce the final state $|2, \pm 1>$ for c; the state $|1, 0>$ can not couple with $|2, 0>$ to give the state $|2, 0>$ for c. It follows that $|m = 0, 2>$ do not occur in the mixture and

$$\rho_{11} = \rho_{-1,-1} = \tfrac{1}{2}$$

and all others except $\rho_{1,-1}$ are zero.

These results were obtained using the Born-Term Model. The inclusion of absorption modifies slightly the predictions. That some difference should be expected can be seen from the fact that neither the rest system of c after the final state interaction A_f nor the direction of a before the initial state interaction A_i are the same as those defined at the meson vertex aec.

1.4 Devices used for the detection of elementary particles

It is not intended here to describe the many and varied types of detector of high energy particles. An up-to-date review of this subject can be found in the article of J.A. Newth.[13]

The devices most suited to accelerator work are the bubble chamber, spark chamber, scintillation counter and Cerenkov counter. The bubble chamber records, with high spatial resolution, all the particle trajectories associated with an interaction. Its scope,

in terms of the complexity of events which can be recorded and identified, is practically unlimited. The limitation of the technique is that the chamber must be made sensitive before the particles interact in it. The study of a rare interaction would necessitate the taking of large numbers of photographs followed by a lengthy scanning and measurement programme.

The pure counter experiments can handle many events in a short time. Problems of identification limit their use to the recording of very simple events. The elastic scattering experiments, with a direct computer link, of Lindenbaum et al.[14] are an example of this technique at its best.

The spark chamber, used in conjunction with counters, improves considerably on the spatial resolution of the counter and it can be made sensitive after the particles have traversed it. Used in this way a spark chamber, if it can be devised to select a particular type of event, will provide results more rapidly than a bubble chamber.

The detector which is described in the following chapter is a magnet spark chamber. It retains all the advantages of the conventional spark chamber but is operated in a magnetic field. The configuration is identical with that of the bubble chamber, and complex events can be identified. Although the intrinsic spatial resolution of this chamber is worse than that of a bubble

chamber the momentum precision is comparable with that of the largest modern hydrogen chambers. This is achieved by employing a low density of material in a spark chamber of large dimensions.

The rare interactions studied with this device include:

$$\pi^- + p \rightarrow K_1^o + K_1^o + n$$

$$\pi^- + p \rightarrow \Lambda + \bar{\Lambda} + n$$

$$K^- + p \rightarrow \bar{K}^o + n$$

$$\bar{p} + p \rightarrow \bar{n} + n$$

$$\bar{p} + p \rightarrow \bar{\Lambda} + \Lambda$$

All the events were recorded using the same experimental set up. The information on the photographs has been digitised by an automatic measuring device. This procedure will eventually be replaced by directly digitising the information with the aid of wire spark chambers, allowing a more rapid rate of data collection.

It is probable that the magnet spark chamber, coupled with new developments in the field of super-conducting magnets, magneto-strictive wire chambers and high speed on-line computers, will be one of the more important detection systems to be used at accelerators of the present and following generations.

CHAPTER 2

THE MAGNET SPARK CHAMBER SYSTEM

2.1 Beam, beam chambers and counter telescope.

The beam was produced from an internal target of the CERN proton synchrotron (PS), operating at 18.1 GeV/c. An angle of 80 milliradians to the circulating beam was chosen to yield a high flux of kaons and antiprotons (though not required for the experiment described in this thesis). The layout is shown in Figure 2.1.

The three 1 metre bending magnets are adjusted to give the same mean bending angle at each energy. In conjunction with the thin foil spark chambers $Sp_{1..5}$ (Fig.2.2) they are used to determine the beam momentum with a precision better than that given by the momentum slit, $\pm 1\frac{1}{2}$ % . From measurements of the beam particle in each of the spark chambers the bending angle (hence momentum) and trajectory can be calculated. It was foreseen that ambiguities of identification from two stereo-views might occur when more than one beam track appeared. To resolve this problem mirrors were fixed at 30° and 45° to the chamber giving, in addition to perpendicular stereoscopy, a third view.

Two threshold Cerenkov counters of the Vivargent type[15] effected

velocity selection of the beam particles. C_1 was filled with hydrogen and its pressure adjusted, so that kaons and antiprotons of a given momentum did not have a velocity high enough to produce Cerenkov light ; the pion velocity at this same momentum is, however, sufficient. Similarly C_2 was filled with ethylene and its pressure adjusted to give a threshold between kaons and antiprotons.

The signatures of pions, kaons and antiprotons are then, C_1C_2 , $\bar{C}_1C_2$ and $\bar{C}_1\bar{C}_2$ respectively. The measured rate in the 'improper' condition $C_1\bar{C}_2$ was less than 10^{-6} of the rate C_1C_2 , an indication of the particle distinction reliability. The proportion of π^- : K^- : $\bar{p}$ in the beam was as follows.

At 5 GeV/c	1 :	.0045 :	.0049
7 GeV/c	1 :	.0075 :	.0045
12 GeV/c	1 :	.0043 :	.0003

The muon contamination, estimated at 5, 7 and 12 GeV/c was 4 ± 1 %, 3.5 ± 1 % , 2.5 ± 1 % . These figures are extrapolated from the DISC (a differential Cerenkov counter) measurements at high energy of Duteil and others[16].

The four 1 cm scintillation counters $S_{1...4}$ ensure that a beam particle passes through both Cerenkov counters avoiding misidentification. Two 2 mm counters S_5 and S_6 define a narrow pencil which enters the target and does not hit the walls. S_6, placed inside the vacuum case of the target, reduces background interactions produced in the mylar windows. Particles scattered after S_4 , for example in the beam chambers, might

still give a signal if they passed through the perspex light guides of S_5 and S_6 producing Cerenkov light. The anticounters $\bar{A}_{1...4}$ reduced this.

The telescope $S\bar{A}$ defines an acceptable beam free from background. The momentum slit S' allowed a total beam flux of 1.7×10^5 particles per burst of which 1.2×10^5 passed through the telescope.

2.2 Target and Anticoincidence system

We are interested in the decay and production of $K\bar{K}$ states. The models introduced in the analysis of the production process require the details of the target particle to be defined. A liquid hydrogen target was designed, therefore, to introduce a minimum of interactions with complex nuclei. The H_2 cell was 41 cm long by 6 cm diameter. The end windows of the cell and its vacuum case were formed from .2 mm mylar. The interaction rate in the carbon of the mylar windows is estimated to be no more than 2 % of that in the target liquid.

The two main purposes of the anticoincidence shield are incompatible. To exclude the high background of interactions in which charged particles and π^o's are produced the ideal system would consist of a many layer sandwich of thin lead plates and scintillator. Such a system, with good gamma ray detection efficiency, must contain a large quantity of material and does not satisfy the second requirement. The neutral particles produced, kaons, lambdas or neutrons should neither be scattered in the counters nor lost altogether after some secondary process (collision or decay) in which the products are detected. The counter

shown in Figure 2.3 was a compromise solution to meet this conflict.

The thin 2 mm counter A_5 needs some explanation. At the target centre the fringe field of the magnet was 2 kilogauss. The counters had to be connected by 2.5 metre light guides to the photomultipliers, located where the fringe field was less than 100 gauss. A soft iron shield permitted reliable operation of the photomultipliers, no difference in the counting rate was observed with the magnet on or off. The light collection efficiency was however, low, and in order to reduce background from interactions in the first few millimetres of the F_1 scintillator $\bar{A}_5$ was introduced in the beam line, down stream from the target.

The gamma ray detection efficiency is energy dependent ; a soft shower produced in the lead may be absorbed before reaching the scintillator layer. A Monte - Carlo programme was used to generate gamma rays from the decay of $N^*(1238)$, produced in the hydrogen target at very low momentum transfer. The mean value of the probability that both gammas from the neutral pion escape detection was 6 % .

The detection of neutrons and neutral kaons by the anticoincidence has been discussed by Colin West[17]. It requires that a correction be applied to the total cross section estimates, and since the neutron detection efficiency is energy dependent, the production angular distribution is biased. These factors are considered in Chapter 5.

2.3 Counter Logic

Werner Beusch designed the electronic units used in the trigger logic for this experiment. The design, testing and performance of these units is fully described in his article[18].

The main requirements of the system may be listed :

i) Small overall time delay to minimize the staggering of the sparks and the number of background beam tracks (section 2.5 (iii)).

ii) Flexible system employing standard input and output signals.

iii) Ability to work with counter pulses of large time and pulse height dispersion. The light from the counters, in the magnetic field, had to be guided to photomultipliers through pipes several metres in length : efficient anticoincidence thus requires the detection of small pulses from counters with a high rate of large amplitude pulses.

iv) Possibility to display the nature of the trigger.

The trigger condition for this experiment demanded that a π^- interacted in the target producing no charged secondaries, π^0's nor gamma rays. Furthermore, the neutral secondaries must decay in a charged mode and trigger one of the large counters D or E .

Block diagrams (Figs. 2.4 a,b) show how this condition is realised. The beam telescope logic consists of $S_{1..4}$ in coincidence together with $A_{1..4}$ in anticoincidence. Counter pulses, appropriately delayed are connected to discriminators which produce standard output pulses from an input signal exceeding 0.4 volts. After firing, the output of the discriminator remains at the YES level until it is reset.

The reset is derived from the counter S_3 which arrives some 20 nanoseconds earlier than the signal at each discriminator input. An additive dead-time, applied to the reset generator, ensures that the logic is reset only if no beam particle had preceeded the triggering particle by less than 200 nanoseconds. Although this reduces by 20% the number of events, these would have had the unwanted beam track in the chamber.

The telescope signal, T, is split into three channels and combined with the outputs from the Cerenkovs. The combinations TC_1C_2 , $T\bar{C}_1C_2$, $T\bar{C}_1\bar{C}_2$ indicate π^- , K^- , $\bar{p}$ respectively. The trigger rate with incident π^- was at least ten times that with incident K^- and $\bar{p}$. In order to collect data from K^- and $\bar{p}$ interactions the PS burst was 'rationed'. During the first 80 % of the burst a priority gate was closed on the π^- channel. If no trigger occurred then the gate was opened to allow π^- triggers during the remaining 20 % of the burst time. The signals from the anticounter surrounding the target are added and inverted; those from the E and D counters are added. The combination TC_1C_2 $(E+D)$ $(\bar{R}+\bar{F})$ triggers the spark chamber and camera.

Each discriminator remains in the YES position until reset, allowing the use of 'slow' flip flops to control the display. These are sufficiently stable to weather the electrical storm produced by the spark chambers. The information displayed on the film included

the output from the Cerenkov counters and from the E and D counters.

An event, having satisfied the trigger condition, can be lost if a chance pulse from an anti-counter arrives during the time interval τ_1 (Fig.2.4). Assuming a constant mean rate for the noise pulse of τ_o^{-1} per second the recorded trigger rate is given by

$$N_1 = N_o \; e^{-\tau 1/\tau_o}$$

N_o being the true trigger rate. The loss is calculated by choosing a different time interval τ_2. The sum of the three trigger channels is delayed and compared with the anti-signal $(\overline{R+F})$. In this condition the observed rate is

$$N_2 = N_o \; e^{-\tau 2/\tau_o}$$

from which N_o can be calculated by extrapolating to zero delay.

The delayed trigger provides a monitor for the anticoincidence losses, which are dependent on the running conditions of the PS ; the effective value of τ_o depends on the radio-frequency structure of the burst. This monitor, together with the output from the three telescope channels is recorded via scalars on punched paper tape. Collected at the end of each roll of film this information was used in calculating and correcting the cross section.

2.4. Magnet

A uniform field, superimposed over a large accessible volume, was the main requirement of the spark chamber magnet. The magnet available, designed by Dr. M. Morpurgo for use with a large cloud chamber, has proved very satisfactory. When operated at 2 Megawatts it has a magnetic field of 10.7 kilogauss which is maintained to within 10 % over a volume of 180 x 90 x 90 cm^3. The position of the coils, with respect to the iron yoke (Fig.2.5a) allows good access to the field volume from either end of the magnet. A hole in the upper pole piece permitted photography of a volume 160 x 60 x 80 cm^3. This was the 'useful volume'. The elongated form is suitable for experiments of the type in which secondaries are peaked strongly forward, as is the case in the reactions described in this thesis.

2.5 Magnet Spark Chamber

(i) Construction

The size of the chamber is pre-determined by the useful volume of the magnet. The standard technique of spark chamber construction, namely glueing aluminium foil onto perspex formers, was not used. This system, employed for a large chamber lacks mechanical rigidity; also the sparks must be photographed through a considerable thickness of perspex, requiring good optical surfaces and freedom from bowing.

One 'plate' was made by glueing 25 microns aluminium foil on

each side of a 75 cm sq. 'picture frame' of aluminium bars. The foils were stretched mechanically over the frames during glueing; (Araldite was used, in an oven at a temperature of 60° C). This all aluminium construction is rigid and thermally stable. To prevent electrical breakdown, the edge of the plate was insulated with mylar sheet 1 mm. thick.

Thirteen such plates were separated by 8 mm. perspex spacers and clamped together inside an airtight aluminium box with mylar end windows to reduce scattering. The gaps could be photographed through a glass plate top and, to reduce spurious reflections, the interior of the box was anodised. Six such units comprise the complete chamber. The aluminium foil, mylar windows and neon gas contribute to a total of 1.3 gms/cm^2 of material. This corresponds to a radiation length of 30 metres.

An apparent disadvantage of this system compared with the conventional chamber is the dead space. Each plate is effectively 12 mm. thick compared with the active space of the 8 mm. gap. Since no short or highly curved tracks were expected, however, this was not a serious problem and, as described in Chapter 3, the dead space proves useful in eliminating noise (e.g. film scratches) during automatic measurement.

The plates in each unit are connected alternately to a high

voltage pulser and to earth. A good multiple track efficiency demands a fast rise time of the pulse on the plates. With this in view a spark gap and condenser bank is mounted directly beneath each unit. The assembly is clamped to a steel plate which slides into the magnet on rails. (Figs. 2.5a,b)

This unit system has been used in a variety of experiments involving lead plate chambers, targets and counters inside the magnet. It is very flexible.

(ii) Operation

The high voltage pulse system used for the chamber is shown in Figure 2.6. The slave system consists of a spark gap driving six active plates through a bank of 4000 pf. condensers connected one to each pair of chamber gaps. Each active plate (or pair of gaps) has a capacity of 1200 pf. The spark gaps were operated at 12 kilovolts giving an effective voltage of 9 kilovolts on the plates. The rise time of the pulse was better than 30 nanoseconds and the RC decay time to earth via the 100 ohm resistors .52 microseconds.

The gaps were of very simple construction. A tungsten bolt and a spark plug, in a 2 kg/cm^2 nitrogen atmosphere, provided an adjustable and reliable device.

The slaves are driven by a master of similar construction. This is triggered from the counter logic pulse after it has been amplified with an avalanche transistor and power pentode.

(iii) Time resolution and track recording efficiency

The time resolution of the spark chamber depends upon the DC clearing field applied between the plates. Electro-negative impurities, introduced into the gas are also effective in reducing the sensitive time, although not easily controlled. We used 'clean' gas. An 80 % : 20 % neon-helium mixture was passed at a rate of $\frac{1}{2}$ litre/minute through the chamber. The curves of Figure 2.6 show, for different fields, the sparking efficiency as a function of time delay between the passage of an ionising particle and the application of a high voltage pulse. The minimum overall delay of the system with the full trigger logic was 350 nanoseconds. In order to allow the use of a high beam intensity and at the same time have a minimum number of 'accidental' tracks the clearing field should be adjusted to give a sensitive time of 400 nanoseconds, i.e. $\sim$ 200 volts/cm. Such a large field would produce an excessively high staggering of the sparks; i.e. a lateral displacement of the spark from the particle trajectory in the direction $\underline{E} \times \underline{H}$. This makes the recognition of events very difficult for the human operator.

A clearing field of 60 volts/cm. was used. This produced a 1 mm. staggering on either side of the trajectory and a memory time of 1.5 microseconds.

During the experiment the conditions were as follows:

Beam flux: 1.7×10^5 particles/burst.

Burst time: 250 milliseconds, flat top.

No beam particle to have preceeded the trigger particle by less than 200 nanoseconds, (required by counter logic).

Fifty per cent of photographs contained a background beam track. This is the figure expected with a sensitive time of 1.5 micro-seconds.

The photograph, Figure 2.7, is a typical event showing two V^o decays together with an accidental beam track. The dead space between the gaps is clearly seen and also the higher staggering of the beam track shows that it is 'older' than the V^o's. A sparking efficiency of 98 % for one track and 60 % for seven or eight tracks was maintained throughout the experiment.

2.6. The Optical System

Two stereo views of the chamber were photographed using an optical axis separation of 58 cm; the maximum allowed by the 170×60 cm^2 aperture in the upper pole piece. The path length between lens and beam level was 271 cm. The stereo-constant, relating vertical position Z to a co-ordinate difference ΔY as measured from the two views, is $\lambda = 4.7$.

A matched pair of Symmar objectives (focal length 108 mm) reproduced adjacent images on 70 mm film. The demagnification was twenty four times. The beam chambers were photographed through a

Xenar 500 mm telephoto lens. A system of mirrors, designed to produce equal optical path lengths between each chamber and the tele-objective was used. Their demagnification was x 37.5 and the three views of each small chamber appear on the same film. Film resolution (we used Eastman Plus-x) was no limitation to the accuracy of measurements and the depth of focus using f/11 aperture was adequate.

The photograph (Figure 2.8) shows the format. Along the lower edge is a sequence of digitised information. A frame number and output from the discriminator memories are displayed.

A prism system, in place of the conventional field lens, bends the light rays emitted parallel to the plates into the objective. Perspex prisms of the same mean thickness, one per gap, were machined to the requisite angle and mounted on a flat glass plate fixed to the magnet. A discussion of the systematic distortions of the optical system and their correction appears in Chapter 3.

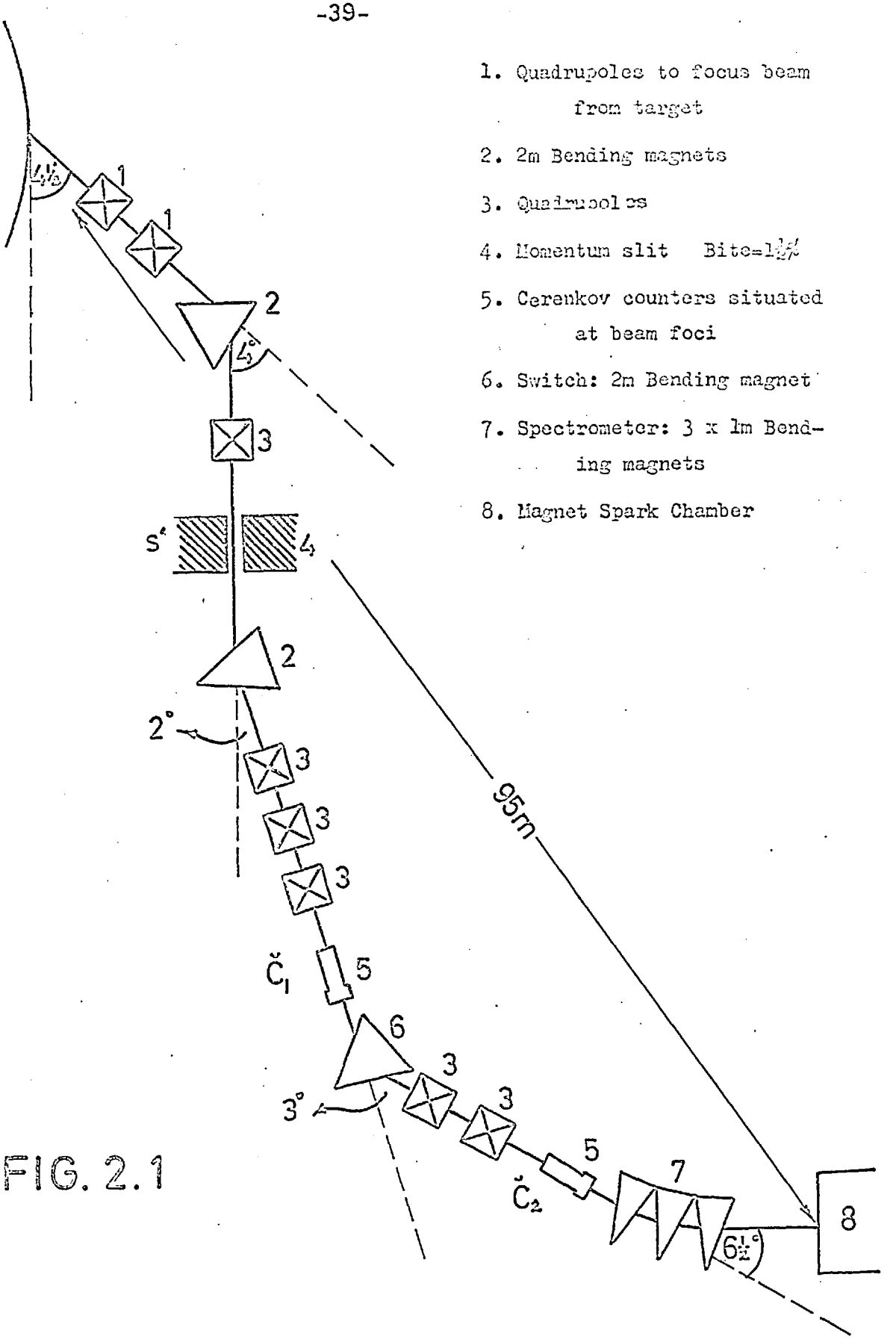
1. Quadrupoles to focus beam from target
2. 2m Bending magnets
3. Quadrupoles
4. Momentum slit Bite=1½%
5. Cerenkov counters situated at beam foci
6. Switch: 2m Bending magnet
7. Spectrometer: 3 x 1m Bending magnets
8. Magnet Spark Chamber
4½°
1
1
2
4°
3
S'
4
2
2°
3
3
3
95m
Č1
5
6
3°
3
3
5
Č2
7
8
6½°

FIG. 2.1

FIG. 2.2

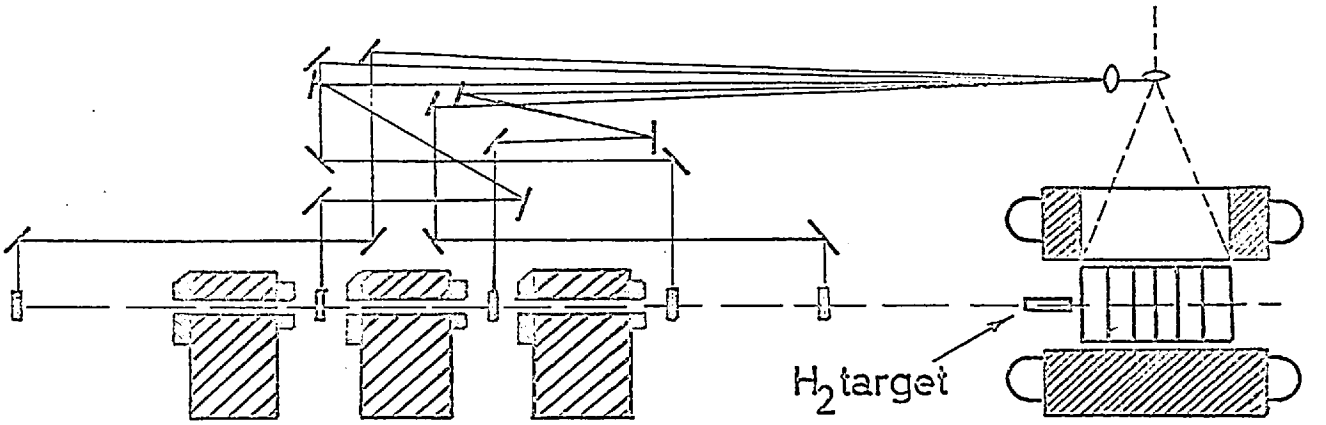

LAYOUT OF THE BEAM DEFINING SPARK CHAMBERS

COUNTER SYSTEM

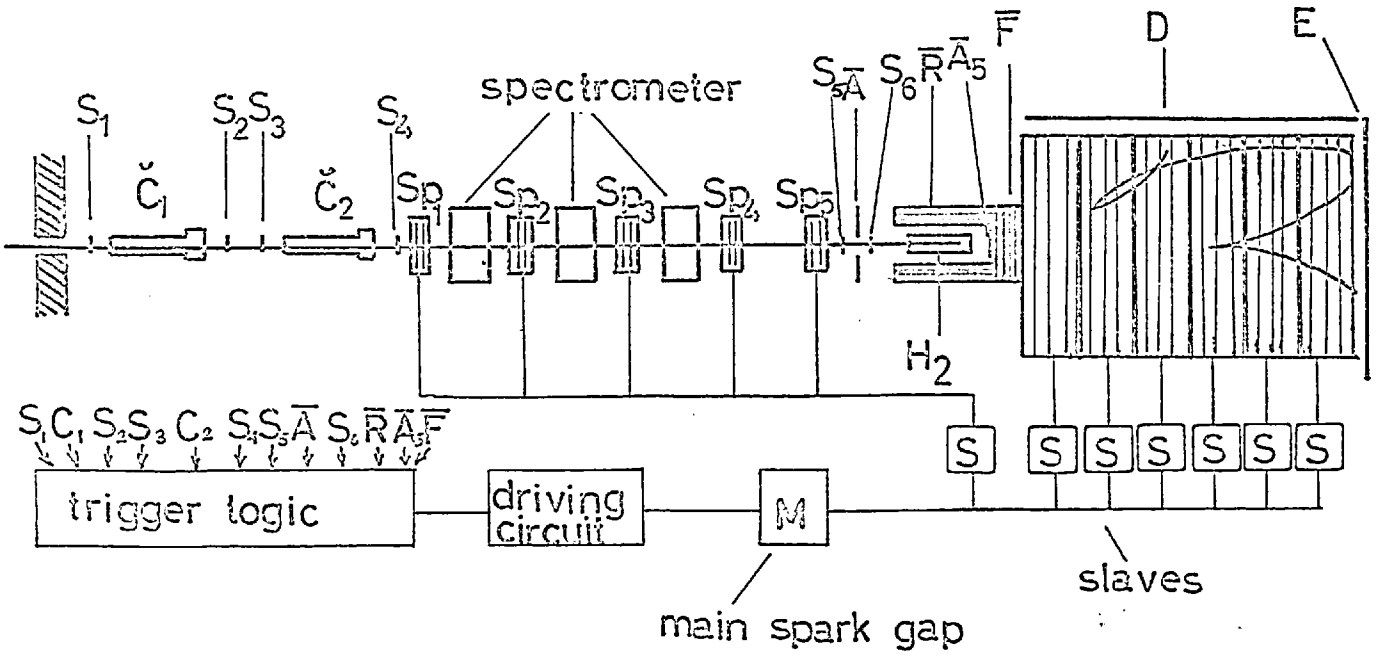

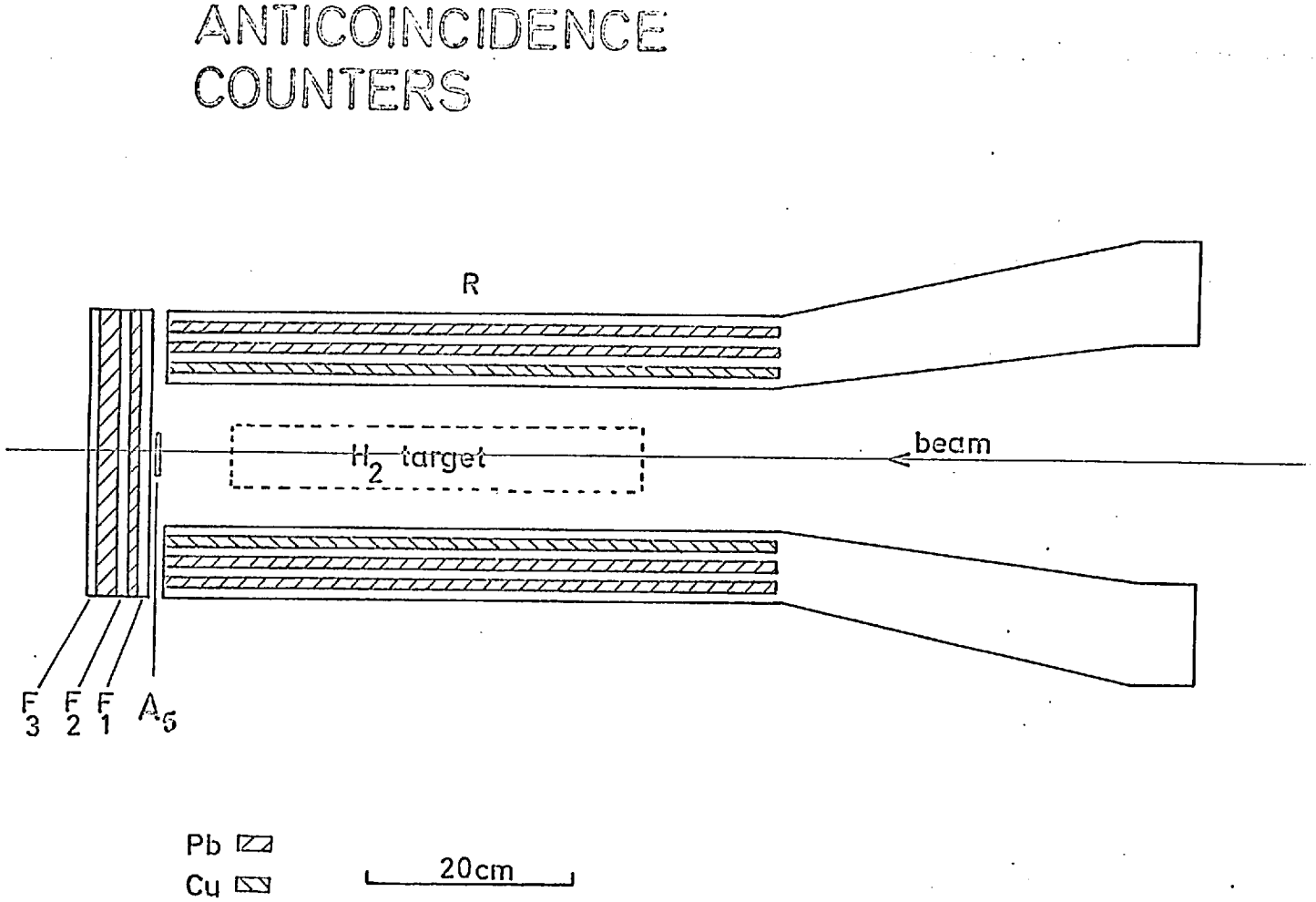
ANTICOINCIDENCE COUNTERS
R
beam
H_2 target
F 3
F 2
F 1
A_5
Pb
Cu
20cm

FIGURE 2.3

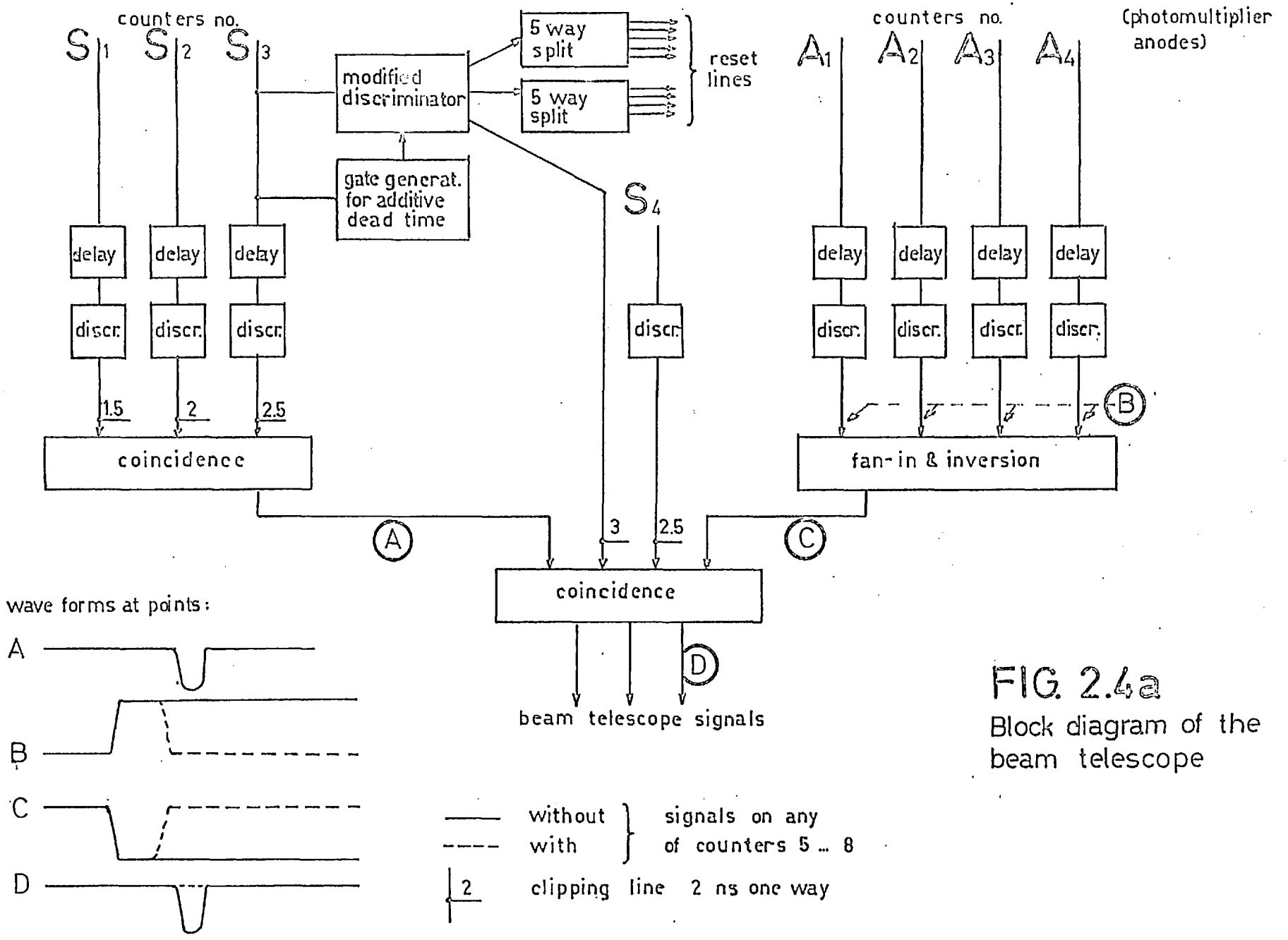

FIG. 2.4a
Block diagram of the beam telescope

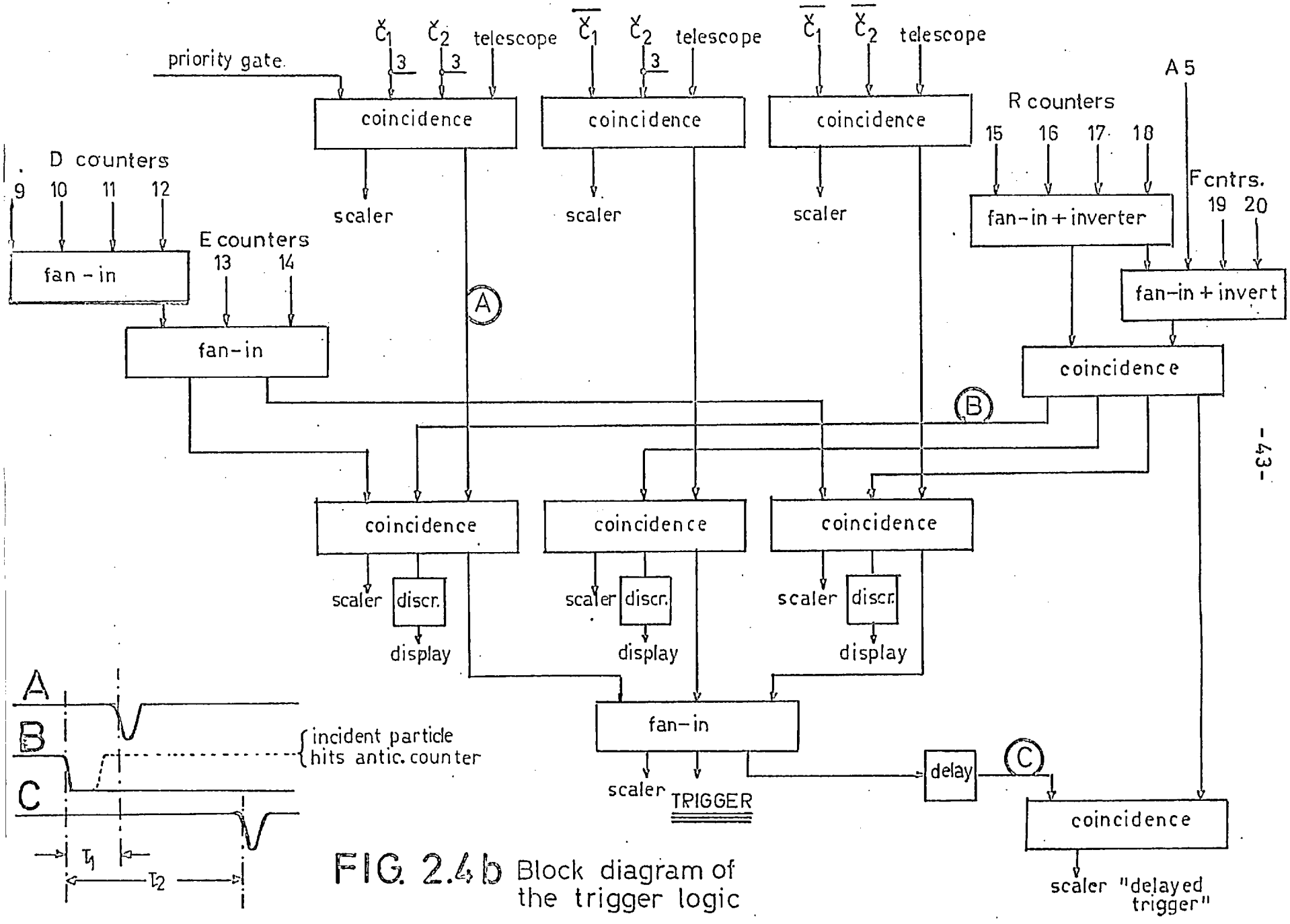

FIG. 2.4b Block diagram of the trigger logic

FIG. 2.5a MAGNET SPARK CHAMBER
SECTION ALONG BEAM DIRECTION

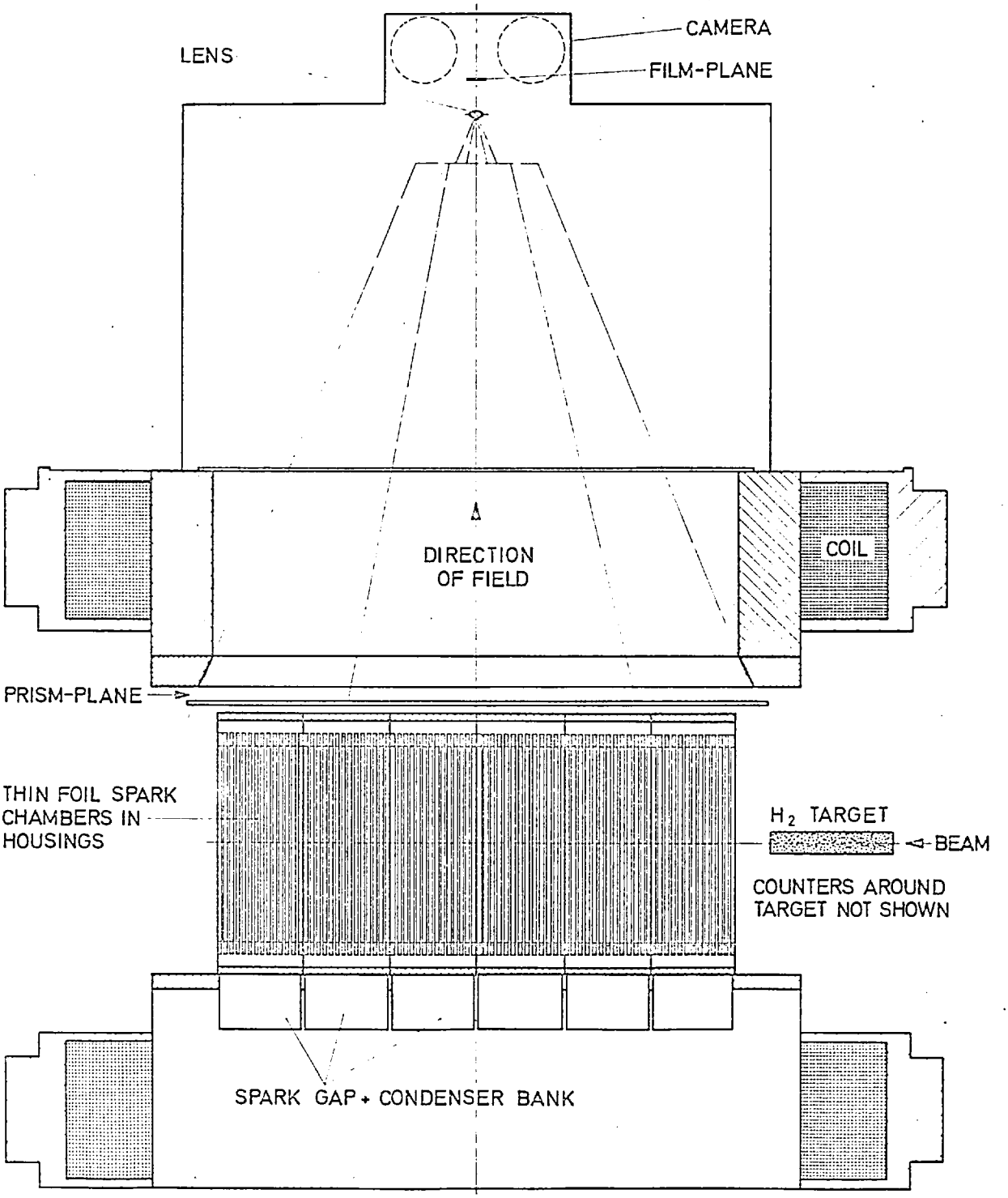

FIG. 2.5 b

MAGNET SPARK CHAMBER

SECTION ACROSS
BEAM DIRECTION

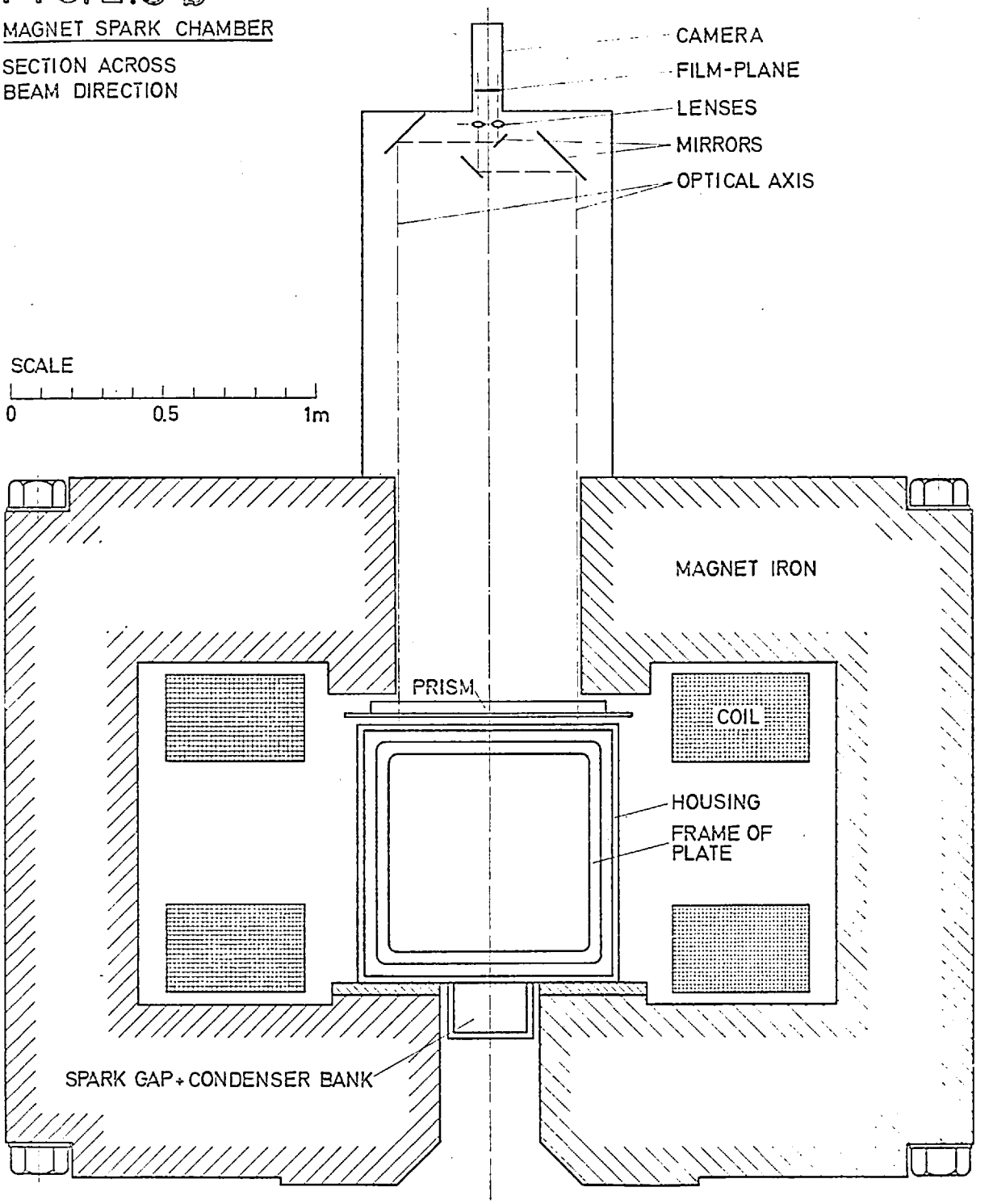

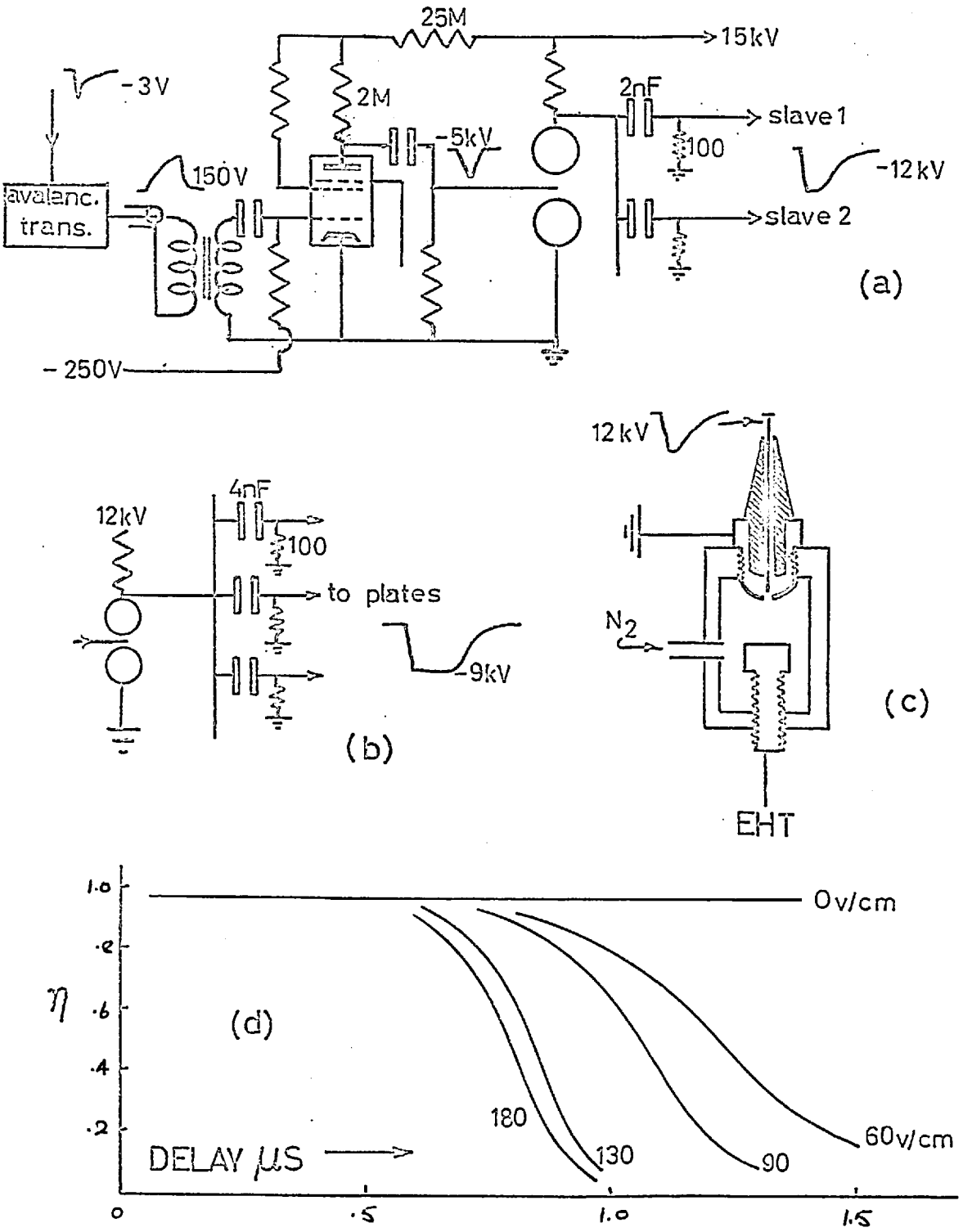

FIG. 2.6 Spark Chamber Operation

a) Master Pulser

b) Slave Circuit

c) Spark Gap

d) Efficiency vs delay

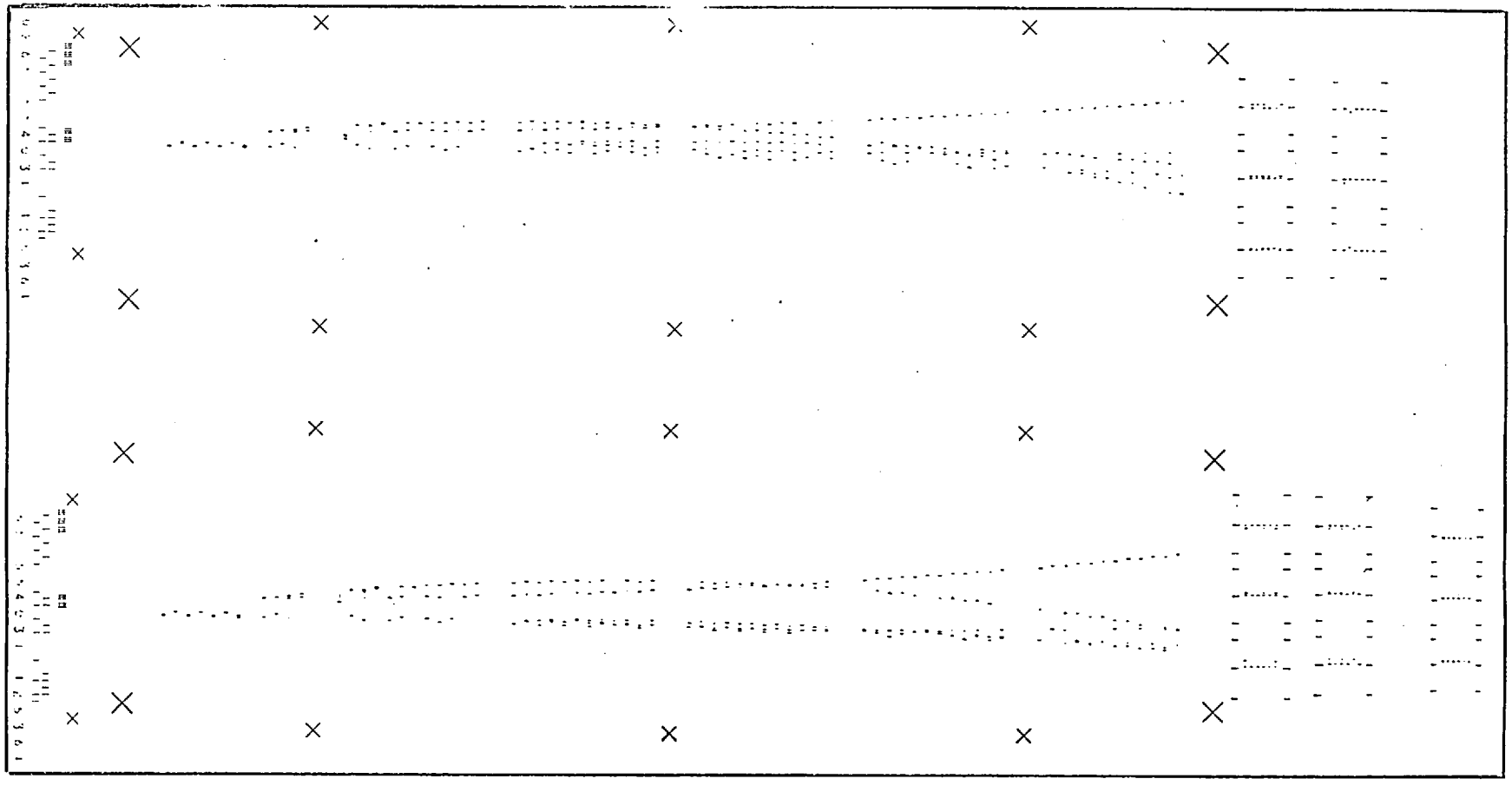

FIG.2.7 2 V^{o}s and an 'old' beam track

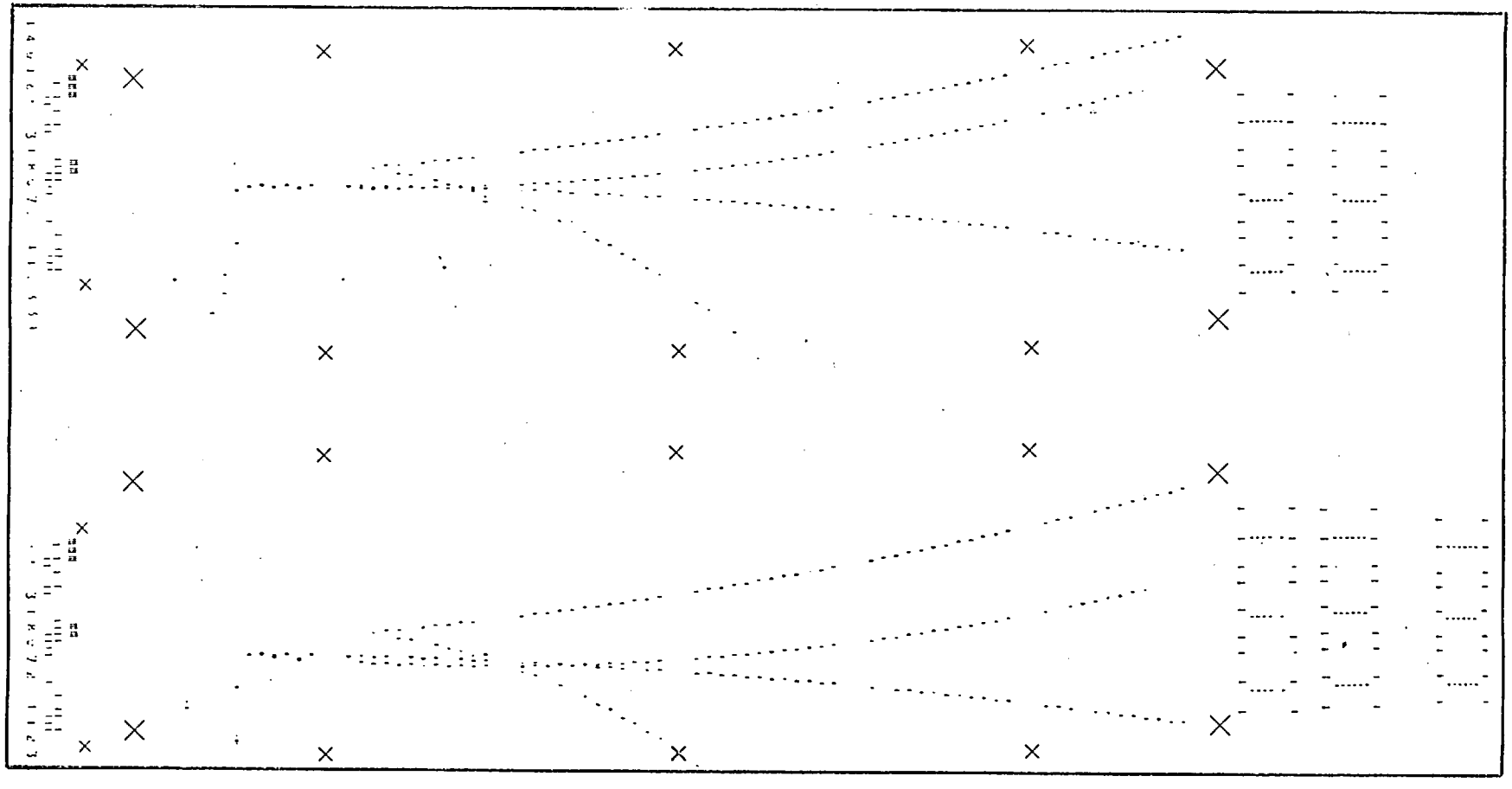

FIG. 2.8 2 V° decays

CHAPTER 3

ANALYSIS OF DATA

3.1 SCANNING

The photographs were examined to select events displaying the incident pion signature in which two neutral decays were visible. For each of these events a card was punched containing information to aid measurement and book-keeping. This consisted of:

(i) frame number

(ii) position of apices (specified by a number defining the chamber gap)

(iii) details of background tracks.

Events were easily recognised; from a sample of 7000 photographs, scanned twice for single neutral decays, an efficiency of 96 % was estimated. We assume that the scanning efficiency for double neutral decays is better than this figure.

The very simple criteria admitted the acceptance of electron-positron pairs and interactions, not contemporary with the trigger, which simulated decays. An indication that either of these possibilities

existed appeared on the punched card. The latter, besides providing some mental stimulation to the scanning girl in a dull task, was used for the interpretation of events rejected at a later stage in the analysis.

3.2 The Flying Spot Digitiser

The Hough-Powell Device (HPD) is a high precision automatic measuring machine. Prior to the present experiment several spark chamber photographs had been analysed using HPD[19] but these all involved straight tracks and simple events; its application to the more complex geometries in this and in a bubble chamber experiment[20] has proved fairly successful.

A narrow beam of light is split; one half passes through the film whence it falls on a photomultiplier cathode, the other is transmitted through a series of reference fringes which record its position. The light spot is swept across the film, the photomultiplier registering any variation of contrast. The spot's position, when a pulse is received, is recorded from the reference fringes and by advancing the film perpendicularly to the direction of sweep the complete event is digitised. The time taken to measure one frame was twenty seconds and the precision, determined by the fringe resolution, 1.6 microns on the film.

H.P.D. is operated on line to an IBM 7090 computer, occupying one data channel. A flow diagram of the control programme is shown

in Figure 3.1.

The scan card information is read into store and the film transport advanced to find the frame required. This is scanned and the digitisations passed over to the central programme which reduces an average of ten thousand digitisations to some five hundred co-ordinate pairs describing the event in two views.

The extraction of the 'signal' from the background proceeds in two stages. First noise, then accidental tracks are eliminated. Once a track is discovered the programme can predict, within a certain tolerance, where to look for the next spark. The track can now be more precisely defined and the tolerance reduced. In this way all the tracks are 'followed', and noise is eliminated. Using the scan card information, concerning any accidental tracks present, together with the apex positions, the track co-ordinates are sorted to present to the spatial reconstruction programme measurements satisfying the event topology.

From 4500 photographs measured 1300 were rejected: the programme could not find, in both views, four tracks consistent with a two V^{o} topology. Some rejections are due to a failure in finding fiducial marks; this is an unbiased loss. However, difficulties were encountered when an event contained a short, low energy track comprising few sparks. Also, if many tracks crossed each other in either view, the programme failed to resolve the confusion. Rejection, if due to either cause can definitely not be considered as unbiased.

In the first case low energy decays are preferentially lost; in the second, those events in which both neutrals emerge along a similar direction in the laboratory are most likely to present the confused photograph. To control these biases a random sample of the rejections were measured by human operators.

3.3. Spatial reconstruction of an event

The measurements, consisting of spark co-ordinates and fiducial marks for two stereo views were converted into parameters defining the trajectory of particles in space. The low density of material in the chamber produced no significant slowing down of the particles; combined with the good magnetic field uniformity this allowed a helix to be fitted to the trajectory, its axis parallel to the direction of the field.

The least squares fitting of helices, considered to be the main problem, is calculated in the CERN bubble chamber geometry programme THRESH[21]. The reconstruction of the beam trajectory, the optical system, systematic deviation of spark position and the location of vertices were problems not common to our spark chamber and the bubble chamber systems. These are discussed in the following paragraphs.

1) Optical distortions

The prisms between the camera and chamber elongated the track image distorting the circular path. Accurate machining of the prisms to the same mean thickness allowed this systematic distortion to be

evaluated simply. No correction other than that due to the bending of the reconstruction rays was applied.

To investigate the distortion produced by other elements of the optical system, e.g. lenses and mirrors, a wire grid, in a plane perpendicular to the optical axes was photographed and measured. The measurements on both views could then be compared with the known wire positions and a 'distortion'function' evaluated. We define co-ordinates in a right handed system with Z-axis parallel to the optical axis and X-axis perpendicular to the plates.

The true position in space, Y, is related to the measurements (x, y) by

$$Y = y + \sum_{m,n=0}^{2} \alpha_{m,n} \, y^m x^n \quad \ldots\ldots \text{ approx. to 2nd order}$$

The coefficients $\alpha_{m,n}$ were determined by least squares, separately for each view. Measurement of the X-coordinate is not considered as the problem is reduced to locating the gap in which the spark occurred, i.e. X-coordinates are 'quantised'. The coefficient $\alpha_{o,2}$, depending on X^2, corrects a systematic curvature to all tracks. This determines the momentum, so was accurately calibrated under experimental conditions from straight beam tracks, measured in the chamber without magnetic field. Differences of $\alpha_{m,n}$ for both views corrected a curvature in the Z-X plane which would have yielded incorrect estimates of dip angle.

ii) Systematic errors resulting from spark displacement

During the time interval between the passage of an ionising particle and the application of the high voltage pulse the ions produced drift in the crossed electric and magnetic fields. The electric field is contributed to by the clearing field and the opposing high voltage pulse during its finite rise time. Whilst the diagram of Figure 3.2 does not attempt to show the details of the spark formation process it illustrates the effect on the spark position of the force:

$$-\underline{F} = e\underline{E} + e\underline{E} \times \underline{H}$$

The second term produces the staggering referred to in Chapter 2.5. The first is observed only when the trajectory is inclined to the normal to the plates. A drift of $2\ \Delta x$ towards the anode results in a lateral drift of $\Delta y = \Delta x \tan\theta$ from the trajectory. The spark is expected to be displaced by this amount. Figure 3.3 is a distribution of δY, the difference between the measured position of a spark and the helix fitted through a complete series of sparks. The clearing field was 60 volts/cm. and the effect of the staggering is clearly illustrated by the twin peaks. The corresponding distribution for δZ is also shown; as expected it exhibits no systematic displacement.

To separate the two effects we give an alternating sign to the deviation: i.e. $\delta y = (-1)^n\ \delta Y$ where 'n' is the gap number.

From a large sample of $2V^o$ events the angular dependence of the mean deviation $\overline{\delta Y}$ was plotted; Figure 3.4. The variation of $\overline{\delta Y}$ with angle indicates the electric field drift while its value at $\theta = 0$ measures the staggering. Both effects were corrected by modifying each spark coordinate in space.

$$X' = X + (-1)^n \Delta X$$

$$Y' = Y + (-1)^n \Delta Y$$

i.e. ΔX displaces the quantisation value from the gap centre:

$$\Delta X = d(\overline{\delta Y})/d(\tan\theta) = 1.2 \text{ mm}$$

$$\Delta Y = \overline{\delta Y}\ (\theta = 0) = -1.1 \text{ mm}$$

It was found that this correction influences the fit of a helix to the sparks even in the case of tracks of maximum length, where 48 sparks are used. The curvature of 12 GeV/c tracks is then affected to the order of 1 % . In the case of short and highly curved (i.e. large θ) tracks the effect is more important.

iii) Apex reconstruction

The parameters defining a track must be specified at an interaction vertex before kinematic constraints are applied. We have, for reasons stated in the introduction to this section, considered a constant curvature. The dip angle, λ , is also constant, there being no component of magnetic field in the X-Y plane; however, the azimuth angle φ varies along each track and must be specified at the apex. Even under ideal conditions the position of

the apex of a V^o can be measured only to within 2 cm, the gap separation. Spark inefficiency, superposition of tracks and decays before the sensitive volume of the chamber all increase the imprecision. Consider a neutral decay at 4 GeV/c ; if the azimuthal angles of the charged tracks were measured at a point 4 cm. from the apex the opening angle would differ by 10 milliradians from its correct value.

All apices were determined by extrapolation of the helices. At 5 mm intervals, along the X-axis, the helix separation was calculated and the apex defined midway between the helices at closest approach. The Z-component of the separation was weighted by the inverse stereo constant 1/4.7.

The error in this measurement was evaluated from the helix separation at points neighbouring the apex. If, at some point ΔX distant from the apex the helix separation was double the minimum value, then ΔX was the error assigned to the X coordinate of the apex; the corresponding azimuthal angle error, $\Delta\varphi$, is calculated from the curvature. Any apex reconstructed more than 4 cm distant from that determined by inspection on the scanning table was flagged, but not rejected.

Figure 3.5 compares the mass resolution of the apparatus with and without apex reconstruction. The improvement is patent.

iv) Beam reconstruction and interaction point in the target

The reconstruction, in space, of the beam trajectory is derived from measurements of sparks and reference marks for each of the five beam chambers. Having determined the position (Y_i, Z_i) of the track in the i th chamber the set of coordinates, from each chamber, is used to determine completely the parameters of the beam track. We adopt the conventional description of the beam in terms of the geometrical optics variables, Y_i and its first and second derivatives in the horizontal plane; in the vertical plane where we assume no chromatic dispersion only Z_i and its first derivative appear.

The ray equations:

$$\begin{pmatrix} Y_i \\ Y_i' \\ Y_i'' \sim \frac{\Delta p}{p_o} \end{pmatrix} = \begin{pmatrix} 1 & L\cos\theta/2 & -L\sin\theta/2 \\ 0 & 1 & -2\tan\theta/2 \\ 0 & 0 & 1 \end{pmatrix} \begin{pmatrix} Y_o \\ Y_o' \\ \frac{\Delta p}{p_o} \end{pmatrix}$$

in the horizontal plane, and

$$\begin{pmatrix} Z_i \\ Z_i' \end{pmatrix} = \begin{pmatrix} 1 & L \\ 0 & 1 \end{pmatrix} \begin{pmatrix} Z_o \\ Z_o' \end{pmatrix}$$

in the vertical plane can be solved by least squares. The angle θ depends upon the bending power of the magnet and L is the length of the drift space separating the chambers. The solution to these equations; Y_o, Z_o, Y_o', Z_o', $\frac{\Delta p}{p_o}$ defines the beam trajectory at $X = X_o$, a specified plane through the target. The transformation of co-ordinates required to convert

$(X_o, Y_o, Z_o, Y_o', Z_o', \frac{\Delta p}{p_o})$ to a helix

$(X, Y, Z, \varphi , \lambda , \rho)$, the description of the track in the magnetic spark chamber co-ordinate system, is deduced from measurements of the same beam track both in the main chamber and in the beam chambers. The conversion to X, Y, Z, φ, λ is a simple translation and rotation of axes. The momentum dispersion $\frac{\Delta p}{p_o}$ must be described by a curvature. The mean momentum of the beam, p_o, is measured in the magnetic spark chamber and hence an absolute value may be assigned to Δp. The momentum of the track in question, $p_o + \Delta p$, is then transformed to ρ, the radius of curvature in the fringe magnetic field superimposed over the target.

A number of reconstruction failures occurred when more than one beam track was visible in the small chambers. The procedure adopted, in this case, was to fit two tracks through the beam matrix, selecting from each chamber the co-ordinates which gave the least residuals in the fit. From two distinct reconstructed tracks, that one not responsible for the trigger must be eliminated. Both tracks we extrapolated in an attempt to correlate them with an accidental beam track, visible in the magnetic chamber. In the first stage it was not always possible to select, unambiguously, the correct combination of co-ordinates belonging to one track: the residuals did not differ sufficiently. In the second stage the correlation sequence often failed.

In all cases of failure the parameters of a standard beam track were provided. These were the mean values; errors corresponded to the width of the distributions; i.e. the physical dimensions, angular divergence and momentum bite of the beam.

The position in the target of the interaction point is derived from the intersection of the beam track with the flight paths of the two neutrals, as calculated from their decays. This is a mass independent calculation. From the three points of nearest approach of each pair of tracks taken in turn a mean, weighted by $\sin^2 \beta$ (β is the angle of intersection of the pair), is calculated. If a well measured beam track is not available the interaction vertex is located using only the two neutrals.

3.5 Kinematics

1) The fitting procedure

The spatial reconstruction of an event consists of measurements of ρ, λ, φ for all charged tracks at a given vertex. At each of five points (evenly distributed along the track) the magnetic field is interpolated from a 3-dimensional map. A weighted mean field is used to determine the momentum from the curvature.

Four-momentum conservation applied at an interaction vertex; this may be a particle decay or a beam interaction; imposes the following constraints on the variables p_i, λ_i, φ_i of the i th track:

$$\sum_i p_{xi} = \sum_i g_i p_i \cos\varphi_i \cos\lambda_i = 0$$
$$\sum_i p_{yi} = \sum_i g_i p_i \sin\varphi_i \cos\lambda_i = 0$$
$$\sum_i p_{zi} = \sum_i g_i p_i \sin\lambda_i = 0$$
$$\sum_i E_i = \sum_i g_i (p_i^2 + m_i^2)^{\frac{1}{2}} = 0$$

$g_i = \pm 1$ depending as the i th track is in the initial or final state.

If the measurements are substituted into the constraint equations the unmeasured variables may be determined, provided their number does not exceed four. A V^o decay has, for a given mass assignment, only three unmeasured variables, those of the unseen neutral track. Any three equations are sufficient to determine these, but, since the measurements are not exact, the fourth equation is not satisfied. In order to improve the track variables the constraint equations are solved by least squares subject to the chi-square being a minimum. This process is termed the 'kinematic fit'. The chi-square is a measure of the overall difference between the measured event and that fitted. It is defined:

$$X^2 = \sum_{ij} (X_i^m - X_i^F) \; G_{ij} \; (X_j^m - X_j^F)$$

X^m and X^F are the measured and fitted track variables:
i , j = 3 x number of tracks. G, the weight matrix, is the inverse error matrix of the variables. This contains no inter-track correlations and any entry corresponding to an unknown variable is zero. The fitted variables are calculated by minimising the expression

$$X^2 + 2\Sigma \lambda_\alpha f_\alpha \quad .$$

$f_\alpha = 0$ are the constraint equations

λ_α are Lagrangian multipliers

Since the constraint equations are non-linear in the x_i an iterative procedure must be used in which the fitted variable after the ν th step becomes the 'measured' variable for the $(\nu + 1)$ th step. The process continues until the constraint equations are satisfied within a specified limit.

ii) Hypothesis testing

In discussing the fit we assumed that the particle masses were known. This is not, a priori, true. A set of hypotheses consistent with the event topology, satisfying charge, baryon and strangeness conservation is compiled. For each hypothesis the event is fitted. A set of X^2's is obtained, one for each hypothesis. The lower the X^2 the less the measurements had to be forced to satisfy the constraints.

The X^2 can be developed into a probability using the theoretical X^2 distribution corresponding to the number of degrees of freedom N.

N = Number of constraint equations - Number of unknown variables

$$P(X^2) = \int_{X^2}^{\infty} \frac{X^{2\,\frac{N}{2}-1}}{2^{\frac{N}{2}}\,\Gamma(\frac{N}{2})}\, e^{\frac{-X^2}{2}}\, dX^2 \quad .... (3.1)$$

This is the probability that from a pure sample of events of a particular type one such event, selected at random, would yield a X^2 higher than that obtained. A comparison of the $P(X^2)$ for each hypothesis allows an interpretation of the event. This is not possible comparing the magnitude of the X^2 which, for one event, may be derived from hypotheses with $(N = 1)$ and without $(N = 4)$ a neutral track.

The programme GRIND[22] was used to perform the hypothesis testing and kinematic fitting.

For each event the two V^os were tested for compatibility with the hypotheses.

$$\begin{aligned} K_1^o &\rightarrow \pi^+ + \pi^- \\ \Lambda &\rightarrow p^+ + \pi^- \\ \bar{\Lambda} &\rightarrow \pi^+ + p^- \\ \gamma &\rightarrow e^+ + e^- \end{aligned} \qquad (3.2)$$

All are one degree of freedom (one constraint) fits. The electron-positron pair hypothesis differs from the strange particle decays in that it can never satisfy momentum and energy conservation. There is always an unbalance, supplied by the momentum transferred in the field of a nucleus. The maximum of the transferred momentum spectrum of high energy gamma rays occurs at 1.3 MeV/c ; the mean is at 2.0 MeV/c.[23]

The limit imposed on the constraint unbalance was 5 MeV/c. This is higher than the typical value in the gamma conversion. We use this argument to treat the decay hypotheses (3.2) equally.

If the chi-squared probability indicated that any of the combinations $K_1^o K_1^o$; $\Lambda \bar{\Lambda}$; $K_1^o \Lambda$ were possible interpretations a fit at the production vertex was attempted. The fitted variables of the neutrals were used, together with the beam measurements to test each of the following hypotheses

$$\begin{aligned} \pi^- + p &\longrightarrow K^o + \bar{K}^o + n \\ \pi^- + p &\longrightarrow \Lambda + \bar{\Lambda} + n \\ \pi^- + p &\longrightarrow \Lambda + K^o \end{aligned} \qquad (3.3)$$

The first two, with a missing neutron, are one constraint fits; the associated production, with all variables measured is a four constraint fit.

If any of these hypotheses were satisfied the three vertices were combined to compute a multivertex fit. At this stage the criterion used to accept a hypothesis was very loose; $P(X^2)$ was required to be larger than one in ten thousand. Even at this level ambiguous interpretations numbered less than ten per cent.

Multivertex fitting differs in the spark chamber experiment from the procedure which would be used for the same event measured in a bubble chamber. The beam particle would appear to stop in the bubble chamber liquid. The position in space of the production vertex can

then be measured. Together with the position of the decay vertices the angles of each decaying neutral can be calculated. Thus, in the overall fit the only unknown variables are the momenta of the decaying neutrals together with any completely missing neutrals. Hypotheses (3.3) in a multivertex fit would have respectively 7, 7 and 10 degrees of freedom.

In the hydrogen target of the present experiment the beam interaction is not seen. Its position can be calculated as described in Section 3.3 but this is derived, by reconstruction, from the V^o decays. The angles of the neutrals cannot now be considered as independent bona fide measurements. As a result the hypotheses are modified to 3, 3 and 6 constraint multivertex fits. Furthermore, since the trajectory of the beam is curved in the fringe field of the magnet as it travels through the target, the precise determination of the azimuth is not an independent measurement. From the experimental distribution of reconstructed interaction vertices along the target a fixed value of the azimuth (corresponding to a point 10 cm before the end of the target) was determined. Assuming that the interaction occurred in the target a corresponding error was assigned. Although this value of the beam azimuth is very definitely not normally distributed, and the importance of this is explained in the following paragraph, it is not a precise measurement and its contribution to the weight matrix, G, is small.

(iii) Error assignment

Before using the probability test as a criterion for selection of events the X^2 distribution obtained from many fits must agree with the theoretically expected one appearing in the integrand of (3.1).

The least squares method requires a set of normally distributed variables. For this reason the track variables $1/p$, λ, φ were used. They are closely related to the fundamental measurements made on the film and, therefore, most likely to have normally distributed errors. Errors assigned to all variables are calculated from the error in measurement of the sagitta, Δs, of a track. The intrinsic anisotropy of the spark chamber had to be considered. Fluctuation of spark position (Fig. 3.4) increases as the angle between the track and the normal to the plates increases. This is taken into account by modifying the value of Δs given below (in section 4.3) accordingly:

$$\Delta s' = \Delta s + .07 \tan \left| \frac{0.6\, L}{\rho} + \varphi_o \right|$$

i.e. Δs is increased by an amount depending on the angle a curved track makes with the plates 0.6 of its length from the apex. This expression was empirically determined from the curves of Figure 3.4.

Error matrix elements $(G^{-1})_{ij}$ are derived from the 'geometry' errors:

$$\Delta\, 1/\rho \;=\; 8\,\Delta s' / L^2 \cos^2\lambda$$

$$\Delta\,\varphi \;=\; 0.5\,/\rho \qquad \ldots\ (3.4)$$

$$\Delta\,\lambda \;=\; 6\,\Delta s' \left[\cos^2\lambda + 0.01\right]^{\frac{1}{2}} / L$$

$$\Delta\,\varphi\,.\,\Delta\, 1/\rho \;=\; -32\,(\Delta s')^2 / L^3 \cos^2\lambda$$

Additional terms corresponding to the coulomb scattering are included. These are, in general, small.

The azimuth error $\Delta\varphi$ is that obtained from the precision of apex reconstruction (section 3.3). A useful parameter to check the errors on each variable is the 'normalised pull'.

$$P_i \;=\; \frac{X_i^m - X_i^F}{\Delta\,(X_i^m - X_i^F)} \;=\; \frac{X_i^m - X_i^F}{\sqrt{\left[\,(\Delta X_i^m)^2 - (\Delta X_i^{\dot{m}})^2\right]}}$$

This should be normally distributed about zero mean with unit variance. A biased distribution indicates a systematic error; a narrow (broad) distribution indicates an overestimated (underestimated) error.

The experimental distributions of chi-square and normalised pulls, using the above error assignments, are discussed in Chapter 5 when event selection and biases are considered.

3.6 Statistical Analysis

The statistics programme SUMX was taken, in its standard form, from the CERN programme library. A data summary tape, DST, containing one record of information for each measured event, is read. Histogrammes and two dimensional graphs, subject to selection criteria

and weighting, can then be plotted.

The limited core store of the IBM 7090 did not allow GRIND to produce the DST . An intermediate programme was used to calculate, using the output from GRIND , the additional information of physical interest required for this experiment.
Included were:

(i) Centre of mass momenta and angles

(ii) Decay probabilities and weight factors

(iii) Effective masses

(iv) Invariant momentum transfer

(v) Resonance decay angles

To aid the study of possible biases no selection of events had been introduced. All measured by H.P.D. appeared on the data summary tape.

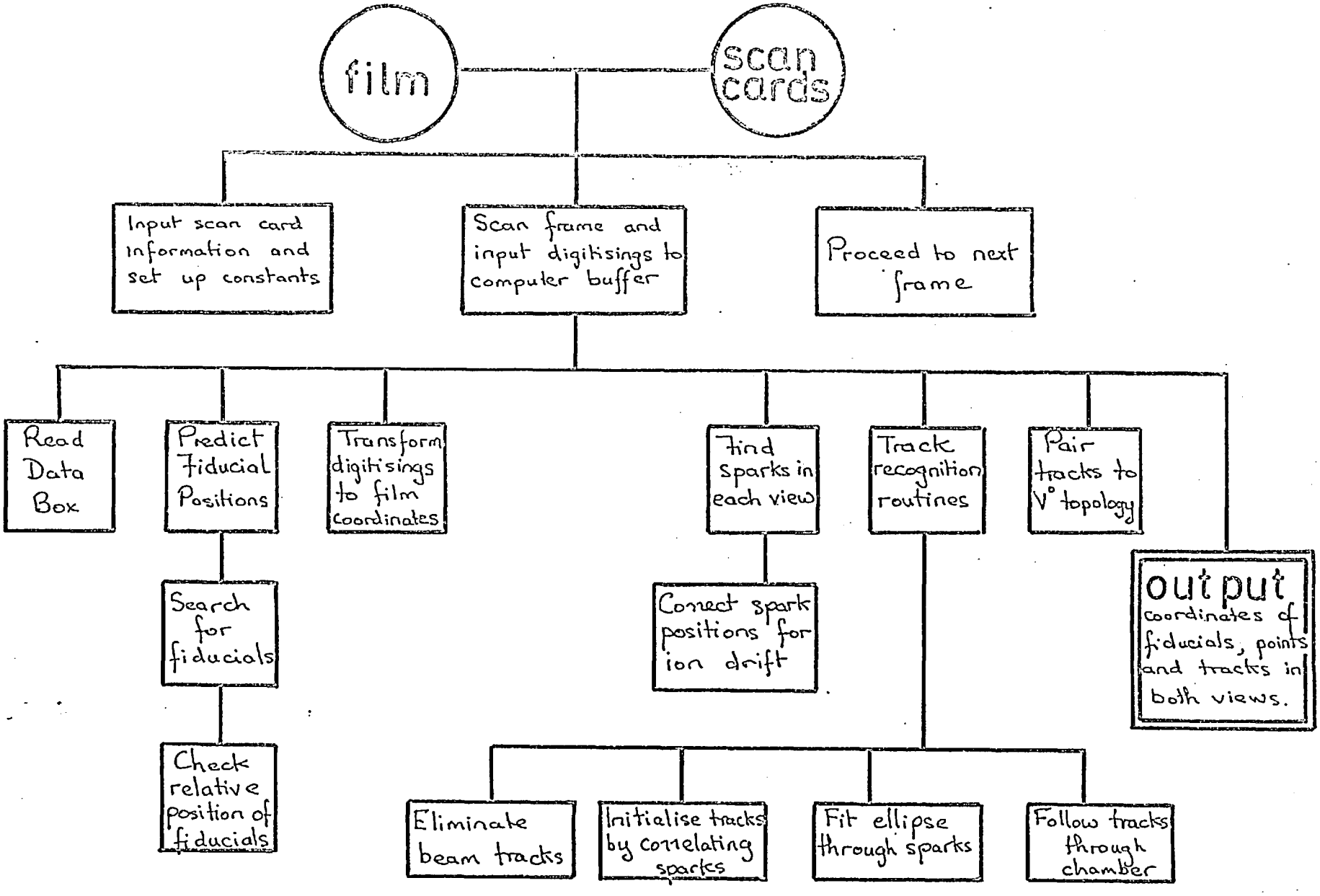

FIG. 3.1 Flow of HPD programme

FIGURE 3.2

EFFECT OF CLEARING FIELD ON INCLINED TRACKS

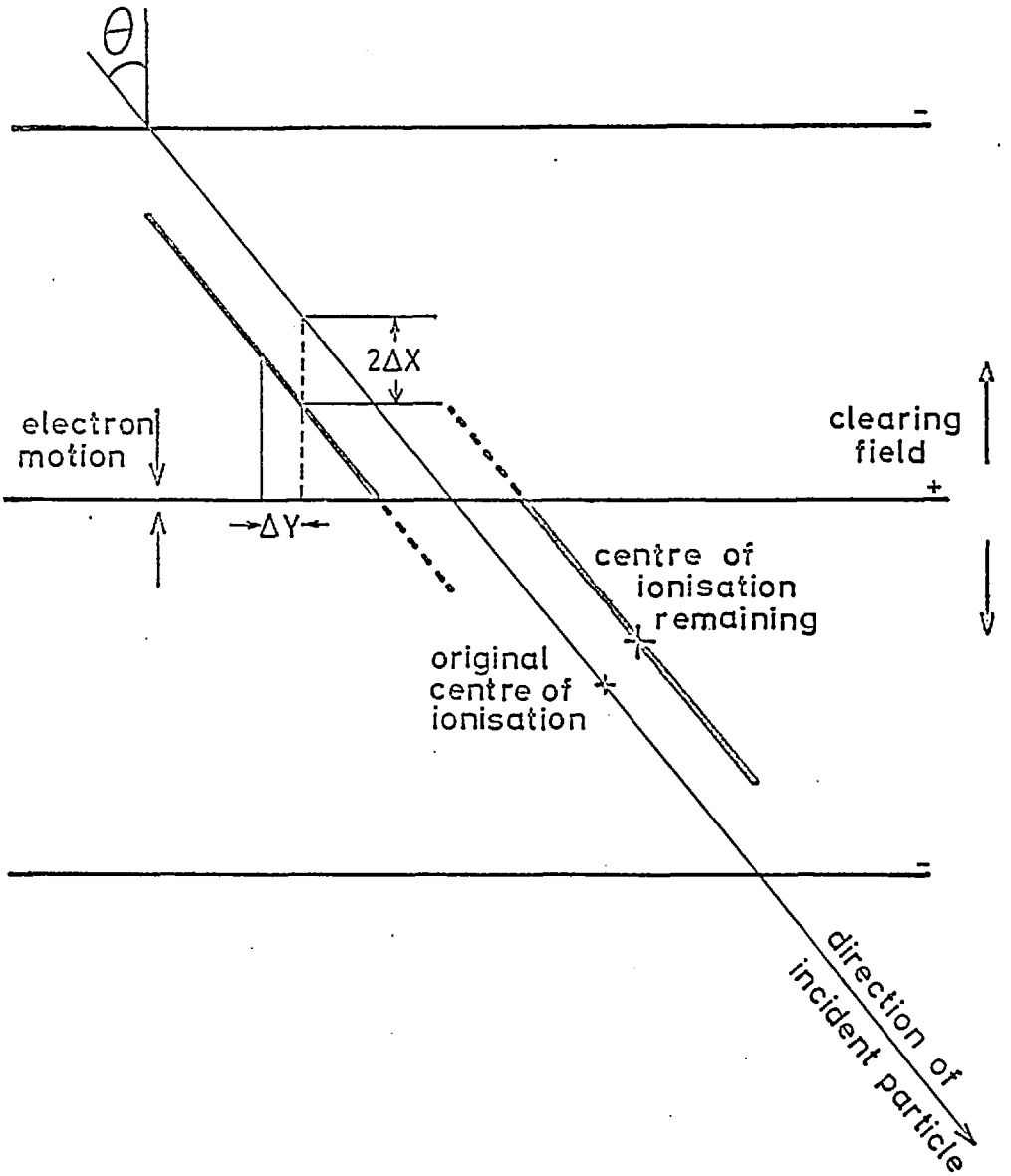

FIG. 3.3 Spatial Resolution

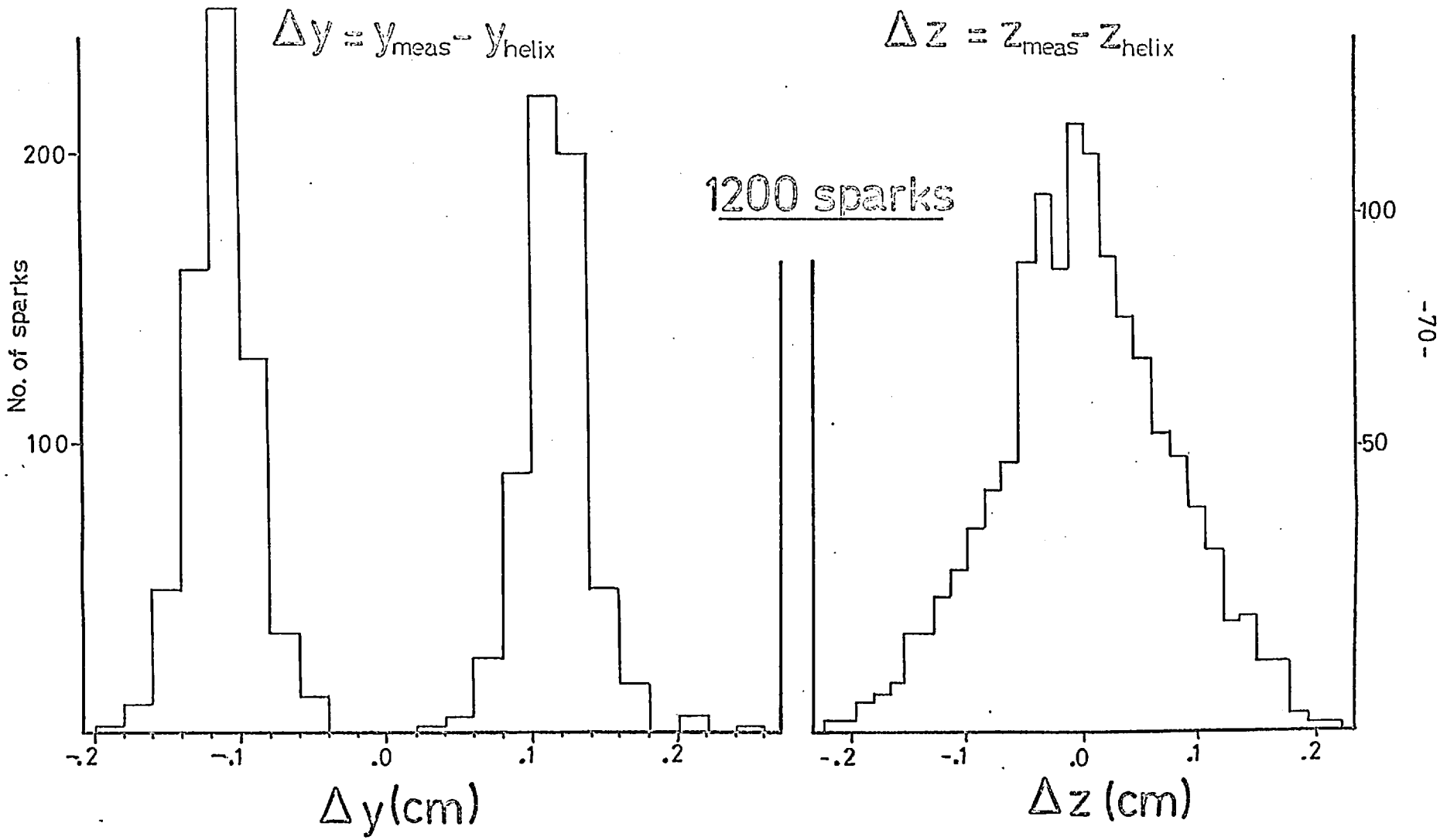

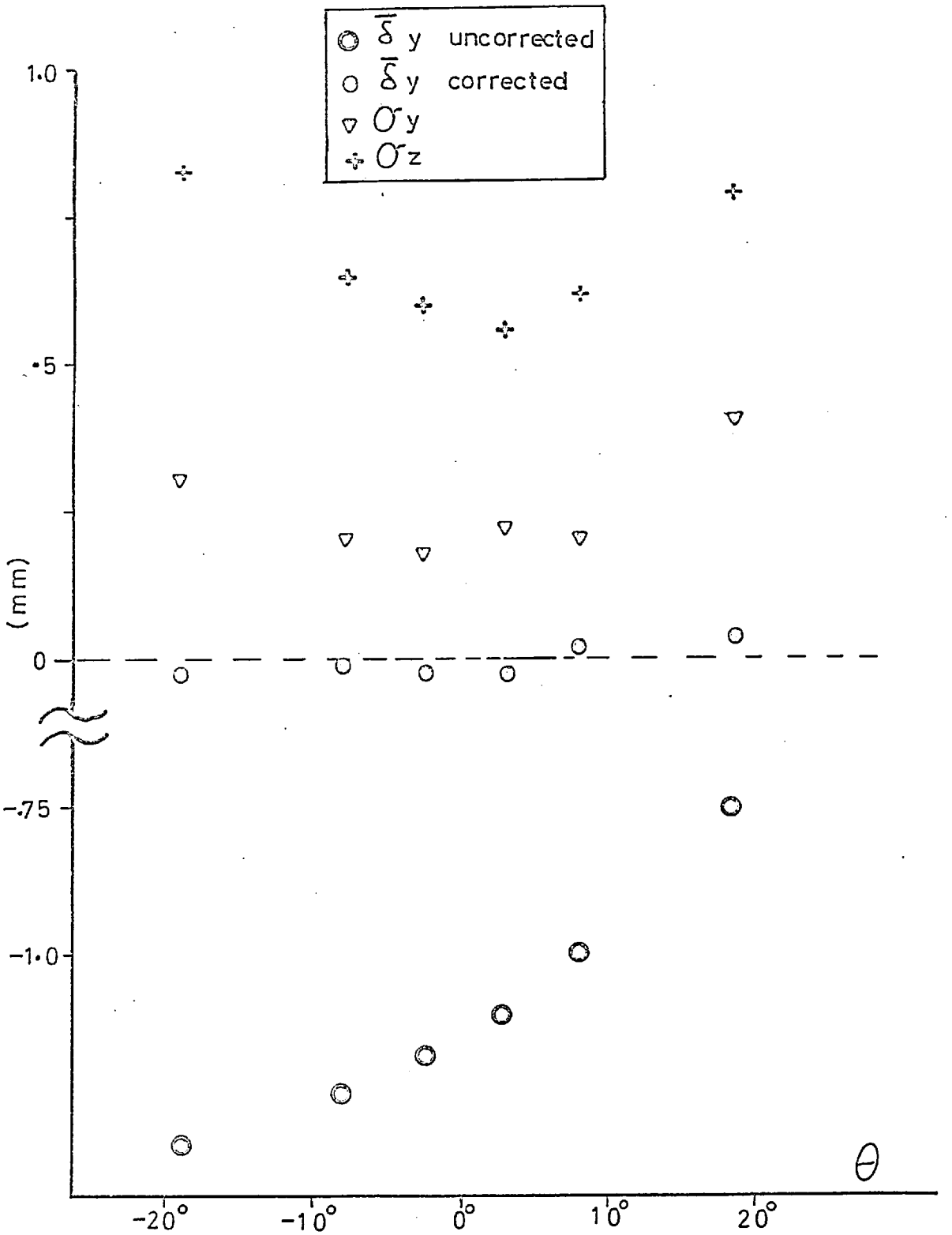

FIG. 3.4 Spatial Resolution vs. θ showing effect of correction for ion drift

FIG. 3.5 MASS DISTRIBUTION OF K_1^0 MESONS

a) Without Apex Reconstruction

b) With " "

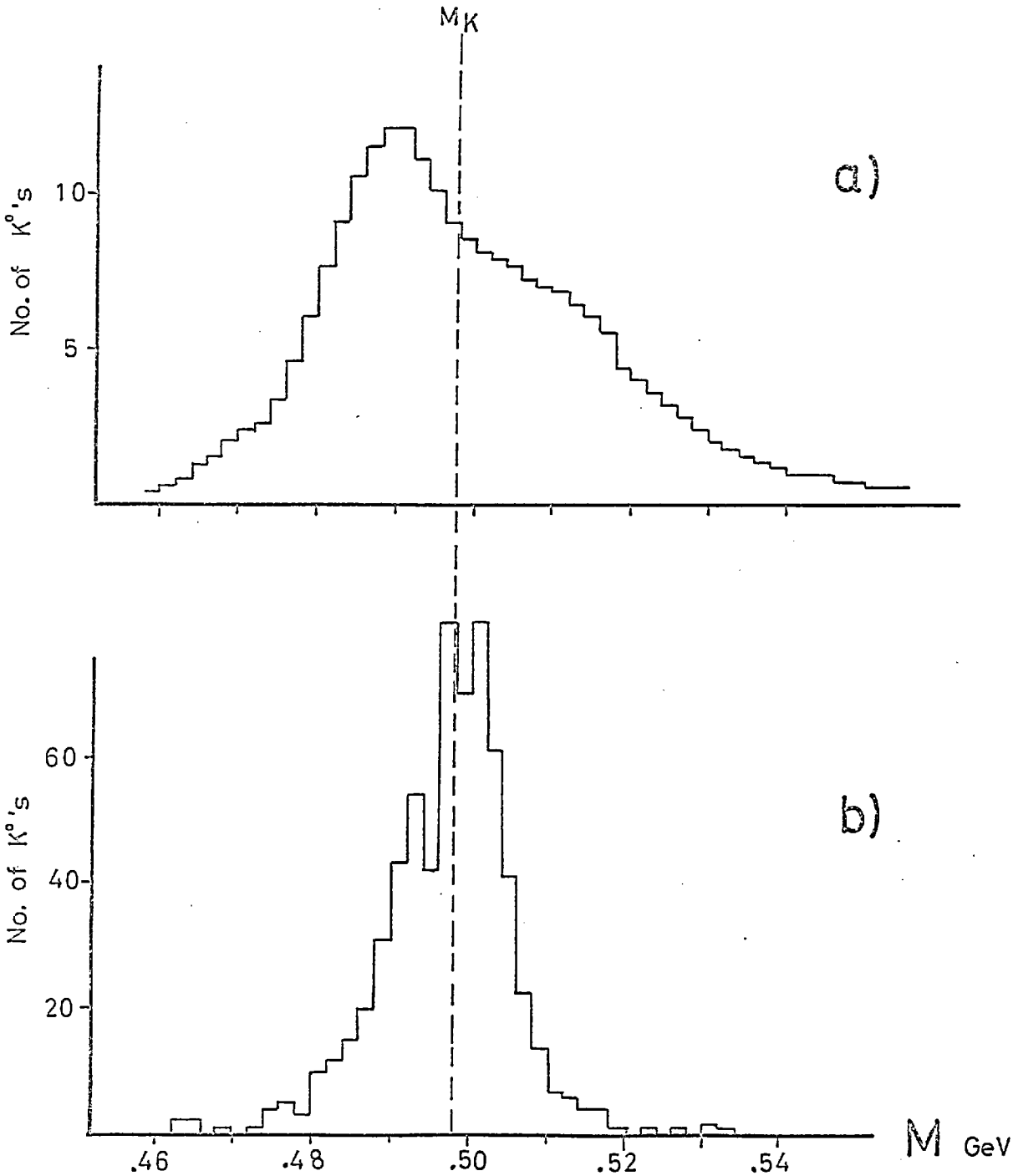

CHAPTER 4

EXPERIMENTAL RESOLUTION

4.1 Introduction.

When discussing the procedure used to reconstruct an event in space we considered, and corrected for, optical distortions and systematic electron drift which displaced the sparks. The resolution of the apparatus is now limited by the random displacements of the sparks from the trajectory, the precision of measurements by HPD and the coulomb scattering of a charged particle in the chamber material.

4.2 Spatial Resolution.

We refer in this section to the data presented in Figure 3.4. The displacements of measured spark position from a fitted helix have been corrected and the widths, σ_y and σ_z, of the distributions for Y and Z components plotted as a function of the angle made by the trajectory to the normal to the plates, i.e. the X-axis. The mean, $\overline{\delta y}$, is consistent with zero for all angles. The contribution to σ_y and σ_z from random fluctuations in spark position is the same; any difference in magnitude reflects measurement errors, weighted by the geometry of the stereoscopy.

We can express

$$\sigma_z = [\sigma^2_{y_{sp}} + 2\lambda^2 \sigma^2_{y_{meas}}]^{\frac{1}{2}} \quad :$$

where $\sigma_{y_{sp}} = \sigma_{z_{sp}}$ is the projected r.m.s. spark fluctuation
and $\sigma_{y_{meas}}$ is the r.m.s. measurement error in each stereo view.
λ is the stereo constant.

Similarly

$$\sigma_y = [\sigma^2_{y_{sp}} + \tfrac{1}{2}\sigma^2_{y_{meas}}]^{\frac{1}{2}} \quad :$$

From the observed values of σ_z = .6 mm; σ_y = .18 mm we deduce:

$\sigma_{y_{sp}}$ = .17 mm

$\sigma_{y_{meas}}$ = .09 mm in space (3.7 microns on film)

A measurement error, corresponding to 3.7 microns on the film, is higher than might have been expected from HPD; one digit represents 1.6 microns on the film. However, the width of the spark image was almost one hundred microns so the centre is found to within five per cent of the spark's width.

The spark position fluctuation in our magnetic spark chamber, $\sigma_{y_{sp}}$ = .17 mm improves on the best published data; $\sigma_{y_{sp}} \leq$ .2 mm [24], without a magnetic field, and $\sigma_{y_{sp}}$ = .5 mm [25] in a magnetic field. The corresponding number is σ_y = .08 mm in a bubble chamber.

4.3 Momentum Resolution.

The accuracy in measurement of the momentum vector (p, λ, φ) of

a particle depends upon multiple coulomb scattering, σ_y, knowledge of the magnetic field ($\pm .3\%$) and the apex reconstruction; the latter limits the precision of the azimuth angle, φ .

The coulomb scattering in the chamber material is calculated assuming a homogeneous medium with radiation length, X_o , thirty metres. The root mean square scattering angle in a thickness L of material is given by Rossi[26] as

$$\langle \theta \rangle = \frac{.021}{p\beta} \left| \frac{L}{X_o} \right|^{\frac{1}{2}} .$$

From the projected scattering angle one obtains the error in curvature

$$\Delta \frac{1}{\rho} = \sqrt{\frac{4}{3}} \cdot \frac{\sqrt{\frac{1}{2}} \langle \theta \rangle}{L \cos^2 \lambda}$$

$\sqrt{\frac{1}{2}}\langle \theta \rangle$ since we are interested in the projected scattering:
$\sqrt{\frac{4}{3}}$ is an emperical constant; see e.g. Solmitz[27].

Whence $$\left(\Delta \frac{1}{\rho}\right)_{\text{coulomb}} \doteq \frac{3 \times 10^{-4}}{p L^{\frac{1}{2}} \cos^2 \lambda} \quad \text{cm}^{-1} .$$

From a set of N measured points whose r.m.s. error is σ_y the fractional error in the radius of curvature of a track is given by

$$\frac{\Delta \rho}{\rho} = \sqrt{\frac{4}{N}} \frac{\sigma_y}{S} \qquad \text{(Gluckstern)}[28]$$

Hence the r.m.s. error in sagitta, ΔS , can be related through

$$\rho \doteq \frac{L^2}{8S}$$

to the error in the location of individual points :

$$\Delta S \simeq \frac{4\sigma_y}{\sqrt{N}}$$

For a track comprising fifty sparks we obtain :

$$\Delta S = 0.1 \text{ mm} .$$

The distribution of sagittae of 12 GeV/c beam tracks, 160 cm long, measured in the chamber without magnetic field is shown in Figure 4.1. The half width is .13 mm. Multiple scattering produces an r.m.s. sagitta, on 12 GeV/c particles, of .07 mm leaving the contribution from measurement errors of .11 mm.

This is in agreement with the expected value, from which we deduce a maximum detectable momentum for tracks 160 cm long ;

$$P_{MDM} = 1000 \text{ GeV/c} .$$

Measurements of neutral decays were limited on average to some thirty points per track. We increase the projected sagitta error accordingly. The value used in generating the error matrix was

$$\Delta S = .15 \text{ mm} .$$

The table below compares the contribution to the relative momentum error from coulomb scattering and from errors of spark location (including measurement errors) for different momenta. A track length of one metre is used.

p GeV/c	12	10	8	6	4	2
$\frac{\Delta p}{p}$ coulomb	.008	.008	.008	.008	.008	.008
$\frac{\Delta p}{p}$ meas.	.055	.04	.035	.027	.018	.01

We see that the coulomb scattering does not limit the momentum resolution. Momenta below 1 GeV/c would contain the coulomb term as the principal error, if the track were one metre long, but low energy tracks with their high curvature leave the chamber via the sides. Their length is, in general, less than one metre ; and the measurement term again provides the main contribution.

The precision, along the line of flight of a V^o, in the location of its apex is .5 cm. This limits the azimuthal resolution typically to one milliradian ; it is inversely proportional to the radius of curvature, i.e. the momentum.

4.4 Summary

We can illustrate the precision attained with an example. Typical errors on a track of momentum 4 GeV/c and length one metre are,

$$\Delta p = 100 \text{ MeV/c}$$
$$\Delta \varphi = .8 \text{ mrad}$$
$$\Delta \lambda = 1.0 \text{ mrad} .$$

Consider the error in the mass of a neutral kaon as derived from the

charged pion tracks with these errors.

$$M^2 = 2 m_\pi^2 + 2 (E_1 E_2 - p_1 p_2 \cos\theta)$$

$$\Delta \frac{M}{M} \doteq \frac{1}{3} \left[\frac{\Delta p_1}{p_1} + \frac{\Delta p_2}{p_2} \right] + \frac{p_1 p_2 \sin\theta \Delta\theta}{M^2}$$

θ is the opening angle of the two pions.

From the momentum term we expect a one per cent error ; from the angular term, averaging over all decay angles, a further one per cent. The error is then :

$$\frac{\Delta M}{M} = 1.4\% \quad \text{or} \quad \Delta M = 7 \text{ MeV/c}^2.$$

Figure 4.2 is the mass distribution of a sample of K_1^o mesons, determined from the decay products.

The mean value of the mass was

$$M_{K_1^o} = 496.7 \pm 0.4 \text{ MeV/c}^2 ;$$

$$\text{c.f. } M_{K_1^o} = 497.7 \pm 0.3 \text{ MeV/c}^2 \quad 1)$$

The error is statistical, it does not account for any error in the magnetic field ($\pm$ 0.3%) .

The r.m.s. width of the distribution is

$$\Delta M_{rms} = 7.3 \text{ MeV/c}^2 ;$$

in very good agreement with the calculation above.

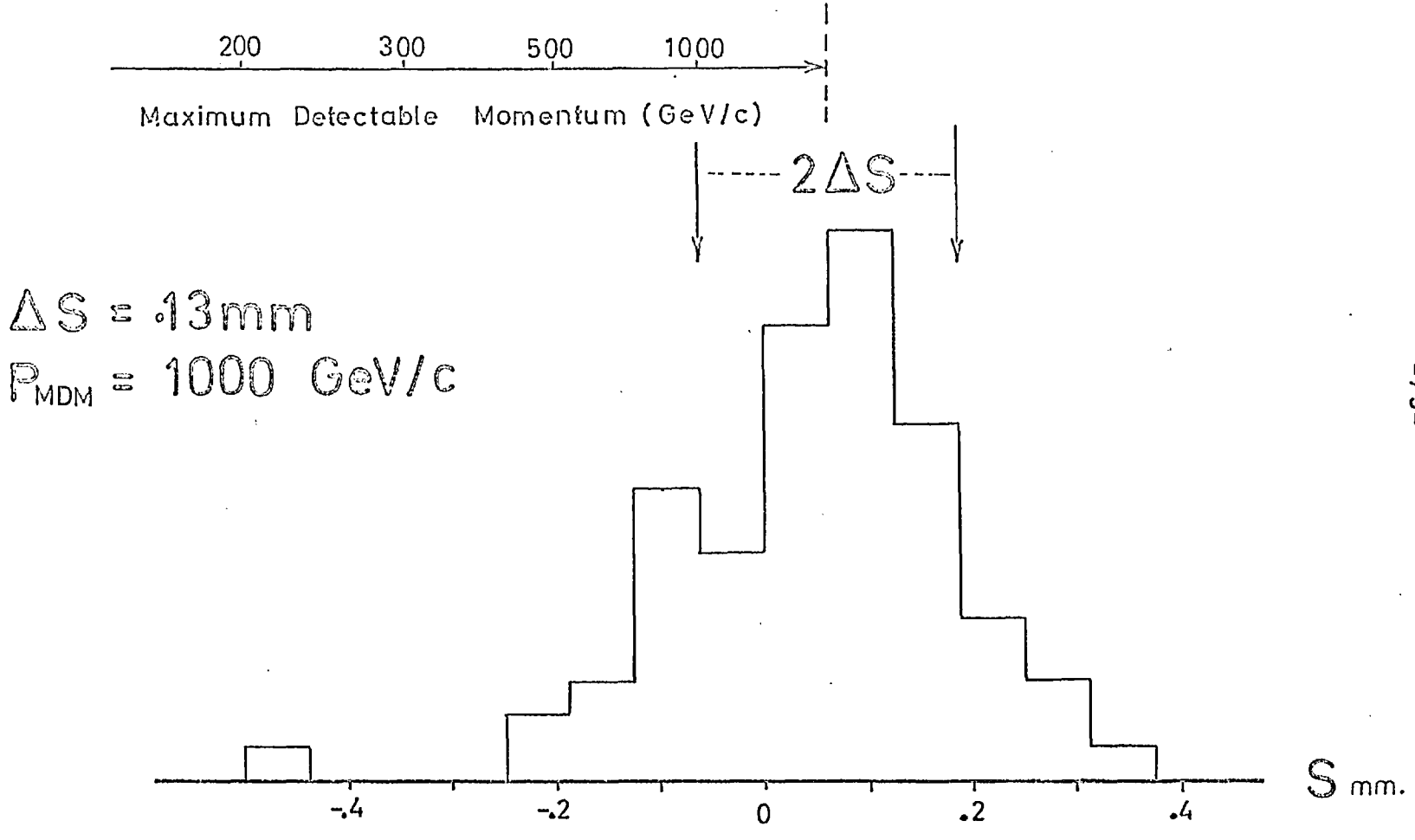

FIG. 4.1 Momentum Resolution

Sagittae of 160 cm tracks with no magnetic field.

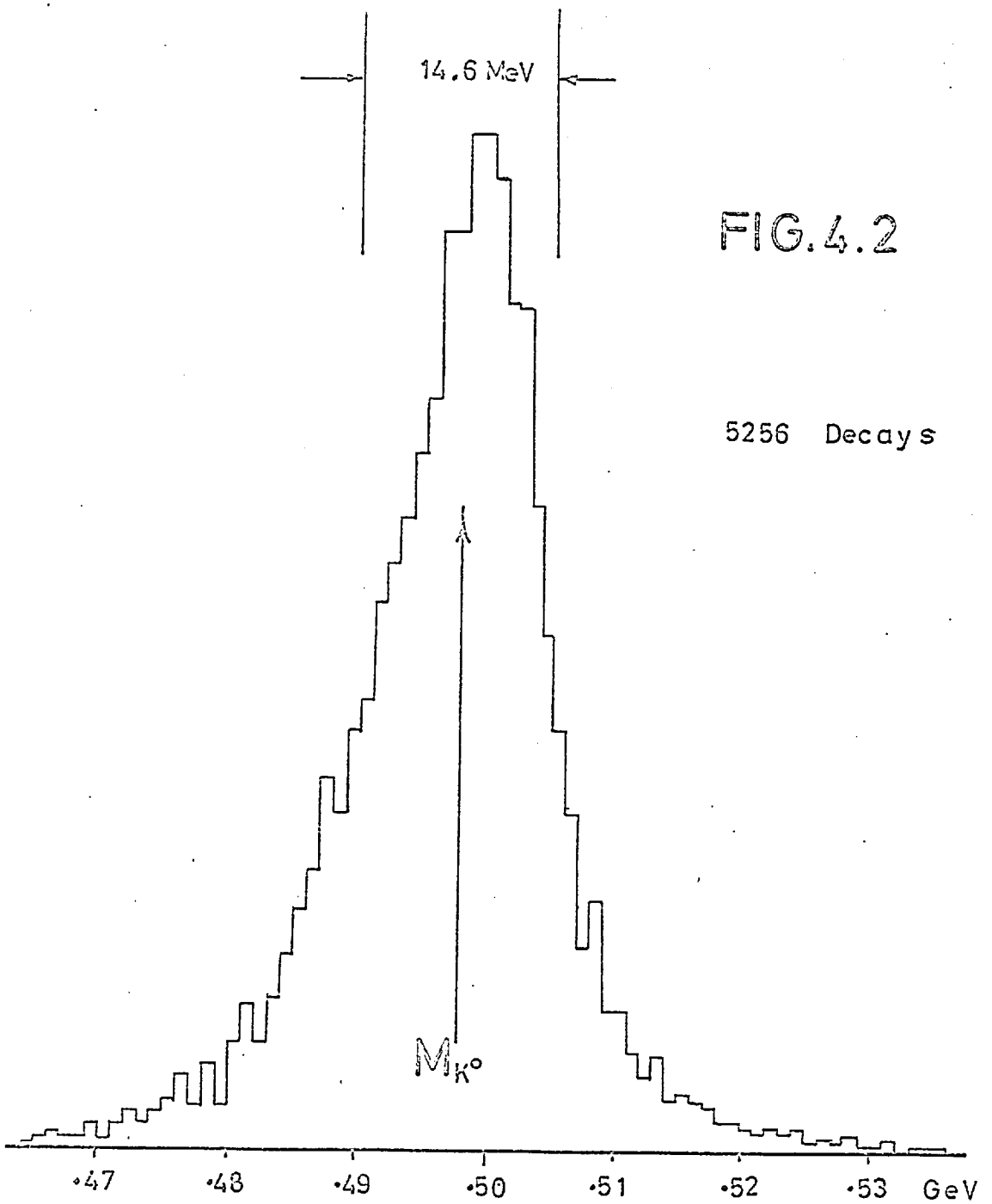

FIG. 4.2

5256 Decays

Mass of K_1° : Resolution ± 7.3 MeV

CHAPTER 5

EVENT SELECTION, BIASES AND THE EVALUATION OF TOTAL CROSS SECTIONS

5.1. Introduction

A reliable estimate of the cross section for the processes

$$\pi^- + p \longrightarrow K_1^o + K_1^o + n$$

$$\pi^- + p \longrightarrow \Lambda + \bar{\Lambda} + n$$

$$\pi^- + p \longrightarrow K^o + \Lambda$$

would be obtained if all V^oV^o events found on the film could be identified. In experiments with low statistics this is almost realised and events can be remeasured until some 95 % are identified.

In this experiment such a procedure has not been possible. Remeasurements with an automatic device will not yield different results unless it is programmed to include further possibilities. The time factor precluded successive remeasurement by hand of the rejected data. An example is illustrated in Figure 5.1 ; the history of a sample of photographs, taken at 12 GeV/c beam momentum,

is followed through the system.

The present chapter describes how the cross sections are evaluated from the HPD measurements and a sample of hand measured data together with the number of incident pions. We consider and correct for biases and losses introduced in the data analysis and from the detection efficiency of the apparatus.

5.2 Event Selection

From the photographs selected on the scanning table for measurement approximately twenty eight per cent were rejected by HPD . The programme was unable to find four tracks in each view consistent with two V^0's. A random sample of these rejected photographs was measured by human operators on a digitised projector and analysed in parallel with the accepted data.

After the geometrical reconstruction of the event two selection criteria had to be satisfied. The decays were to originate within a fiducial volume (this will be defined in the following section where we consider the detection efficiency) and secondly, the event had to be 'well measured'. For a well measured event we required:

a) Convergence of the helix fit to all four charged tracks from the decays.

b) The errors on the track parameters, generated internally in the helix fit, were to satisfy the condition

$$\sigma_i^{int} < 3 \sigma_i^{ext}$$

where σ_i^{ext} are the external errors as defined by equations (3.4)

c) The coordinates of both reconstructed V^o apices to be consistent with the positions specified on the scanning table. A tolerance of 4 cm, appropriate to the chamber inefficiency, was permitted.

Seventy five per cent of events in the fiducial volume were well measured. These were classified according to the results of the kinematic fit. A hypothesis was accepted if the chi-square probability exceeded 0.1 % . In Table I the numbers of events, well measured and identified with one of the production processes, are listed. We can immediately make two observations. Most events fit the process

$$\pi^- + p \longrightarrow K_1^o + K_1^o + n$$

and the number of ambiguities in identification is small.

5.3 Bias and contamination in the kinematic fit

There is no evidence of a bias in the fitting procedure, and the error estimates appear reliable. The chi-square distributions for K_1^o decay fits and $K_1^o K_1^o n$ production fits are shown in Figure 5.2 and compared with the theoretical distributions. In Figure 5.3 we show the distributions of normalised pull functions for the incident pion track and for the outgoing K_1^o's. They are normally

distributed with unit variance about a zero mean.

Though it does not contain as much information as the pull functions to indicate the confidence we may have in the fitting procedure, the missing mass is a physically significant parameter. Missing mass plots for these events fitting the three production hypotheses (Fig. 5.4) indicate that there is practically no contamination from the processes

$$\pi^- + p \longrightarrow K_1^o + K_1^o + n + \pi^o$$
$$\pi^- + p \longrightarrow \Lambda + \bar{\Lambda} + n + \pi^o$$
$$\pi^- + p \longrightarrow \Lambda + K_1^o + \pi^o$$

which would be seen in an excess of events with $MM > (\overline{MM} + m_\pi)$ over those with $MM < (\overline{MM} - m_\pi)$.

Those events with ambiguous interpretations are not going to affect any estimate of the $K_1^o K_1^o n$ cross section but they are a significant number compared with the $\Lambda\bar{\Lambda}n$ events. A pure sample of Λ or $\bar{\Lambda}$ will yield more ambiguous fits than a pure sample of K_1^o. This is because the decay momentum in the rest system of a K_1^o decay (206 MeV/c) is higher than that of a Λ in its rest system (100 MeV/c). It follows that the transverse momentum, which is a measureable quantity independent of any mass assignment, of a Λ decay is always less than the maximum allowed for a K_1^o decay whereas only those K_1^o's decaying with a transverse momentum less than 100 MeV/c could be interpreted as Λ or $\bar{\Lambda}$ decays. Approxmately one third of a sample of K_1^o's will decay with a transverse momentum less than 100 MeV/c. We should,

therefore, weight a set of ambiguous ($\Lambda\bar{\Lambda}$ n ; $K_1^o K_1^o$ n) interpretations 9:1 in favour of $\Lambda\bar{\Lambda}$ n were it not for the observed a priori probability of $K_1^o K_1^o$ n occurring more frequently than $\Lambda\bar{\Lambda}$ n (the factor is 200 at 5 GeV/c, 33 at 7 GeV/c, 24 at 12 GeV/c). We therefore weight the ambiguities in favour of $K_1^o K_1^o$ n by 22/1 ; 3.7/1 ; 2.7/1 for the 5, 7 and 12 GeV/c data respectively.

5.4 Corrections for biases and losses from HPD measurements

Eight per cent of the events are listed in Table I as unidentified. These are most likely to be τ^o decays or non-contemporary 2 prong and 4 prong interactions which occurred before the sensitive region of the chamber.

If it is assumed that the main source of electron pairs is the neutral decay of K_1^o's then a simple calculation based on the radiation length of the chamber gives an expected ratio:

$$\frac{\text{events with charged } K_1^o \text{ decay and an electron pair}}{\text{events with two charged } K_1^o \text{ decays}} \sim \frac{1}{8}$$

The number given in Table I falls short of this figure . A gamma ray from a neutral K_1^o decay will carry, on average, one quarter of the K_1^o momentum. The measured tracks of an electron pair have then, on average, four times the curvature of a K_1^o decay and are difficult to measure well with HPD . The figures in Table II, for badly measured events, support this fact; the number of

electron pairs exceeds that which is expected. It is seen that those events not satisfying the well measured criterion are not an unbiased sample. The corrections to the figures of Table I are applied in terms of upper and lower limits. An upper limit on the yield of K_1^o K_1^o n events from the badly measured data is given by assuming that sample is identical with the well measured data. A lower limit is given by the number of K_1^o K_1^o n events identified in the bad data.

The events rejected by HPD and remeasured by hand were treated in a similar manner. The breakdown is listed in Table III. Here again one sees a bias. There is a much higher proportion of events satisfying the

$$\pi^- + p \rightarrow \Lambda + K_1^o$$

hypothesis. The Λ particle, in this reaction, is generally very slow in the laboratory and the short, high curvature decay tracks are difficult to measure. Upper and lower limits for the corrections to be applied to Table I are evaluated.

The estimated number of events in each channel, corrected for the biases and losses in the data analysis are presented in Table IV. The errors given are not due to the statistics but are sufficiently pessimistic to include the limits used on the corrections.

5.5. The detection efficiency of the apparatus

Consider a pion which interacts in the hydrogen target at a point $(x_o\ y_o\ z_o)$ producing $K_1^o\ K_1^o\ n$. The detection efficiency, η, is the probability that both K_1^o decays are observed inside a fiducial volume, $F(x, y, z) = 0$. It is a function of the position of the interaction point, the definition of the fiducial volume and also the kinematics of the event as specified by $(\underline{p}, \underline{p}')$ the laboratory momenta of the two kaons.

The factors contributing to η are discussed under the following headings:

i) Corrections for finite fiducial volume.

ii) Absorption of K^o and $\overline{K}^o$ in the target and anticoincidence counters.

iii) Absorption of neutrons in the target and anticoincidence counters.

iv) Absorption of incident pions along the target.

All calculations are specific to the $K_1^o\ K_1^o\ n$ final state. The extension to other channels is effected by substitution of the appropriate masses, lifetimes and cross-sections.

i) The fiducial volume and biases introduced by the counter geometry.

We define a fiducial volume bounded by the planes

$x = -85.0$; $x = 53.0$ cm.

$y = \pm 20.0$ cm.

$z = \pm 20.0$ cm.

(The origin is defined at the centre of the chamber.)

The plane $x = -85.0$ coincides with the end of the anti-coincidence counter and any decays before this plane should be suppressed by the trigger system. The other boundaries are chosen to allow a sufficient length of measurable track in the sensitive region of the chamber.

If L_3 and L_4 are respecitvely the lengths, measured from the interaction point, along the flight path of the decay to its entry into and exit from the fiducial volume then the probability that both decays occur within this region is

$$P_{(geom)} = \left| e^{\frac{-L_3 m}{pc\tau}} - e^{\frac{-L_4 m}{pc\tau}} \right| \cdot \left| e^{\frac{-L_3' m}{p'c\tau}} - e^{\frac{-L_4' m}{p'c\tau}} \right| \quad \ldots\ldots (5.2)$$

m and τ are the mass and lifetime of the K_1^o, p is its laboratory momentum.

We see from this expression that the system is biased against the detection of events with interaction point near the front (upstream) end of the target and events characterised by a K_1^o of low momentum or wide production angle.

ii) Absorption of K^o and $\bar{K}^o$

The K^o or $\bar{K}^o$ produced in the hydrogen target may experience a secondary interaction either in the hydrogen or in the lead and scintillator of the anticoincidence counters. Charged particles resulting from this interaction (elastic recoils and mesons produced in inelastic processes) are detected and the trigger is suppressed.

The survival probability against absorption is:

$$P\ (K^o\ \bar{K}^o\ \text{abs}) = e^{-(\mu_H L_2 + \mu_{Pb,CH} D)} \cdot e^{-(\mu'_H L'_2 + \mu'_{Pb,CH} D)}$$

μ_H is the absorption constant for K^o and $\bar{K}^o$ in liquid hydrogen.

$\mu_{Pb,CH}$ is the absorption constant for K^o and $\bar{K}^o$ in the Pb-scintillator sandwich.

Both μ_H and $\mu_{Pb,CH}$ are momentum dependent.

L_2 : the length of K^o flight path in liquid hydrogen.

D : the length of K^o flight path in the anticounter.

As no data exist on high energy $K^o p$ and $\bar{K}^o p$ cross sections we make the following assumption:

$$\sigma^T (K^o p) = \sigma^T (\bar{K}^o p) = \tfrac{1}{2} [\, \sigma^T (K^+ p) + \sigma^T (K^- p)\,]$$

For $K^{\pm}$ momenta between .5 GeV/c and 12 GeV/c

$$\sigma^T (K^+ p) \sim 17.5 \text{ mb} : [29] \text{ independent of } p$$

$$\sigma^T (K^- p) \sim (21 + \tfrac{20}{p}) \text{ mb} :$$

This expression is an approximate fit to the data of the groups given in reference 30 and 31.

i.e. $\sigma^T (K^o p) \sim (19.25 + \tfrac{10}{p})$ mb

Whence $\mu_H = \sigma^T (K^o p)\ \rho\ N_o \sim (8.25 + \tfrac{4.25}{p}) \times 10^{-4}\ \text{cm}^{-1}$

N_o : Avogadro's Number 6.025×10^{23}

ρ : Density of liquid hydrogen .071 gm/cc.

The anticoincidence counter is composed of 10 mm. Pb and 18 mm. Plastic Scintillator (the ratio of H atoms : C atoms is 1.1 : 1)

We obtain the composition of the counter:

No. of Hydrogen atoms/cm^2 = 8.9×10^{22} (n_H)

No. of Carbon atoms/cm^2 = 8.1×10^{22} (n_C)

No. of Lead atoms/cm^2 = 3.2×10^{22} (n_{Pb})

Hence for a K^o or $\bar{K}^o$ with direction cosines l, m, n traversing the counter

$$\mu_{Pb,CH}\, D = (n_H \sigma_H^T + n_C \sigma_C^T + n_{Pb} \sigma_{Pb}^T) / l$$

The cross sections are again momentum dependent. We take an average of

$\sigma_H^T \sim 21$ mb corresponding to a 5 GeV/c K^o

$\sigma_C^T \sim 160$ mb

$\sigma_{Pb}^T \sim 1520$ mb

(The values of σ_C and σ_{Pb} are taken from the calculations of Williams.[32] They differ widely from the $A^{2/3}$ rule).

This gives

$$\langle \mu_{Pb,CH}\, D \rangle \sim \frac{.065}{l} \pm 10\%$$

The survival probability against absorption of K^o and $\bar{K}^o$ in the anticoincidence counters and hydrogen target is

$$P(K^o\bar{K}^o \text{ abs}) = e^{-\left[8.25(L_2+L'_2) + 4.25\left(\frac{L_2}{p} + \frac{L'_2}{p'}\right)\right] \times 10^{-4}} \cdot e^{-.065\left|\frac{1}{l}+\frac{1}{l'}\right|} \quad \ldots\ldots (5.3)$$

(iii) Absorption of neutrons.

The neutron detection efficiency of the anticoincidence counter was studied by Colin West.[17] From the results of a Monte Carlo calculation he produces the curve shown in Fig. 5.5 of the neutron detection efficiency as a function of the four-momentum transferred to the neutron (~kinetic energy of the neutron). The variation over a wide range of neutron energies is not very large and we approximate the function by a constant detection efficiency of $.09 \pm .02$. We may write the survival probability against neutron absorption

$$P_{(n\ abs.)} = .91 \qquad \ldots\ldots (5.4)$$

(iv) Absorption of beam in target.

A correction for the effective loss of beam particles due to interactions in the target does not strictly enter into the detection efficiency, as it has been defined. However, the correction must be applied in the calculation of the cross section and it is conveniently incorporated in the detection efficiency.

The pion proton cross section at momenta ranging from 5 to 12 GeV/c is $\sigma^T (\pi^- p) \sim 29$ mb. If a pion travels a distance L along the target the probability against absorption

$$P\ (\pi^-\ abs.) = e^{-.0012\ L} \qquad \ldots\ldots (5.5)$$

By combining the results of equations (5.2).(5.5) we obtain the overall detection efficiency of the apparatus for the specified

event. A factor 4/9 is included as each K_1^o decays via the charged mode in the ratio 2:3.

$$\eta\,(X_oY_oZ_o\cdot\underline{p}\cdot\underline{p}')\;=\;\frac{4}{9}\,P_{(geom)}\cdot P_{(K^o\bar{K}^o abs)}\cdot P_{(n\ abs)}\cdot P_{(\pi^-\ abs)}\qquad\ldots(5.6)$$

We shall estimate the relative magnitudes of the above factors for a specific event in which two 6 GeV/c K_1^o's are produced at the centre of the target and emerge in the forward direction.

$P_{(geom)}$	:	0.2
$P_{(K^o\bar{K}^o\ abs)}$	:	0.83
$P_{(n\ abs)}$	:	0.91
$P_{(\pi^-\ abs)}$	:	0.97

It is evident in this example, and true in general, that the geometrical factor is the most significant in depressing the detection efficiency.

5.6 The Weight of an Event

The inverse of the detection efficiency, as evaluated above, is the weight which may be attached to an event, characterised by the vector momenta of the outgoing kaons and generated in the target at (x, dx)

$$W_x\,(x,\ \underline{p},\ \underline{p}')\;=\;1/\eta\,(x,\ \underline{p},\ \underline{p}')$$

The disadvantage of using the individual weight for an event is evident from Figure 5.6. The variation over the complete sample

of events is very large and two events, kinematically identical, may be weighted differently by factors of ten or more, simply because they were produced at different points in the target.

We state the problem in the following manner. One event, defined only by the kinematic variables, is observed. How many events of this type were produced in the target liquid?

We assume the events to be produced uniformly along the target at a rate n_o/cm. The number, dN, which are observed to originate from (x, dx)

$$dN = n_o \, dx \, \eta \, (x, \underline{p}, \underline{p}')$$

and from anywhere in the target

$$N = n_o \int_{Target} \eta \, (x, \underline{p}, \underline{p}') \, dx = 1.$$

The total number of events generated, observed and unobserved, is

$$n_o L_T = \frac{L_T}{\int_{Target} \eta \, (x, \underline{p}, \underline{p}') \, dx} = W$$

This number is the weight which we assign to the observed event. The geometry of the anticoincidence counter does not allow an analytic evaluation of the integral; a summation approximation is used.

$$W \, (\underline{p}, \underline{p}') = \frac{L_T}{\Sigma_i^{10} \eta_i \, (x_i, \underline{p}, \underline{p}') \, \Delta x}$$

η_i is the detection efficiency as given by (5.6), calculated at points x_i equally spaced along the target. Ten 4.1 cm. intervals were used. In Figure 5.6 the distribution of the weight function is compared with that of the individual weight. The range is greatly reduced.

5.7 Total Cross Sections

The total cross section for a process where N events are observed is given by

$$\sigma = \frac{\sum_{i=1}^{N} W_i}{N_o \rho \, \mathcal{N} \, L_T}$$

N_o : Avogadro's number. 6.023×10^{23}

ρ : Density of liquid hydrogen in the target.

L_T : Length of target, 41 cm.

$\mathcal{N}$: The effective number of incident pions. This implies a correction of 4 ± 1 % for electronics losses (see anticoincidence losses - Chapter 2.3)

The relevant figures for the 5,7 and 12 GeV/c data are listed in Table IV. The errors quoted for the $K_1^o K_1^o n$ total cross sections are due principally to uncertainty in the corrections applied. As shown above the factor $P_{(geom)}$ is the most important correction. To check this factor the cross sections are recalculated using a different definition of the fiducial volume. The results are

consistent (Table IV).

In Table V the $\Lambda\bar{\Lambda}n$ cross sections are listed. Statistics in this channel are not very high. At 5 GeV/c incident momentum the c.m. energy is only 70 MeV/c^2 above $\Lambda\bar{\Lambda}n$ threshold. The cross sections are in the range 100 $\rightarrow$ 500 nanobarns.

The apparatus could not detect (because of a vanishing detection efficiency) an event in which the neutron was emitted forward in the centre of mass system. In this respect the cross sections may be underestimated but no events of this type, which are characteristic of a baryon exchange process, have been observed in bubble chamber experiments.[33,34]

An estimate of the background, that is, events not produced in the hydrogen target, was obtained from data collected with an empty target. The rates were relatively high. Approximately 15 % of the target full rate was recorded at 5 GeV/c and 10 % at 7 GeV/c. It was stated in Chapter 2 that interactions in the mylar windows would contribute only 2 % so these results deserve some comment.

The detection efficiency for events produced in the window nearest to the anticounter is much higher than the average taken over the target.

A simple calculation of the factor P_{GEOM}, the decay survival probability, at 5 GeV/c for an event produced in the downstream mylar window gives 0.5 for the symmetric case with two K_1^o's of

equal momentum. The average, taken over the target, is 0.07. This difference enhances the background and the observed rate of 15% is seen to be consistent with a true background of 2 %. The effect diminishes as the incident momentum increases. The cross sections have been corrected accordingly.

Data from this experiment are combined with total cross section measurements at lower energies[34,35] and plotted in Figure 5.7 as a function of the incident laboratory momentum. The cross section follows the normal pattern of inelastic processes. It increases steadily above threshold, reaches a maximum and then, as other inelastic channels are opened, it drops to less than 10 microbarns above 7 GeV/c.

We may note that a measure of the cross section for the process

$$\pi^- + p \rightarrow K_1^o + K_1^o + n$$

gives no indication of the cross section for the process

$$\pi^- + p \rightarrow K^o + \bar{K}^o + n$$

which is contributed to by $K\bar{K}$ states of both positive and negative C parity.

TABLE I

HPD measurements

Incident beam momentum	5 GeV/c	7 GeV/c	12 GeV/c
Well measured events in fiducial volume	295	576	949
$K_1^o\ K_1^o\ n$ uniquely identified	252	487	771
$\Lambda\ \bar{\Lambda}\ n$ uniquely identified	1	14	30
$K_1^o\ \Lambda$ uniquely identified	2	0	1
$K_1^o\ K_1^o\ n$ / $\Lambda\ \bar{\Lambda}\ n$ hypotheses ambiguous	0	1	1
Events exhibiting one or more electron pairs	14	23	60
Unidentified events	26	51	86

TABLE II

HPD measurements

Incident momentum	5 GeV/c	7 GeV/c	12 GeV/c
Badly measured events in fiducial volume	153	228	343
$K_1^o\ K_1^o\ n$ uniquely identified	45	91	139
$\Lambda\ \bar{\Lambda}\ n$ uniquely identified	0	7	14
$K_1^o\ \Lambda$ uniquely identified	2	2	1
$K_1^o\ K_1^o\ n$ / $\Lambda\ \bar{\Lambda}\ n$ hypotheses ambiguous	0	0	3
Events exhibiting one or more electron pairs	22	21	44
Unidentified events	84	107	142

TABLE III

Digitised Table measurements

Incident beam momentum	5 GeV/c	7 GeV/c	12 GeV/c
Events rejected by HPD	248	459	450
Sample measured on Digitised Table	84	70	161
Events in fiducial volume	58	50	133
$K_1^o\ K_1^o\ n$ uniquely identified	27	28	68
$\Lambda\ \bar{\Lambda}\ n$ uniquely identified	0	0	1
$K_1^o\ \Lambda$ uniquely identified	2	4	3
$K_1^o\ K_1^o\ n$ / $\Lambda\ \bar{\Lambda}\ n$ hypotheses ambiguous	1	1	2
Events exhibiting one or more electron pairs	2	3	8
Unidentified events (well measured)	7	2	10
Unidentified events (badly measured)	19	12	41

TABLE IV

TOTAL CROSS SECTION : $\pi^- + p \rightarrow K_1^o + K_1^o + n$

Incident π^- momentum	5 GeV/c	7 GeV/c	12 GeV/c
No. incident $\pi^- \times 10^6$	750	1354	1585
V^oV^o events found in scanning	778	1359	1860
$K_1^o K_1^o n$ fits in fiducial volume well measured by HPD	252	488	772
Corrections :			
$K_1^o K_1^o n$ events from bad measurements	88 ± 43	141 ± 50	210 ± 70
$K_1^o K_1^o n$ events from HPD rejects	125 ± 42	230 ± 46	246 ± 56
$K_1^o K_1^o n$ events corrected for losses in data analysis	465 ± 60	859 ± 70	1228 ± 90
Correction factors :			
For neutral decays of K_1^o	2.25	2.25	2.25
For detection efficiency and absorpt.	25.1	13.6	7.1
For anticoincidence losses	$1.04 \pm .01$	$1.04 \pm .01$	$1.04 \pm .01$
For background (measured in target empty run)	$0.85 \pm .07$	$0.90 \pm .05$	$0.94 \pm .03$
$\sigma (\pi^- + p \rightarrow K_1^o + K_1^o + n)$	$18.0 \pm 2.5 \mu b$	$10.8 \pm 1.0 \mu b$	$7.0 \pm .8 \mu b$
Consistency check using small fiducial volume	19.5 ± 5 μb	$11.5 \pm 1.5 \mu b$	7.4 ± 1 μb

TABLE V

TOTAL CROSS SECTION : $\pi^- + p \rightarrow \Lambda + \bar{\Lambda} + n$

Incident π^- momentum	5 GeV/c	7 GeV/c	12 GeV/c
No. incident $\pi^- \times 10^6$	750	1354	1585
$\Lambda\ \bar{\Lambda}\ n$ fits in fiducial volume well measured by HPD	1	14	30
Corrections :			
$\Lambda\ \bar{\Lambda}\ n$ events from bad measurements	1 ± 1	10 ± 4	19 ± 7
$\Lambda\ \bar{\Lambda}\ n$ events from HPD rejects	2 ± 2	2 ± 2	3 ± 2
$\Lambda\ \bar{\Lambda}\ n$ events corrected for losses in data analysis	4 ± 3	26 ± 6	52 ± 10
Correction factors :			
For neutral decays of Λ, $\bar{\Lambda}$	2.25	2.25	2.25
For detection effiency and absorpt.	25	15 ± 4	11 ± 3
For anticoincidence losses	$1.04 \pm .01$	$1.04 \pm .01$	$1.04 \pm .01$
For background (measured in target empty run)	$.85 \pm .07$	$.90 \pm .05$	$.94 \pm .03$
$\sigma(\pi^- + p \rightarrow \Lambda + \bar{\Lambda} + n)$	$\sim 0.1\ \mu b$	$0.3 \pm .15 \mu b$	$0.5 \pm .2 \mu b$

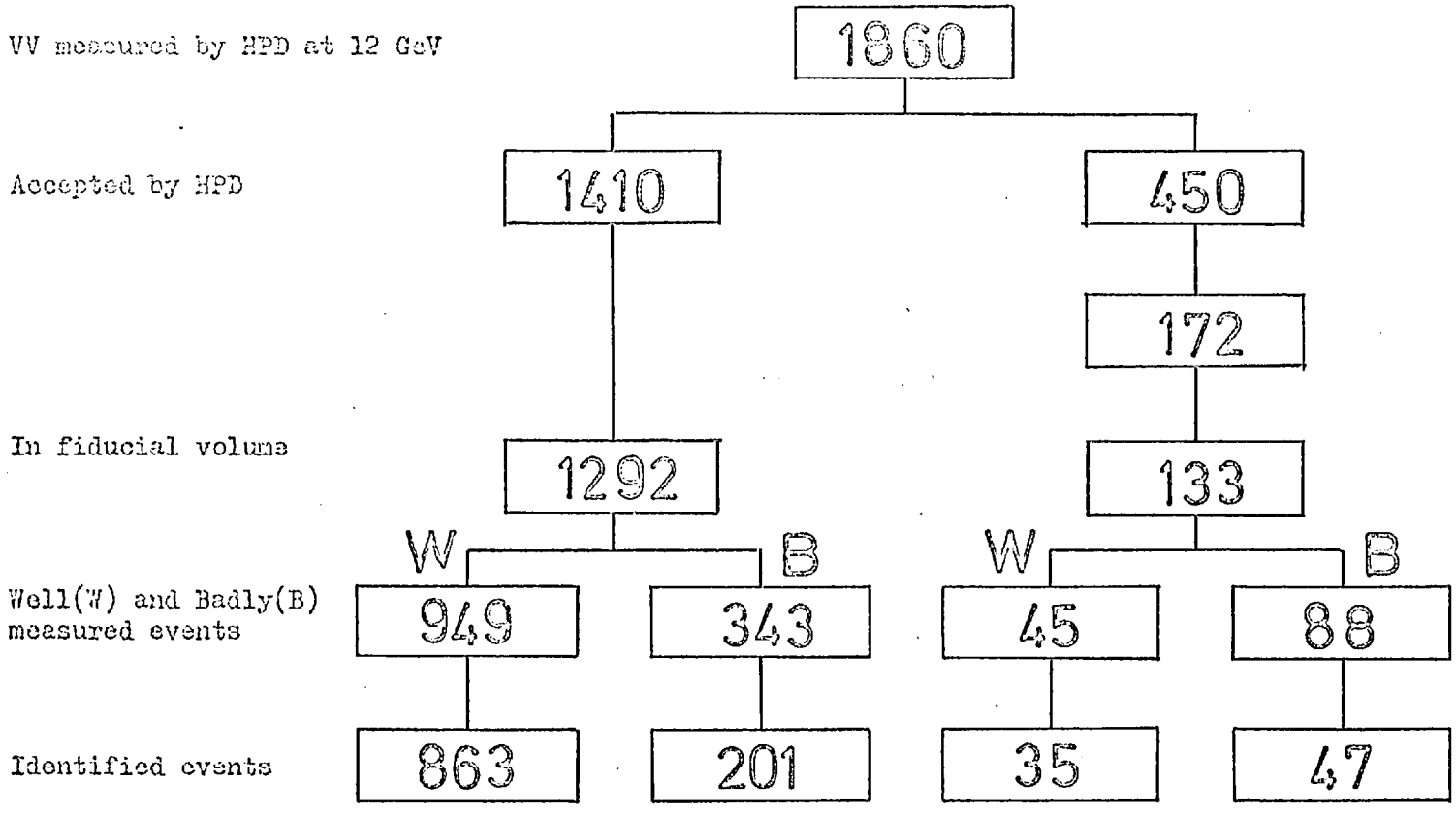

FIG.5.1 A history of 1860 photographs measured by HPD

FIG. 5.2 1-C χ^2 Distributions

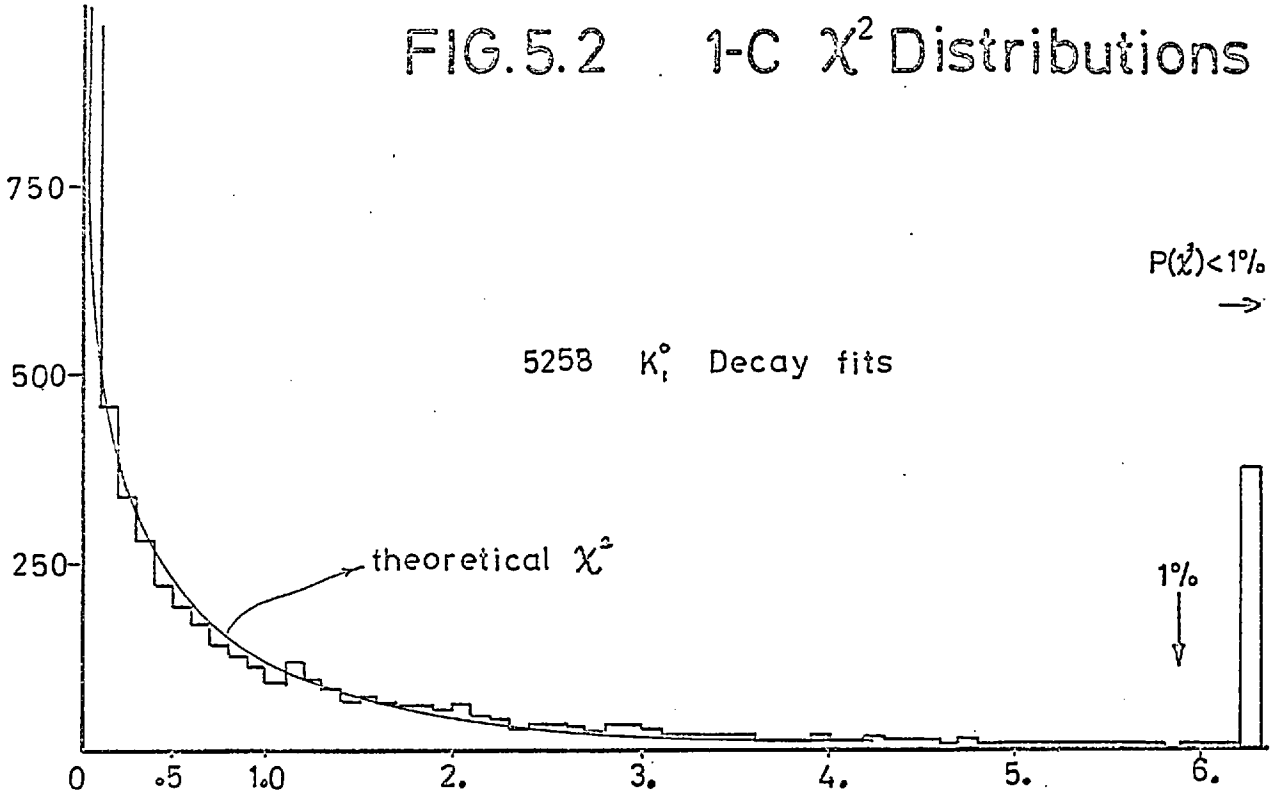

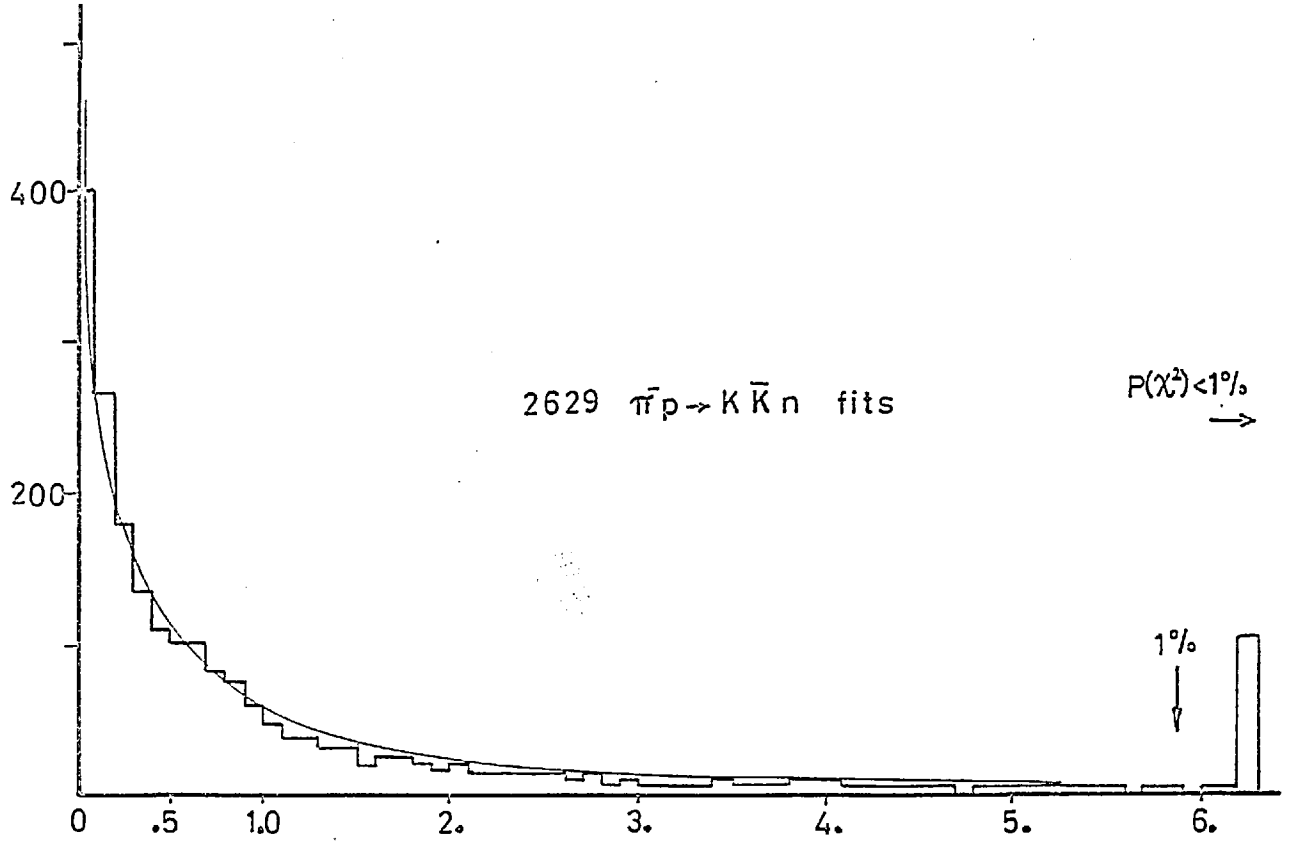

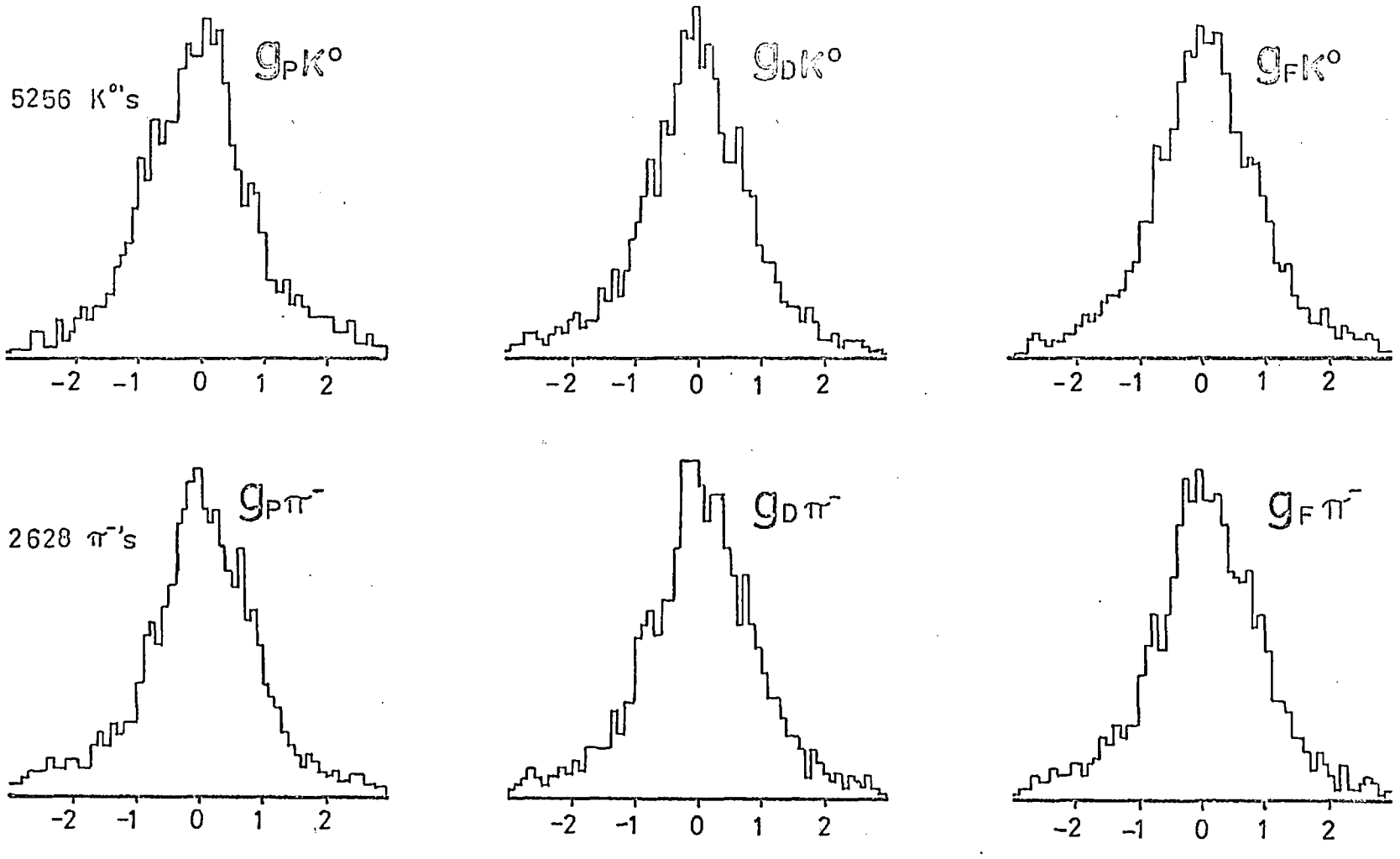

FIG. 5.3 $\pi^- p \to K\bar{K} n$ pull functions

P.... momentum
D.... dip, λ
F.... azimuth, ϕ

FIG.5.4

Missing mass distributions

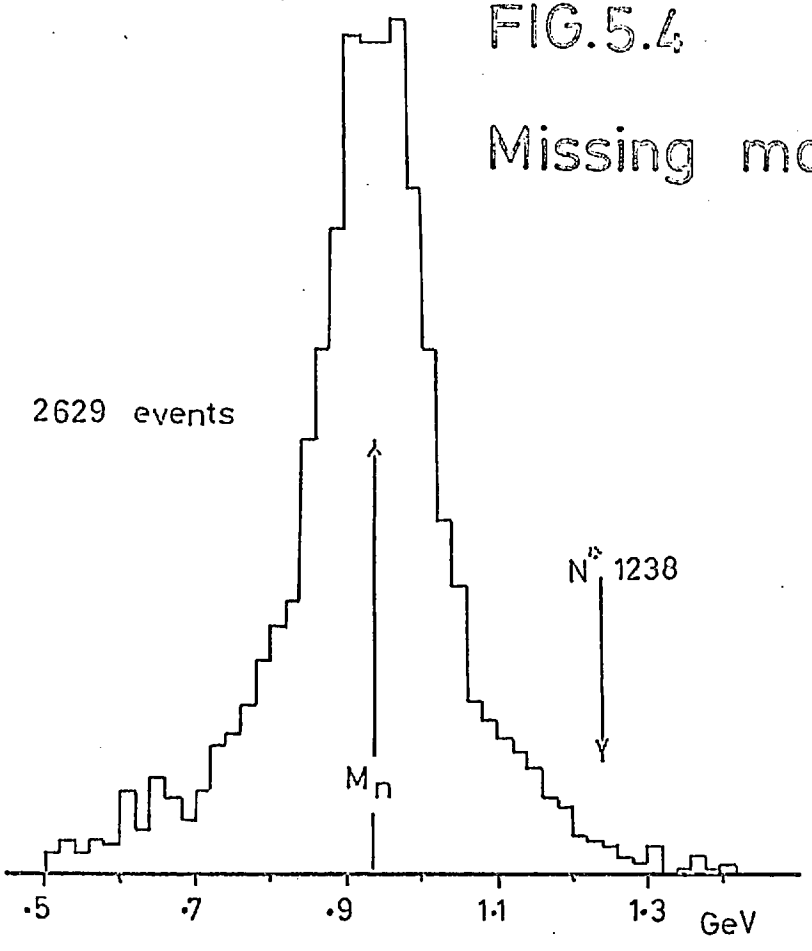

Missing mass recoiling against $K\bar{K}$

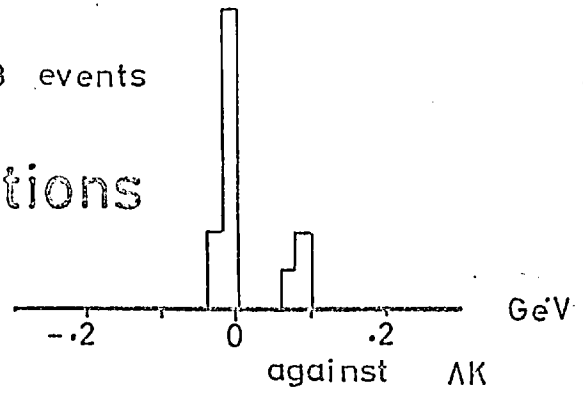

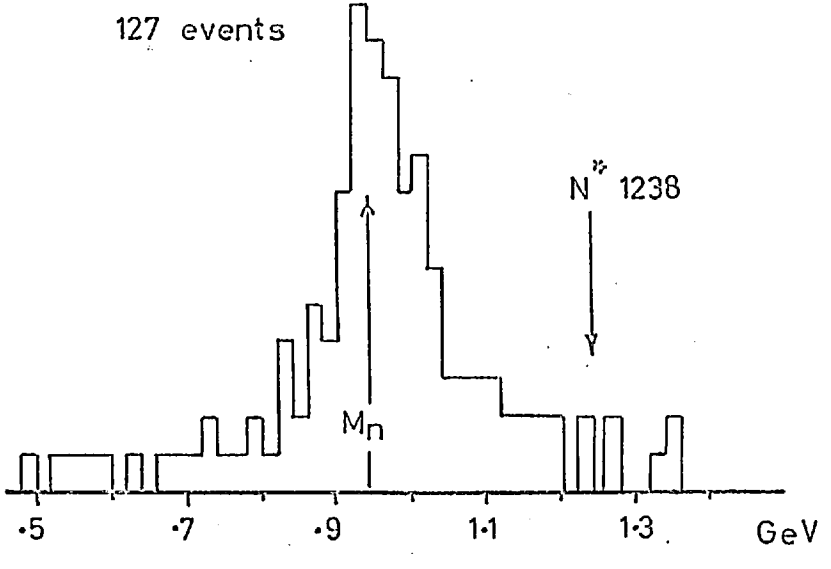

Missing mass recoiling against $\Lambda\bar{\Lambda}$

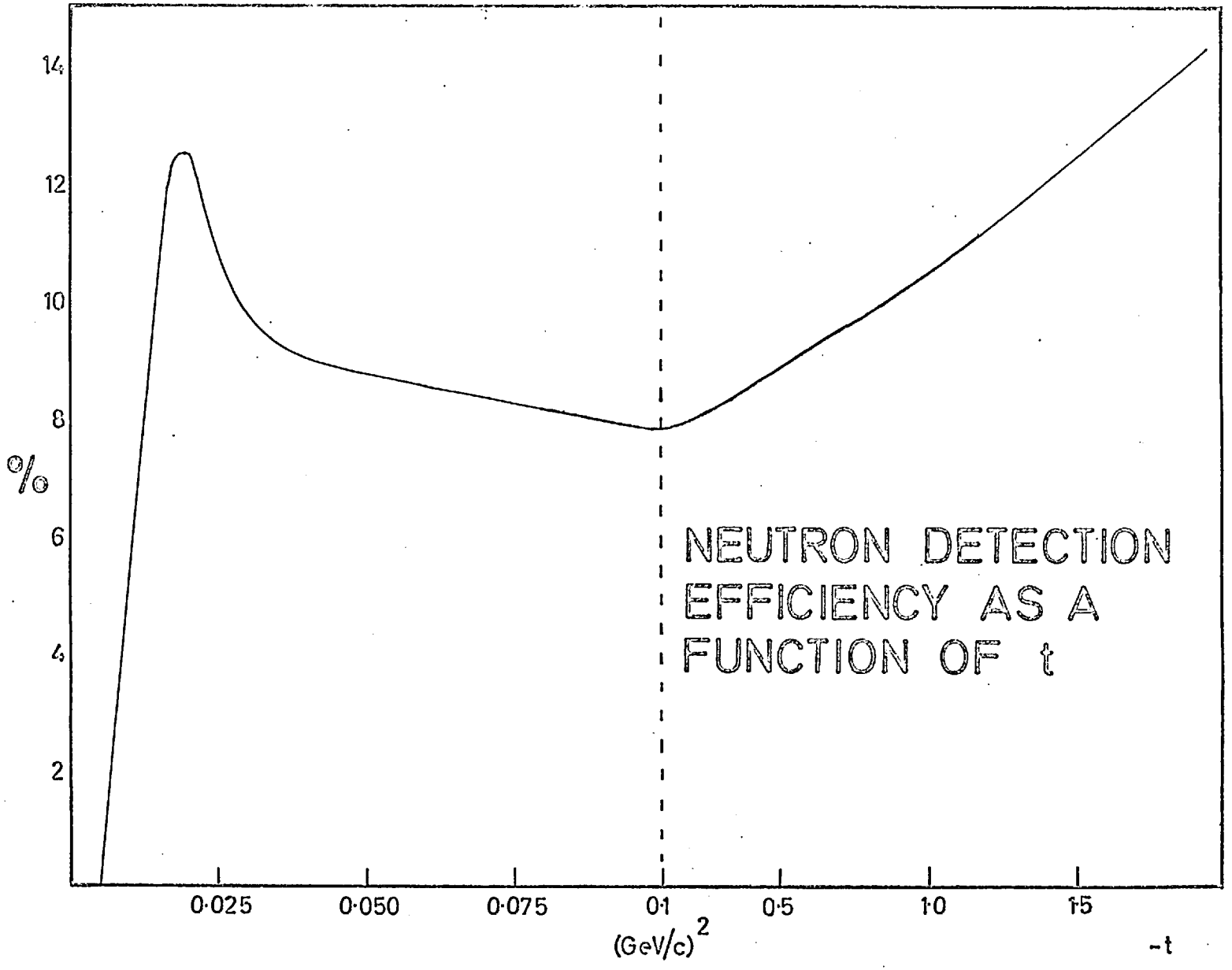
14
12
10
8
%
6
4
2
0·025
0·050
0·075
0·1
0·5
1·0
1·5
(GeV/c)^2
-t
NEUTRON DETECTION EFFICIENCY AS A FUNCTION OF t

FIGURE 5.5

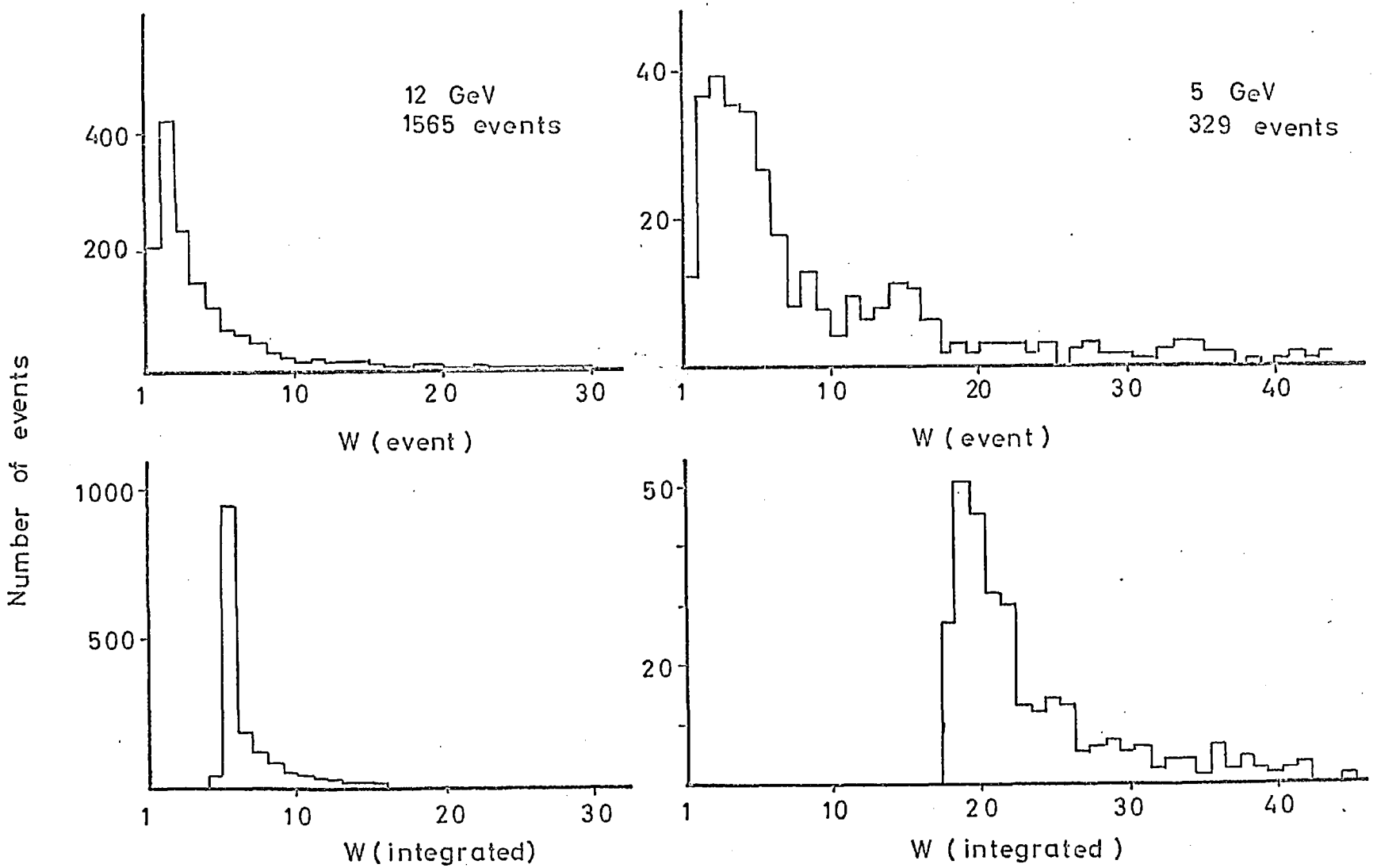

FIG.5.6 COMPARISON OF EVENT WEIGHT AND THE INTEGRATED WEIGHT FUNCTION

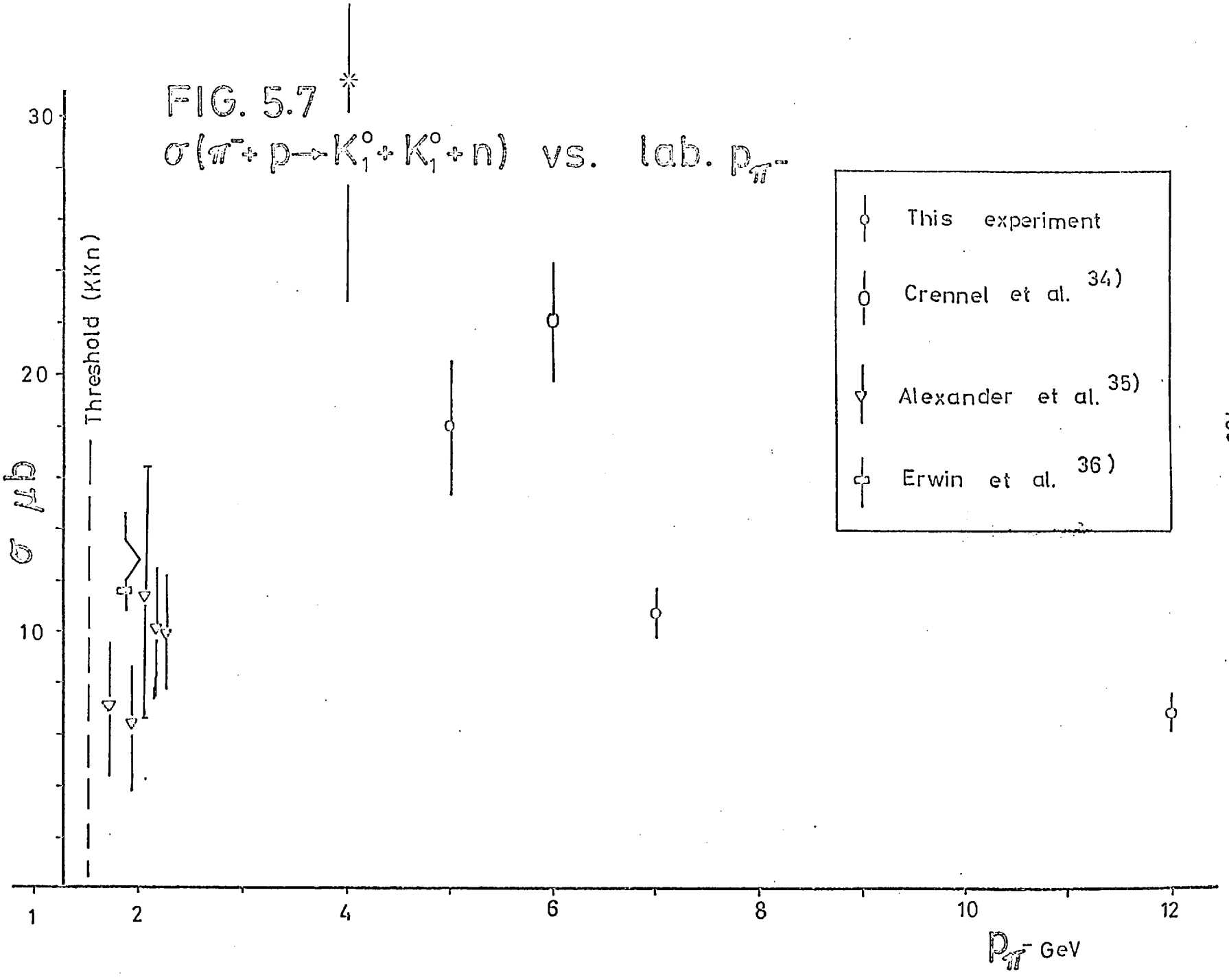
FIG. 5.7
$\sigma(\pi^- + p \rightarrow K_1^0 + K_1^0 + n)$ vs. lab. p_{π^-}
This experiment
Crennel et al. 34)
Alexander et al. 35)
Erwin et al. 36)
Threshold (KKn)
σ μb
p_{π^-} GeV
30
20
10
1
2
4
6
8
10
12

CHAPTER 6

Resonance production in $K_1^o K_1^o$ Final States

6.1. Introduction

The data presented in this chapter are relevant in a phenomenological description of high energy inelastic processes. The problem is to identify the final state and describe how it is produced. A simplification is introduced if the data can be separated into quasi-two-body interactions. The two body processes, it will be seen, are not always clearly defined and the methods which have been used to overcome these difficulties are described. This analysis invokes the use of a model which is not necessarily valid for all physical processes; if it were, then we should have a theory!

The invariant mass and angular distributions, corrected by the hand measured events (rejected by HPD), have been weighted according to the procedure described. The number of events in a particular distribution has been normalised to the number of events actually observed. Since the mean weight of an event is a slowly varying function across the distribution discussed, the statistical significance is indicated directly by the number of events per bin.

Dalitz plots for the final state $K_1^o K_1^o n$ are presented in Figures 6.1-3. One immediately sees that they are not uniformly populated. The $K_1^o K_1^o$ tends to be produced at low mass values. The projection onto the $M^2(K_1^o n)$ axis, however, does not exhibit any prominent features. The phase space curves shown are not the standard Lorentz invariant density of states distributions; they are model dependent and are calculated according to a simple recipe which is to be described below. The departures from 'phase space', most marked in the 12 GeV/c data, are statistically significant. This is attributed to a limitation of the model rather than a dynamic effect (the discrepancies depend on the incident energy and not on the invariant Kn mass). In particular, there is no evidence for the production of a $Y^* \rightarrow K_1^o n$.

In Figure 6.4 't', the squared four momentum transfer from proton to neutron, is plotted as a function of the invariant $K_1 K_1$ mass. The final state $K_1^o K_1^o n$ appears to be produced predominantly at very low momentum transfer to the neutron. The projection onto the t axis is shown in Figure 6.5. The corresponding centre of mass angular distribution is approximate (t is a function of $\cos \theta^*$ and the momentum in the final state c.m. system). It is presented to show how the $K\bar{K}$ system and the neutron are strongly collimated forward and backward respectively.

This is characteristic of an exchange in the 't channel' in which the $K\bar{K}$ is produced at the meson vertex. The data will be analysed within the framework of this peripheral process, the Feynman diagram for which is shown in Figure 6.6.

Before proceeding with a detailed study of the interaction we may try to discover the nature of the exchanged meson. When viewed in the rest system of the incident pion, the plane defined by the outgoing kaons is distributed around the direction of the exchanged particle in a manner depending upon the spin of that particle. The distribution of the Treiman-Yang angle is shown in Figure 6.6. It is isotropic. We conclude, since scalar exchange is forbidden by parity conservation, that the main features of the data are consistent with a one pion exchange model.

Figure 6.7 shows the distributions of the invariant $K_1^o K_1^o$ mass as obtained at each energy. The dotted line is the weight function. It increases steadily with the mass and enhances the number of events at 1400 MeV/c^2 by 30% relative to those at 1000 MeV/c^2. The error in the mass at 1400 MeV/c^2 is $\pm$ 13, $\pm$ 18, $\pm$ 23 MeV/c^2 at 5, 7 and 12 GeV/c respectively.

At each energy the significant features of the mass plot are the same. The events are concentrated below 1500 MeV/c^2 in two regions. One, a very broad peak at about 1300 MeV/c^2 and the other, much narrower, at about 1060 MeV/c^2.

6.2 Background

In the absence of resonance production the reaction proceeds directly to the three body final state. In order to estimate the proportion of the final state contributed by this non resonant background it has been usual practice to consider the form of the invariant mass distribution expected from a constant matrix element, the Lorentz invariant three body phase space. The peripheral model very definitely does not have a constant matrix element. We have, therefore, modified the phase space distribution so as to be consistent with this model.

The mass distribution, $d\rho/dM_{KK}$, obtained from the density of states factor, $\rho(E^*)$, can be evaluated analytically or simply by generating a large number of events randomly orientated in their centre of mass system. The characteristic feature of the peripheral model is the momentum transfer distribution which is approximately exponential in form. A large number of events were generated in a Monte Carlo programme. For each event the momentum transfer was calculated and the event weighted according to the experimental t distribution (Fig. 6.5). The invariant mass distribution obtained,

$$e^{bt} \frac{d\rho}{dM_{KK}},$$

is the 'peripheral phase space'. Its shape was found to be rather insensitive to the value of b. We have taken $b = 7$ $(GeV/c)^{-2}$ at each energy and superimposed the phase space curves on the $K_1 K_1$ mass distributions (Fig.6.7). The events with a mass higher than 1500 MeV/c^2 are consistent with the phase space. From the 5 GeV/c data it is estimated that background contributes 20% of the reaction. As the energy increases so does the background; it contributes 30% at 7 GeV/c and 40% at 12 GeV/c.

For an individual event it is not possible to say whether it is a direct reaction or a quasi-two-body process, i.e. resonance production. Since the resonance decay angular distributions play an important role in the one meson exchange model it is desirable to obtain unbiased decay distributions free from background. Two methods have been used.

We assume that the events with $M_{KK} > 1500$ MeV/c^2 are all direct reactions. Furthermore we assume that the angular distribution for the background K_1K_1 systems does not depend critically on their invariant mass. The angular distribution for the background can then be normalised to the 'phase space' in a resonance region, R, and subtracted from the overall angular distribution in this region. The result should be the decay angular distribution for R alone.

The second method involves a momentum transfer 'cut'. It is

seen from the Chew Low plots shown in Figure 6.4 that events with high M_{KK} are produced at higher momentum transfer than those with M_{KK} closer to threshold. By limiting the data to low momentum transfer we may hope to obtain a purer sample of the quasi-two-body processes. The data from all energies are shown in Figure 6.9 divided into those events with K_1K_1 systems produced at low t, $0 > t > -.14$ $(GeV/c)^2$, and at high t, $-.24$ $(GeV/c)^2 > t > -\infty$. Unfortunately the background is produced peripherally. By selecting the low t events we have reduced the relative number of background events but they have certainly not been eliminated. Two observations may be made however. The enhancement close to threshold is produced only at low t values. Secondly the very broad peak, which is about 250 MeV/c^2 wide at low t, is seen to be very much narrower at high t; $\sim$100 MeV/c^2 wide and centred at $\sim$1330 MeV/c^2.

6.3 The Broad Enhancement at $\sim$1300 MeV/c^2

Kinematic effects:

At least fifty per cent of the events are produced with the K_1K_1 invariant mass between 1200 and 1500 MeV/c^2. As we have seen in the preceeding section, this is not simply what is expected from the peripheral model. The phase space curve reaches a maximum above 1500 MeV/c^2 at each of the three incident momenta.

A broad enhancement can result from a resonance in another channel which is 'reflected'. The kinematic boundary of the Dalitz plot does not admit this explanation. Furthermore, no resonance in the $K_1^o n$ channel is observed.

In the past year there has been some attempt to account for observed peaks in the mass distributions of certain two particle subsystems of three particle final states. The explanation is based on the kinematics of a specific model involving an off mass shell diffraction scatter at one vertex of the one particle exchange diagram. The A1 (1080, principal decay mode $\pi\rho$), B (1220, $\pi\omega$) and K^* (1320, $K^*\pi$) if not definitely attributed to this so called 'Deck effect'[36] have their existence clouded by it. We note that each of those meson states is seen in a system of one stable (i.e. stable with respect to strong interactions) and one unstable particle; that is to say the ultimate observed final state contains four or more stable particles. The final state which concerns us consists of three stable particles, $K^o\bar{K}^o n$. We can think of no simple model in which the Deck effect could produce a broad enhancement at low $K\bar{K}$ mass. Parity conservation at the meson vertex forces a scattering vertex involving a vector meson - nucleon initial state and a pseudoscalar meson - nucleon final state. This cannot be a diffraction process; i.e. both diagrams shown below are forbidden.

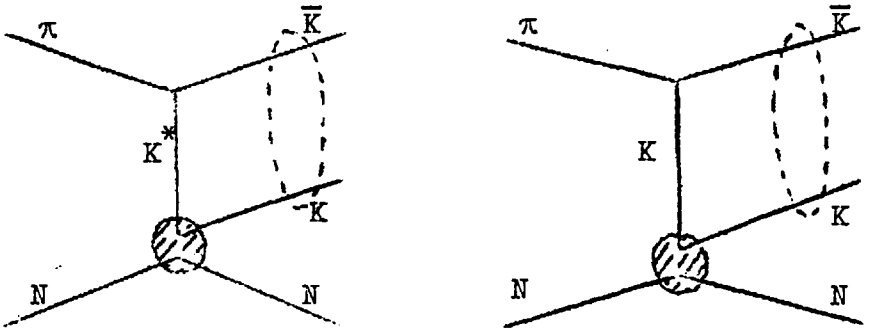

Having considered and rejected these kinematic interpretations we turn to the dynamics; in particular, the production of genuine resonances.

A fit to the data of Breit-Wigner peaks:

The width of the enhancement, about 250 MeV/c^2, is much greater than can reasonably be expected for a strongly decaying resonance. We discuss the possibility that the effect is due to the superposition of two or of three resonances.

If the cross section for the production of a stable particle of mass M is $\sigma_s(M)$ then, by modifying the calculation to include a propagator and decay amplitude, the cross section for the production of a resonant state can be written[37)]

$$d\sigma = \sigma_s(M) \frac{2}{\pi} \left[\frac{M M_o \Gamma(M)}{(M_o^2 - M^2)^2 + M_o^2 \Gamma^2} \right] dM \qquad (6.1)$$

$$= \sigma_s(M) \; B(M) \; dM$$

M_o is the mass of the resonance.

If the resonance decays via a partial wave of angular momentum l then

$$\Gamma(M) \sim \Gamma_o \left[\frac{q}{q_o}\right]^{2l+1} \qquad \ldots (6.2)$$

$\Gamma_o \equiv \Gamma(M_o)$ is the width of the resonance.

q is the momentum of each particle measured in the rest system of the decay.

$q_o = q(M_o)$

An attempt was made to fit two D-wave Breit Wigner peaks, B^1 and B^2, of the form given by equations (6.1) and (6.2) with $l = 2$. The polar decay angular distributions (Fig.6.13, 14 and discussed in the following section) do not admit the possibility that the two kaons are predominantly in an $l = 0$ state. It was assumed that the region of the KK mass plot defined by $1150 < M < 2600$ MeV/c^2 was contributed to by two resonances and background (phase space). The effective mass distribution can then be written

$$f(M) \sim \text{Phase space} \times (1 + \text{Resonances})$$

or, explicitly,

$$f(M) = e^{bt} \frac{d\rho}{dM} \left[1 + \sum_{i=1,2} \alpha^i \left[B^i (M, M_o^i \Gamma_o^i) - 1 \right] \right]$$

α^i are the relative contributions from each resonance.

$1 - \Sigma \alpha^i$ is the relative contribution from background.

The likelihood function (see Appendix 1) was generated and

the best values of the parameters M_o, Γ_o and α estimated from the data (the data, taken at each incident beam momentum were treated independently). The results of the calculations are shown below. They are inconsistent at different energies.

2 peak hypothesis		fraction of events	M MeV	Γ MeV
5 GeV	1	.39	1256	90
	2	.39	1336	95
7 GeV	1	.5	1294	100
	2	.13	1447	60
12 GeV	1	.15	1277	70
	2	.18	1356	75

It is concluded that two resonances do not explain this broad peak.

Two established resonances of even spin - parity may contribute: f (1254) and A2 (1290).* In Figure 6.87a shoulder (at 7 GeV/c a definite peak) is seen at about 1440 MeV/c^2.

* The J^P assignment of the A2 ($\pi\rho$) and its identity with the $K\bar{K}$ resonance at approximately the same mass is not settled.[38] The symbol A2 in the following discussion implies the resonance which decays into $K\bar{K}$.

This occurs at each energy and cannot be attributed either to kinematics or to a bias in the system. With the assumption that three resonances are present the maximum likelihood estimate of their parameters was found in the same way as for the two peak hypothesis. The mass and width of the f_o ($M = 1254$; $\Gamma = 100$ MeV/c^2) were fixed. Only one additional free parameter is present but the results obtained, shown in Table VI, are now consistent at each energy. For the A_2 meson we fit the mass and width : $M = 1335 \pm 10$, $\Gamma = 80 \pm 25$ MeV/c^2. The third peak, referred to in Table VI as 'G', occurs at a mass of 1435 ± 15 MeV/c^2 and has a width $\Gamma = 70 \pm 30$ MeV/c^2.* The mass of the f'(1500)[39] is very different from that of the peak we observe, and the simplest explanation of the data is to assume the existence of a zero strangeness resonance at $\sim$1435 MeV/c^2 with even spin-parity and $G = (-1)^I$. This is discussed more fully in section 6.6.

In conclusion, the broad enhancement is interpreted as a superposition of three resonant states (at 5 GeV/c the presence of f_o and A_2 alone is sufficient to explain the

---

* The errors derived in the likelihood analysis are strongly correlated and to quote the diagonal elements of the error matrix would be an underestimate. The errors given here are estimated from the spread of values for M and Γ obtained at different energies.

TABLE VI

Breit - Wigner fits to mass spectra :

Three peak hypothesis

Incident π^- momentum		Mass$_2$ MeV/c^2	Width$_2$ MeV/c^2	Fraction of events
5 GeV/c	f	<u>1254</u>	<u>100</u>	.35
	A	1328	80	.35
	G	1436	Consistent with zero production	
7 GeV/c	f	<u>1254</u>	<u>100</u>	.22
	A	1331	82	.25
	G	1451	53	.10
12 GeV/c	f	<u>1254</u>	<u>100</u>	.22
	A	1341	<u>80</u>	.26
	G	1435	70	.06
All data	f	<u>1254</u>	<u>100</u>	
	A	1334	<u>80</u>	
	G	1432	70	

The parameters underlined were fixed in the likelihood analysis.

data). The invariant $K\bar{K}$ mass for the combined data (Fig. 6.8) shows the contribution of each Breit-Wigner peak.

6.4 The f_o meson

The f_o meson, with a mass of 1254 MeV/c^2, is firmly established as an $I = 0$, $S = 0$ member of the 2^+ nonet. For this reason its mass and width were fixed in the analysis of the mass spectrum. From this analysis however, approximate values for the production cross section

$$\pi^- + p \longrightarrow f_o + n$$

$$\text{where} \quad f_o \rightarrow K_1^o + K_1^o$$

have been obtained.

P_{π^-} GeV/c	$\sigma\ (f_o \rightarrow K_1 K_1)$
5	$6\ ^{+1}_{-3}$ μb
7	$2.5\ ^{+.5}_{-1.2}$ μb
12	$1.5\ ^{+.3}_{-.6}$ μb

The $K_1^o K_1^o$ mode represents one quarter of the total $K\bar{K}$ decay of f_o (see Chapter 1.1). A comparison with the cross sections, at the same energy, for the process

$$\pi^- + p \longrightarrow f_o + n$$

or

$$\pi^+ + n \longrightarrow f_o + p$$

with the principal decay mode $f_o \rightarrow \pi^+ + \pi^-$

should give an estimate of the branching ratio

$$R_f = \frac{\Gamma\,(f_o \rightarrow K\bar{K})}{\Gamma\,(f \rightarrow \pi\pi)}$$

The only data for the f_o cross section known to me are the following:

P_π GeV/c	$\sigma\,(f \rightarrow \pi\pi)$	reference
3.2	465 ± 130 μb	Chung et al.[40]
4	630 ± 90 μb	ABBHHM[41]
6.1	220 ± 180 μb*	Viellet et al.[42]
6.1	410 ± 50 μb	Bruyant et al.[44]
8	250 ± 100 μb*	Orsay-Milan-Saclay[43]

Precise results are evidently excluded due to the extrapolation of these cross sections to the energies of this experiment. It was assumed that the cross sections, in each channel, should lie on a smooth curve as a function of energy, provided that the $K\bar{K}$ mode is multiplied by a factor corresponding to the inverse branching ratio R_f^{-1}.

* These figures are estimated from the $\pi^+\pi^-$ mass spectra. They are not quoted by the authors.

With only seven points it is not possible to fit a simple polynomial to the cross section curve and at the same time estimate R_f. Using only the qualitative requirement of smoothness the branching ratio obtained is

$$R_f = .04 \begin{matrix} +.03 \\ -.02 \end{matrix} \qquad \text{(see Fig. 6.10)}$$

(.07 should be regarded as an upper limit as it means that all events with M_{KK} in the f_o mass band are, in fact, f_o's).

This number can be compared with the present experimental upper limit of < 0.04[40] and the prediction of SU (3) (Glashow and Socolow[4]) assuming an f-f' mixing angle of 30^o ; $R_f = 0.024$. The decay $f \rightarrow K\bar{K}$ is forbidden in the static (i.e. $qq\bar{q}\bar{q}$ for spin 2) quark model.[45]

The f_o production angular distributions are shown in Figure 6.11. These are obtained after subtraction of the background from the events in the range $1170 < M_{KK} < 1280$ MeV/c^2 (the cut at 1280 MeV/c^2 is to reduce the overlap with the A_2). The forward diffraction-like peak can be parametrised by an exponential, exp (bt). The value of the parameter 'b' appears to increase as the energy increases. At 12 GeV/c $b = 7 \pm 1$ (GeV/c)$^{-2}$. In Figure 6.12 the variation of b along the mass spectrum is illustrated at different energies. The tendency for the peak to shrink with increasing energy appears not only at the f_o mass, but true in general.

The decay angular distributions, φ and $\cos\theta\,(\hat{p}_\pi \cdot \hat{p}_K)_f$, defined in the rest frame of the f_o are shown in Figure 6.13. The Treiman Yang angle, φ, is isotropic; consistent with pion exchange. The distribution of $\cos\theta$ is definitely not isotropic and so $J^P = 0^+$ for the f_o is excluded. It is, however, consistent with a quadratic in $\cos^2\theta$, as is expected from the next possible assignment, 2^+.

So far this is satisfactory, but if the shape of the $\cos\theta$ distribution is analysed there are some complications. The number of decays with $\cos\theta \sim 0$, i.e. perpendicular to the incident beam, is much larger than that expected in the pion exchange Born term model (BTM). In terms of the most general angular distribution for a $2^+ \to 0^-0^-$ decay (Appendix 4) the data require a large ρ_{22}. The dashed curve shown on the distribution is for $\rho_{22} = 0.4$ and $\rho_{oo} = 0.2$. The effects of absorption[46] do not shift the density matrix elements from the BTM values ($\rho_{22} = \rho_{11} = 0 : \rho_{oo} = 1$) by this amount, so it appears necessary, at first sight, to invoke a spin 2 exchange process at least as strong as the pion exchange.

There is, however, a much simpler explanation than this unattractive model. If there is some s-wave background which can interfere* with the f_o then the amplitude can be written,

---

* This explanation is used to account for the ρ^o decay asymmetry.[47]

assuming pion exchange:

$$A(\cos\theta) \sim Y_2^o + cY_o^o \quad (c \text{ is complex})$$

where $\frac{|c|^2}{1+|c|^2}$ is the proportion of s-wave background present.

The angular distribution then is

$$W(\cos\theta) \sim |A|^2 = \frac{45}{16\pi}(\cos^2\theta - \tfrac{1}{3})^2 + \frac{|c|^2}{4\pi} + \frac{3}{4\pi}\sqrt{5}\,\mathrm{Re}(c)(\cos^2\theta - \tfrac{1}{3}) \quad \ldots (6.3)$$

With $c = 0.6$ (i.e. $\sim 25\%$ background) and the phase of c such as to give completely destructive interference equation (6.3) gives good agreement with the observed angular distribution. This is shown by the solid curve in Figure 6.13. It is interesting to note that Lee et al.[48] when looking at the decay $f_o \to 2\pi$ found a lack of events at $\cos\theta \sim 0$, which, they say, indicates some constructive s-wave interference.

We shall now return to consider the production process. The differential cross sections as a function of t are shown in Figure 6.11. The dashed curve is the calculation from the BTM, as given in Appendix 3 (A.3.1). The familiar failings of this model are evident. The predicted angular distribution is much too shallow and the magnitude of the cross section perhaps ten times too high. The inclusion of absorptive effects considerably improves the situation. The solid curves shown (note the difference of the

vertical scales) are not fitted to the data but calculated using the following constants:

$\frac{g^2}{4\pi}(f\pi\pi) = 2.8$ from the f_o width

$\frac{G^2}{4\pi}(N\pi N) = 29$ for the charged pion-nucleon coupling

$R_f = .04$ to normalise the observed $\sigma(f_o \rightarrow K\bar{K})$ to the f_o production cross section.

The absorption parameters, which corresponded to total absorption in the final state, are the same as those used by Hogaasen et al.[46] in their analysis of 2^+ meson production at 4 GeV/c.

In spite of the improvement over the BTH the agreement is not complete. A factor $\sim 1\frac{1}{2} \rightarrow 2$ between theoretical and experimental cross sections remains and, especially at the higher energies, the predicted fall off with t is still not steep enough, requiring the inclusion of a t dependent form factor.

6.5 The A_2 meson

The tables of presently known particles[1] list the A_2 as a well established resonance with quantum numbers $I^G J^P = 1^- 2^+$. The principal decay mode is $\pi\rho$ and it has been observed in the $K\bar{K}$ and the $\pi\eta$ modes.

The basis of the spin-parity assignment, 2^{+-}, is the observation of the rare decay modes $K_1^o K_1^o$ and $K^- K^o$. Independent spin

analyses on the $\pi\rho$ data from many experiments have not given unique results. The possibilities are 1^+, 2^- and 2^+; some data even disagree with the assignment 2^+. [49] Measurements of the branching ratios

$$\frac{A_2 \rightarrow \eta\pi}{A_2 \rightarrow \rho\pi} \qquad \text{and} \qquad \frac{A_2 \rightarrow K\bar{K}}{A_2 \rightarrow \rho\pi}$$

at 3-to-4 GeV/c[50] and at 8 GeV/c[51] are inconsistent. Furthermore, the mass of the A_2 is not, at present, well defined. The range is 1260 MeV/c^2 to 1330 MeV/c^2 with a mean value of about 1320 MeV/c^2 for the $K^oK^\pm$ and about 1290 MeV/c^2 for the $\pi\rho$ system.

The argument, that the $K\bar{K}$ resonance is the same as the $\pi\rho$ resonance, based on the equality of their masses does not seem very compelling. In view of this $J^P = 2^+$ for the $\pi\rho$ system should not be preferred to 1^+ or 2^-. We preserve the name A_2 for the $K\bar{K}$, $I^GJ^P = 1^-2^+$ resonance.

From the Breit-Wigner analysis of the mass spectrum we fitted a mass and width to the A_2; $M = 1335 \pm 10$: $\Gamma = 80 \pm 25$ MeV/c^2. It is seen most prominently when the very low ($-t < .24$ (GeV/c)^2) momentum transfer events have been removed (see Fig.6.9); this suggests that the A_2 is not produced as peripherally as are the f_o and G. The A_2 cannot be produced via pion exchange; this violates

G parity. The production mechanism, probably ρ exchange, with a broader angular distribution, explains why the A_2 tends to be observed at relatively high momentum transfer.

Simple peripheral models do not agree with the experimental angular distributions. In the Born Term model the differential cross section increases with increasing t ! The absorptive modifications do predict a peak in the forward direction but the peak is not sharp enough and the predicted cross section an order of magnitude too high. The absorption model has invariably failed to agree with the data from high energy processes in which pseudoscalar exchange is forbidden. Even if a form factor is introduced the energy dependence is wrong.[46)]

The decay angular distributions (Fig.6.14) have been plotted only for the high momentum transfer events in the A_2 mass region. This cut has been applied to reduce the contribution from the overlapping f_o and G.

The cos θ decay distribution is not isotropic so we assert that the A_2 spin is ≥ 2. The form of this distribution in the case of vector exchange is given in Appendix 4 (A.4.2). There are, as in the case of the f_o, too many decays with cos $\theta \sim 0$ and it appears that interference from the background must again be disturbing the simple decay mechanism. Since this background will contain both S-wave and D-wave (from f_o) components a quantitative analysis

has not been attempted. The azimuthal angle, φ , shows no definite evidence of vector exchange.

To conclude this section on the A_2 it does not appear that the K_1K_1 resonance which we observe can definitely be identified with the $\pi\rho$ resonance at 1290 MeV/c^2. (Apart from the mass difference, a resonance exhibiting both decay modes violates the Bronzon-Low quantum number[52]). The decay distributions are disturbed by background and the proximity of the f_o. A more profitable channel for the observation of this resonance is in $(K\bar{K})^{\pm}$ final states where the f_o is absent.

The cross-sections for the process

$$\pi^- + p \rightarrow A_2 + n$$

$$\text{where } A_2 \rightarrow K_1^o + K_1^o$$

are given below as a function of the incident pion momentum. These cross-sections represent one twelfth of the total $K\bar{K}$ decay modes of an $I = 1$ resonance (see Chapter 1.1).

P_{π^-} GeV/c	$\sigma (A_2 \rightarrow K_1K_1)$
5	$6\ ^{+1}_{-3}$ μb
7	$2.8\ ^{+.6}_{-1.2}$ μb
12	$1.8\ ^{+.4}_{-.6}$ μb

6.6. An enhancement at 1435 MeV (E ?)

Armenteros et al.[53] in a study of stopping antiprotons, observed a strong accumulation at a mass of about 1420 MeV/c^2 in the neutral $K\bar{K}\pi$ system from the final state $K\bar{K}3\pi$. This they interpreted as the production of a resonant state, which they called the E. Its existence has been confirmed in $\pi^- p$ interactions by Miller et al.[54] From these data only the quantum number $I = 0$ can be determined.

In the $K\bar{K}$ mass distribution obtained from our experiment at 7 GeV/c incident pion momentum a significant peak was observed. This appeared as a shoulder at 5 and at 12 GeV/c. In the likelihood analysis a mass and width were fitted to this peak, which we called G : $M = 1435 \pm 15$ MeV/c^2 ; $\Gamma = 70 \pm 30$ MeV/c^2. The effect disappeared if only the high momentum transfer events were selected (Fig. 6.9).

From the information that can be obtained from this experiment on G, is it possible that, from what is known of the E, both effects may be attributed to the same particle? We shall first consider the data from this experiment.

G is seen in a state K_1K_1 so it has $J^P = 0^+, 2^+ \ldots$. furthermore its C parity is positive. Its production angular distribution is steeper than that of the A2 (see Figure 6.12) and the Treiman Yang angle is isotropic. This suggests pion exchange; i.e. the G couples to two pions and so $I = 0$. The $\cos\theta$ decay

distribution (Fig.6.14) has the form expected for a particle of spin 2 produced via pion exchange but this evidence should not be too highly valued owing to the high background and overlap with the A2 peak. However, we can say definitely:

$$J^P = 0^+,\ 2^+ \ldots \text{ etc.}$$

$$C = +$$

$$G = (-1)^I$$

and the evidence favours:

$$I^G J^P = 0^+\ 2^+$$

Recent results from the CERN-Paris-Liverpool collaboration[55] confirm the existence of the E in $p\bar{p} \rightarrow K\bar{K}\,3\pi$ annihilations. Moreover the decay mode $K_1^o\,K_1^o\,\pi^o$ is observed thus fixing the C parity as positive. They measure the mass : 1425 ± 7 MeV/c^2.

Montanet in a review of this work[55] considers the annihilation $p\bar{p} \rightarrow E^o\,\pi^o\,\pi^o$ from the ^1S_o (C = +) protonium and concludes that J^P (E) = 0^- is most probable, but 1^+ cannot be excluded. So we can say definitely for the E meson:

$$I = 0$$

$$C = +$$

and the evidence favours :

$$J^P = 0^-$$

Two decay modes of the E, K^*K and $(K\bar{K})\pi$ are seen. In the latter the $K\bar{K}$ system peaks close to threshold, indicating a

relative $K\bar{K}$ s-state. Coupling the $(K\bar{K})$ with a π produces the series $J^P(E) = 0^-, 1^+, 2^-$ etc. but there is one complication. In the $(K\bar{K})$ system of the E decay the K angular distribution is not isotropic, as would be expected from an s-state. If in fact this is a d-state (a p-state is excluded for K_1K_1) then an $l = 1$ coupling of a 2^+ $(K\bar{K})$ with a π can give a resultant $J^P(E) = 2^+$.

In conclusion, there is no definite reason to exclude the possibility that the peak we observe, G, is a $K\bar{K}$ decay mode of the E meson. This would fix the quantum numbers $I^GJ^P = 0^+2^+$ (if we neglect spin 4 and higher). The possibility would be confirmed by the observation of a 2π decay mode of the E, though not necessarily excluded by its absence.

6.7 The enhancement close to threshold : S^*

It was noted earlier, in the introduction to this chapter, that a peak in the K_1K_1 mass spectrum was observed near threshold. This effect is particularly evident at very small momentum transfers (Fig.6.9).

With the exception of one bubble chamber experiment, analysed by Crennel et al.[34] earlier published data of $K_1^0 K_1^0$ production in $\pi^- P$ interactions are obtained at energies much lower than the present experiment. The data of Bigi et al.[33] at 10 GeV/c contains 27 events with K_1K_1 in the final state; but that final

state contains both charged pions and an unknown number of neutrals.

The K_1K_1 mass plot close to threshold (996 MeV/c^2) in Figure 6.15 presents the data from references 35, 40 and 56. The enhancement, reported by the groups individually to occur between threshold and 1025 MeV/c^2, can be adequately explained using a simple pole approximation with the one pion exchange model.

The differential cross section may be written (Chew and Low[57])

$$\frac{d^2\sigma}{dt\, dM^2} = \frac{G^2}{2\pi} \cdot \frac{M\, k_\pi}{m_\pi^2\, p^2} \left[\frac{-t}{(m_\pi^2 - t)^2} \right] \quad \sigma(\pi\pi \rightarrow K\bar{K})$$

G : the coupling constant at the $N\pi N$ vertex.

σ : the $\pi\pi \rightarrow K\bar{K}$ cross section at energy M in the c.m. system.

k_π (k_K) : the initial (final) state momentum in the $\pi\pi$ ($K\bar{K}$) c.m. system.

In the zero effective range approximation the absorption cross section is given by[58]

$$\sigma(\pi\pi \rightarrow K\bar{K}) = \frac{4\pi}{k_\pi} \left[\frac{k_K}{k_\pi} \right] \frac{2b_o}{(1 + b_o k_K)^2 + (a_o k_K)^2}$$

With $A_o = a_o + ib_o$ the I = 0, S-wave $K\bar{K}$ scattering length. (D-wave scattering, close to threshold is neglected).

Substitution of this cross section in the Chew Low formula and integration over the angular distribution gives

$$\frac{d\sigma}{dM} \sim G^2 M^2 \left[\frac{k_K}{k_\pi} \right] \frac{b_o}{(1 + b_o k_K)^2 + (a_o k_K)^2}$$

where $k_K^2 = \frac{M^2}{4} - m_K^2$

and $k_\pi = \frac{1}{2M}\left[M^4 - 2M^2 (m_\pi^2 - t) + (m_\pi^2 - t)^2 \right]^{\frac{1}{2}}$

$\simeq \frac{M}{2}$ at small $(-t << M)$ momentum transfers.

A scattering length of $4 \pm i\ 0.4$ Fermi is drawn on the low energy data. The agreement is satisfactory indicating a strong $K\bar{K}$ interaction.

We have tried to explain the enhancement observed in our data in terms of this effect. In Figure 6.16 the threshold region of the K_1K_1 mass distribution is shown (after subtraction of the f_o). A momentum transfer cut of $-t < .14$ $(GeV/c)^2$ is applied, consistent with the approximation $-t << M$ used in the evaluation of the momentum, k_π, in the $\pi\pi$ cm system.

The best fit to the data is $A_o = 1.8 \pm i\ 0.4$ Fermi, with a chi square probability of $< 1\%$. The shape of the mass spectrum is sensitive to a_o only. The imaginary part effectively determines the normalisation, i.e. the $\pi\pi \rightarrow K\bar{K}$ cross section. Several scattering lengths are superimposed on the experimental mass distribution in Figure 6.16. None explain, even qualitatively, the data. Values of a_o less than one Fermi give too broad a peak. Increasing a_o sharpens the peak but the threshold rise is too severe.

An s-wave Breit-Wigner peak, fitted to the same data gives $M = 1050 \pm 6$ MeV/c^2 ; $\Gamma = 100 \pm 15$ MeV/c^2. The chi-square probability is 40%.

It is concluded that the data are not explained by a large $K\bar{K}$ scattering length but by the production of a K_1K_1 resonance. The Treiman-Yang and cos θ decay distributions (Fig.6.14) are isotropic and hence consistent with a state of $I^GJ^P = 0^+0^+$, produced by pion exchange. We identify this state with the S^* observed by Crennell et al.[34)]

6.8 The f' meson

The f' meson, seen in $K\bar{K}$ and $K\bar{K}^*$ final states, occurs at a mass of about 1500 MeV/c^2 [39)]. Its quantum numbers, $I^GJ^P = 0^+2^+$, are based on the observation of the K_1K_1 decay mode. Since a singlet meson, of this mass, fits very nicely into the 2^+ nonet its existence has been more readily accepted than some other resonances which have a firmer experimental foundation.

If we refer to Figure 6.7 it is seen that there is no enhancement at 1500 MeV/c^2. In fact, there are very few events in this region and we can say that the cross section for f' production in this experiment is less than 1.5 microbarns at 5 GeV/c and less than 0.5 microbarns at 12 GeV/c. These limits are for the K_1K_1 decay mode of the f'.

The cross section for the process

$$K^- + p \longrightarrow f' + \Lambda$$

$$f' \longrightarrow K_1K_1$$

at 5 GeV/c is about 22 μb.[39)]

If one assumes that in the K^- experiment the f' is produced by K exchange and that in our π^- experiment it is produced (if at all) by π exchange then the relative differential cross sections are, in the Born approximation

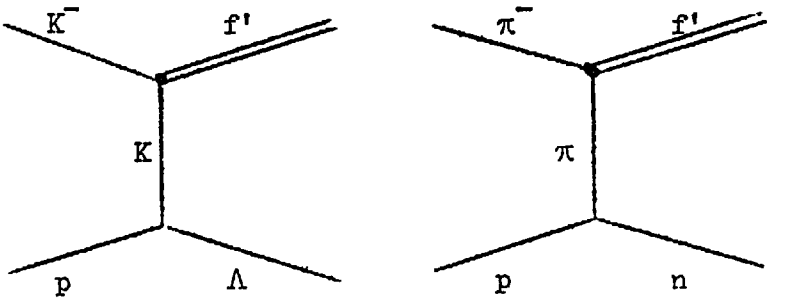

$$\left(\frac{d\sigma}{dt}\right)_\pi \Big/ \left(\frac{d\sigma}{dt}\right)_K \sim \frac{G^2_{N\pi N}\, g^2_{f'\pi\pi}}{m_\pi{}^2} \Big/ \frac{G^2_{NK\Lambda}\, g^2_{f'K\bar{K}}}{m_K{}^2}$$

The kinematic factors at the $2^+0^-0^-$ and $\frac{1}{2}^+\frac{1}{2}^+0^-$ vertices are similar in both Feynman graphs (Appendix 3). The propagator term, $(m^2 - t)^{-1}$, which favours pion exchange to kaon exchange, has been included.

$$\frac{g^2_{f'\pi\pi}}{g^2_{f'K\bar{K}}} \sim \left(\frac{\sigma_\pi}{\sigma_K}\right) \cdot \frac{G^2_{NK\Lambda}}{G^2_{N\pi N}} \cdot \frac{m_\pi{}^2}{m_K{}^2}$$

Using the value $\dfrac{G^2_{N\pi N}}{G^2_{NK\Lambda}} = \dfrac{2 \times 14.6}{5.9}$ [59]

(a factor two appears for the charged pion coupling)

we obtain $\dfrac{g^2_{f'\pi\pi}}{g^2_{f'K\bar{K}}} \lesssim 10^{-3}$

whence $\dfrac{\Gamma\ (f' \to \pi\pi)}{\Gamma\ (f' \to K\bar{K})} \lesssim .005$

(phase space factor used is p^5/m^2)

This very naive calculation has at least shown that the f' couples very weakly to two pions. The small branching ratio obtained would explain the fact that the $f' \to 2\pi$ decay has not been observed, although the phase space is favourable. The predication, from SU (3), for the branching ratio is .05[4]; this figure is, however, very sensitive to the input data: $\Gamma\ (A2 \to K\bar{K})/\Gamma(A2 \to \pi\rho) = .06$ which must be regarded as uncertain.

SUMMARY

At incident momenta ranging from 5 to 12 GeV/c the reaction

$$\pi^- + p \longrightarrow K^o + \bar{K}^o + n$$

is observed in highly peripheral collisions. In terms of the one meson exchange model the $K\bar{K}$ system is produced at the meson vertex, with the nucleon acting as a'spectator'. Quasi-two-body channels dominate the final state although the separation of these channels is not always clear. The S^*, close to the $K\bar{K}$ threshold is interpreted as an $I^GJ^P = 0^+0^+$ resonance rather than as a large $K\bar{K}$ s-wave scattering length. The f_o and A_2 are strongly produced; there is also evidence of a K_1K_1 enhancement at 1435 MeV/c^2 which we suggest may be a decay mode of the E meson. The separation of these three effects has complicated the task of making comparisons with the absorption model predictions of their production and decay angular distributions. The f_o production is consistent with one pion exchange when the effects of interference with an s-wave background are considered. The absorption model, with ρ exchange, fails to explain the A_2 production angular distribution.

The f' meson is not observed. We assume this is due to a small $f'\pi\pi$ coupling which depresses the production of f' in a one pion exchange mechanism. Branching ratios

for $f_o \longrightarrow K\bar{K}$ / $f_o \longrightarrow \pi\pi$ and $f' \longrightarrow \pi\pi$ / $f' \longrightarrow K\bar{K}$ have been estimated from the data. In so far as the SU(3) predictions of these ratios are based on uncertain experimental data (the $A_2 \longrightarrow K\bar{K}$ / $A_2 \longrightarrow \rho\pi$ ratio) the agreement is reasonable.

An experiment with similar high statistics on the process

$$\pi^- + p \longrightarrow K^o + K^- + p$$

$$\text{or} \quad \pi^+ + p \longrightarrow K^+ + \bar{K}^o + p$$

should reveal only the iso-vector $K\bar{K}$ states. A comparison with these data would reduce the problem of separating the f_o and A_2. This is, unfortunately, not yet a feasible proposition for a bubble chamber experiment and the development of a selective trigger for spark chambers would be very difficult.

The production of $\Lambda\bar{\Lambda}$ pairs in the reaction

$$\pi^- + p \longrightarrow \Lambda + \bar{\Lambda} + n$$

is analogous to the production of $K\bar{K}$ pairs. The collisions are peripheral with the neutron emerging in a backward direction in the centre of mass. The $\Lambda\bar{\Lambda}$ effective mass spectrum does not exhibit any significant features (Fig.6.17); the concentration of events at low mass results from the peripheralism. In particular, there is no evidence for the production of a heavy boson which could decay into a $\Lambda\bar{\Lambda}$ pair.

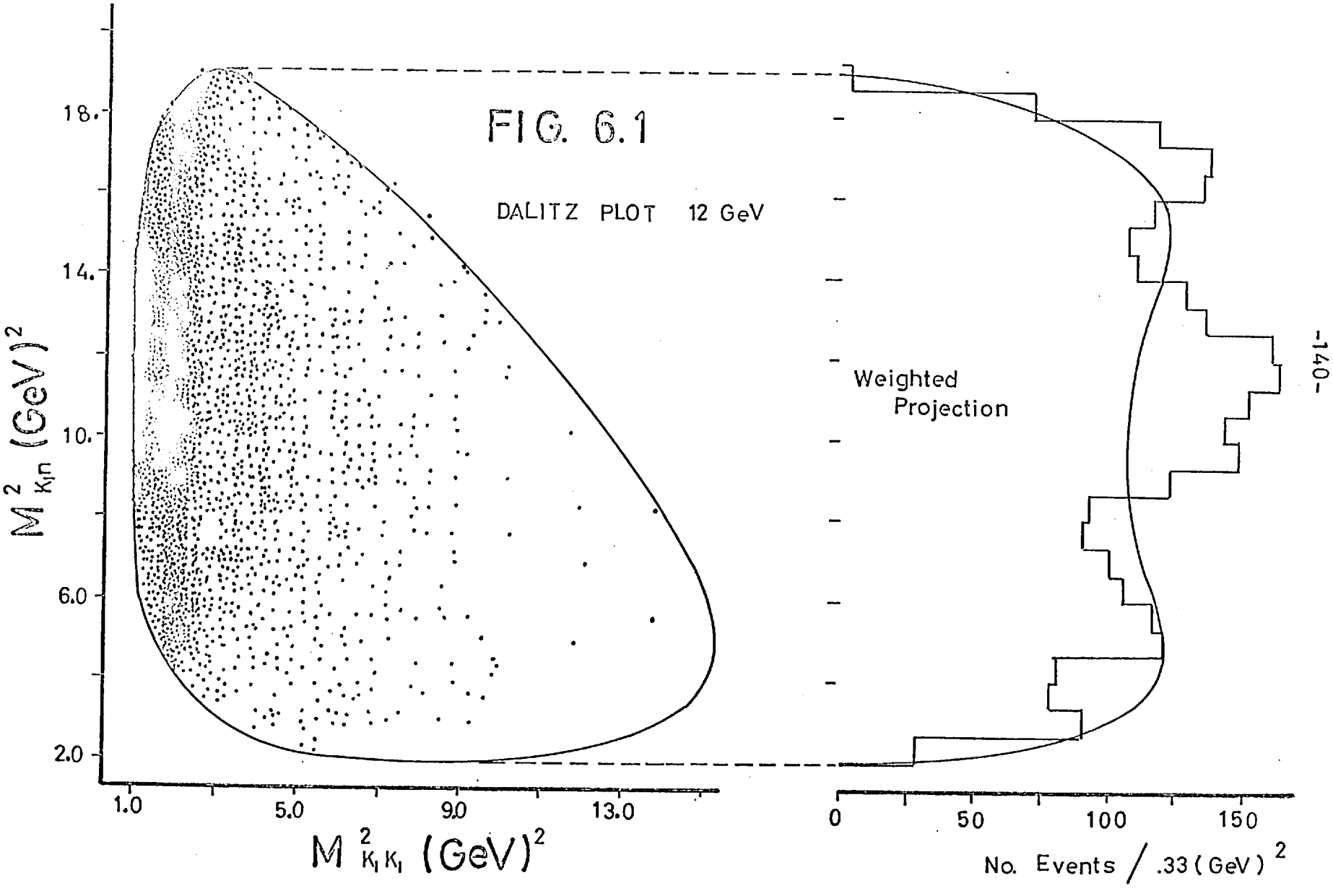
FIG. 6.1
DALITZ PLOT 12 GeV
Weighted Projection
18.
14.
10.
6.0
2.0
$M^2_{K_1 n}$ (GeV)^2
1.0
5.0
9.0
13.0
$M^2_{K_1 K_1}$ (GeV)^2
0
50
100
150
No. Events / .33 (GeV)^2

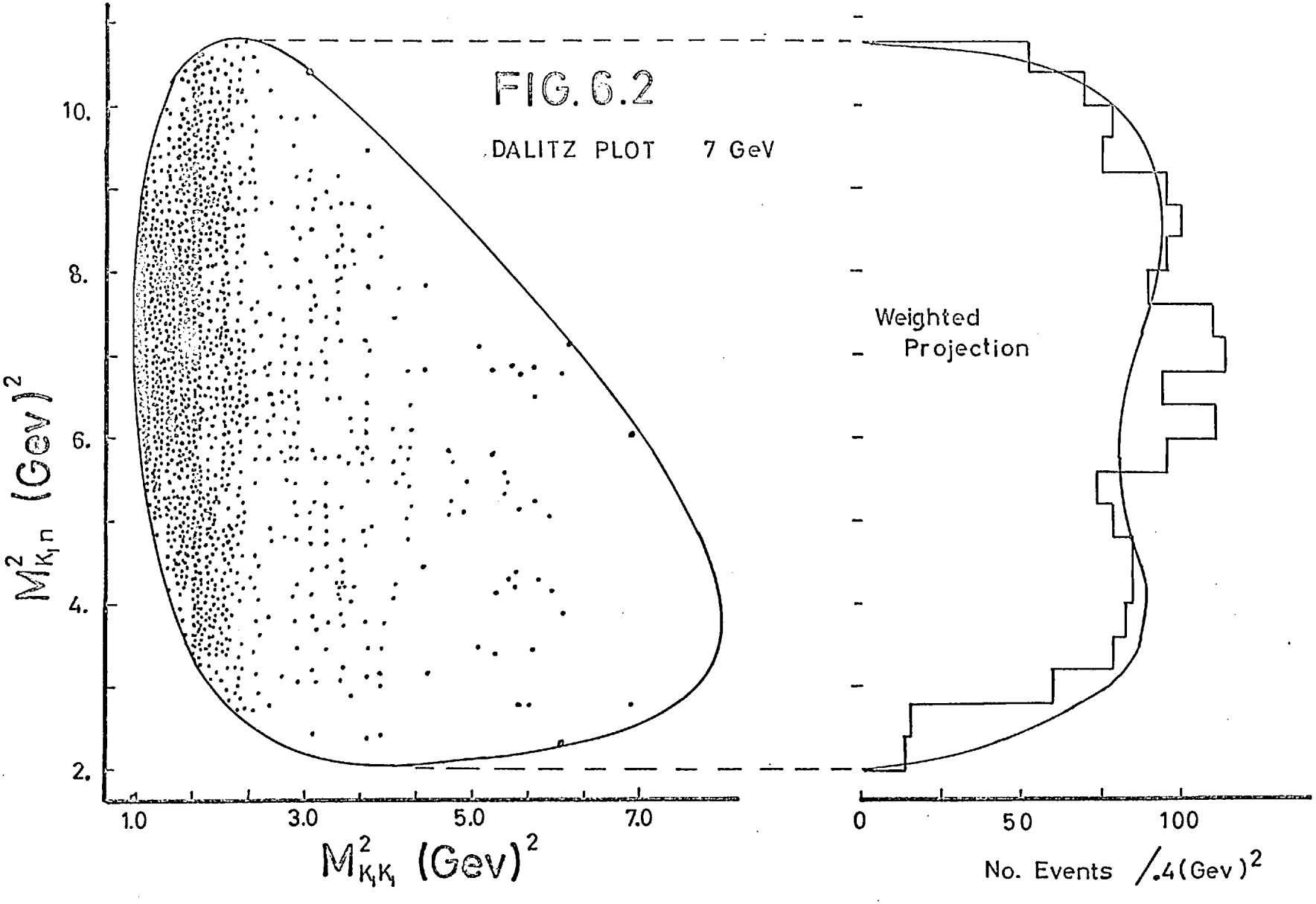
FIG. 6.2
DALITZ PLOT 7 GeV
Weighted Projection
$M^2_{K_1 n}$ (Gev)^2
$M^2_{K_1 K_1}$ (Gev)^2
No. Events /.4(Gev)^2
10.
8.
6.
4.
2.
1.0
3.0
5.0
7.0
0
50
100

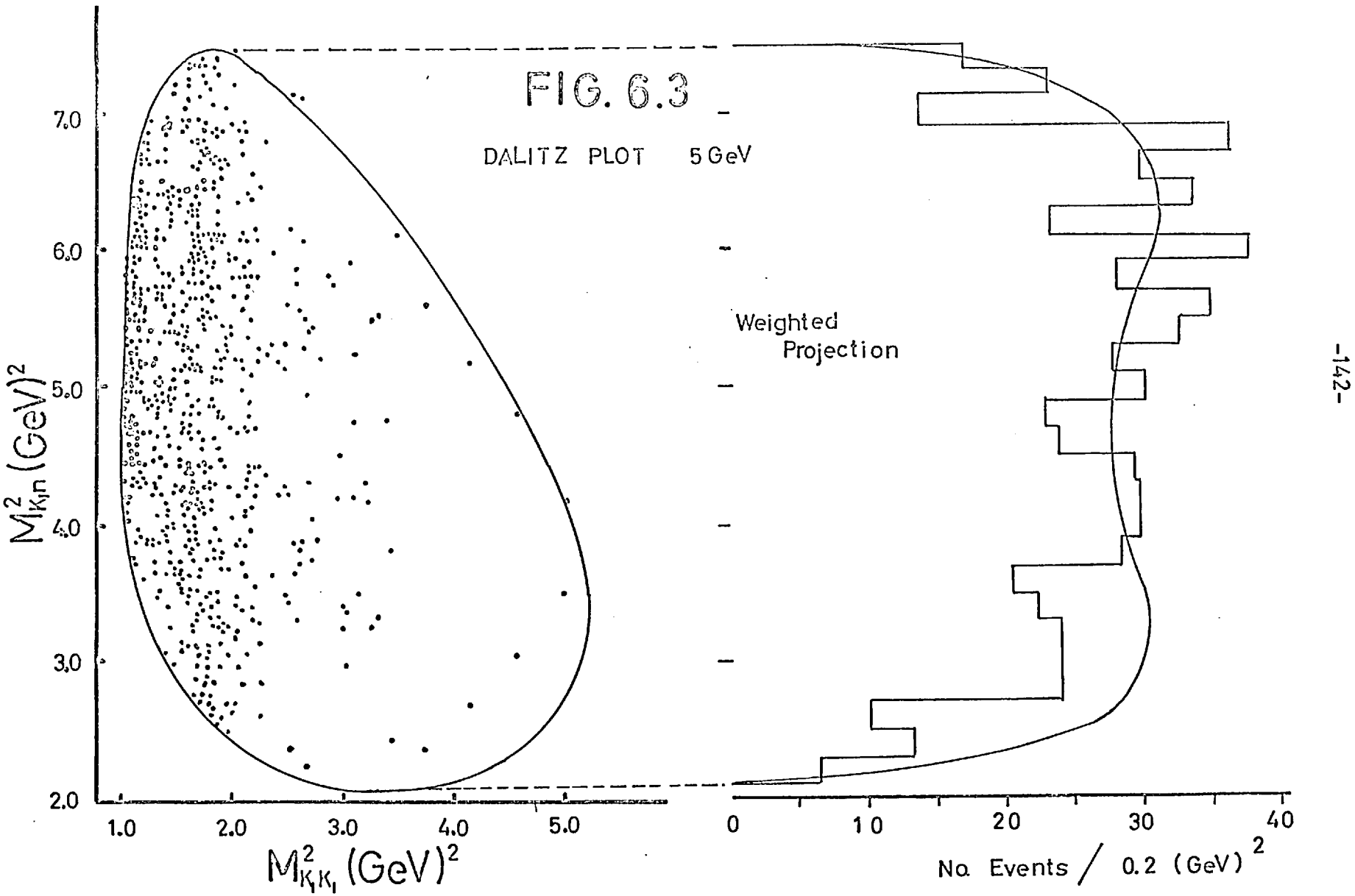
FIG. 6.3
DALITZ PLOT 5 GeV
Weighted Projection
$M^2_{K_1 n}$ (GeV)^2
$M^2_{K_1 K_1}$ (GeV)^2
No. Events / 0.2 (GeV)^2
7.0
6.0
5.0
4.0
3.0
2.0
1.0
2.0
3.0
4.0
5.0
0
10
20
30
40

FIG. 6.4 Chew-Low plots $K\bar{K}n$

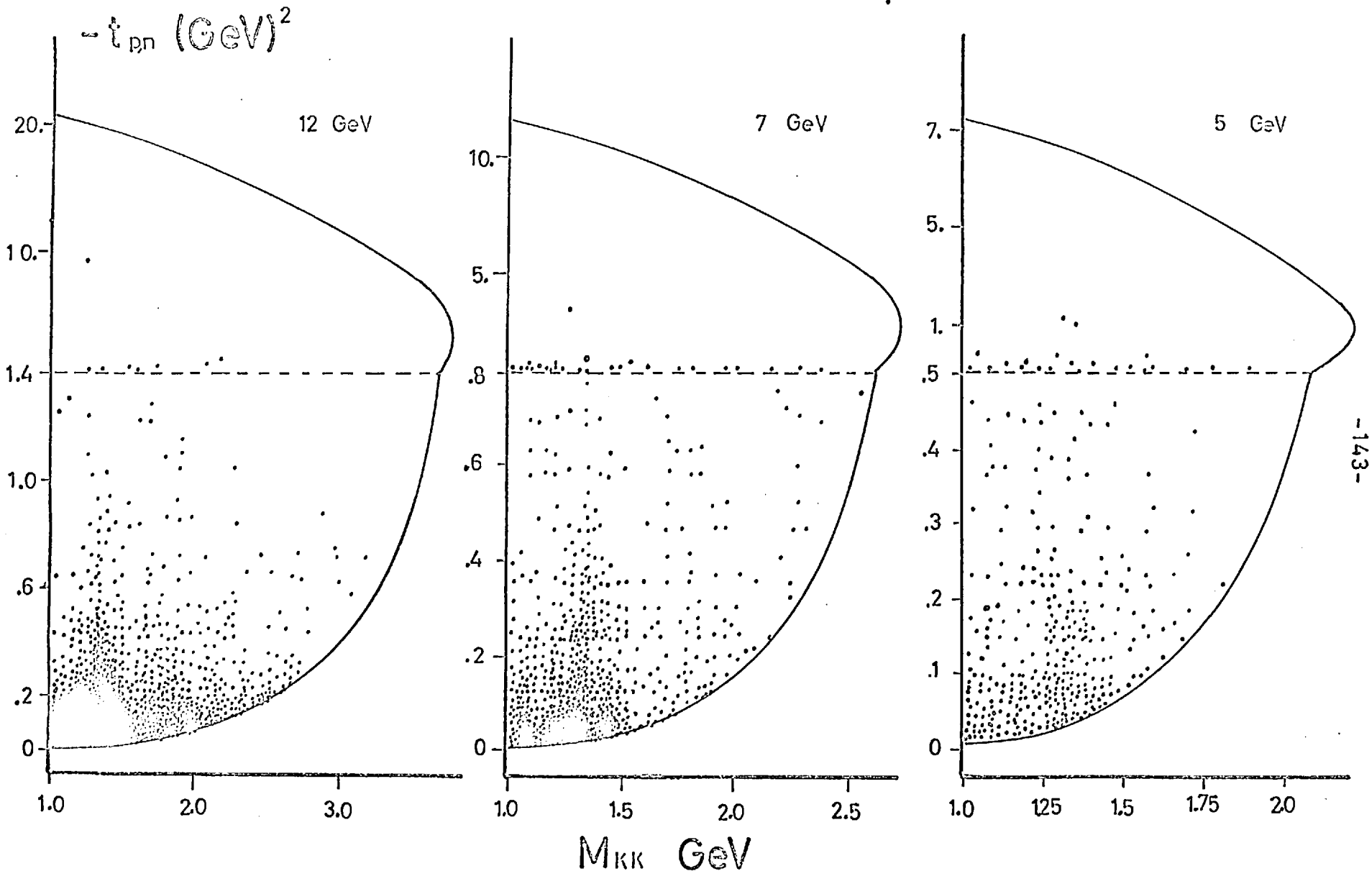

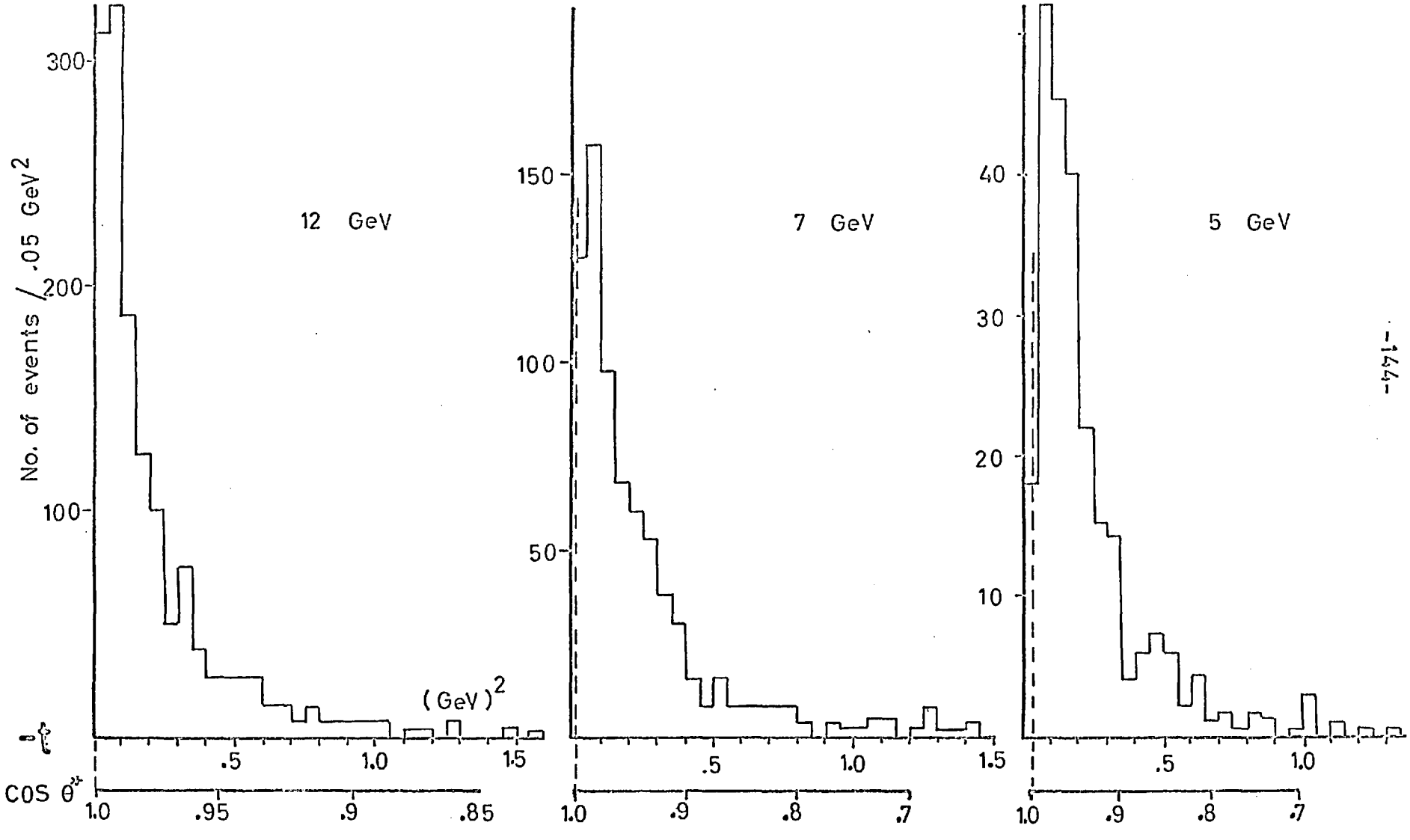

FIG. 6.5 t and c.m. production angular distribution of $K\bar{K}$

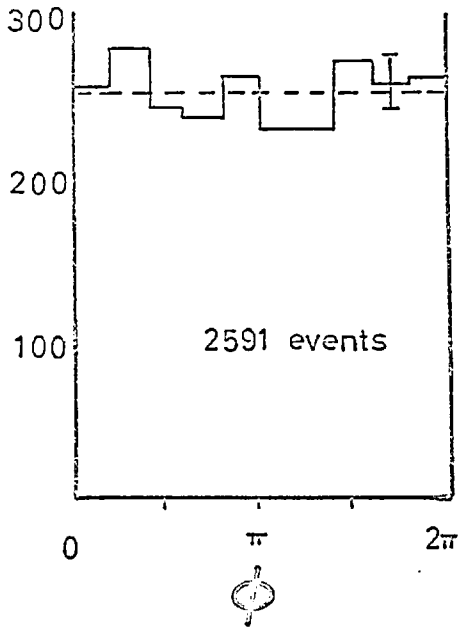

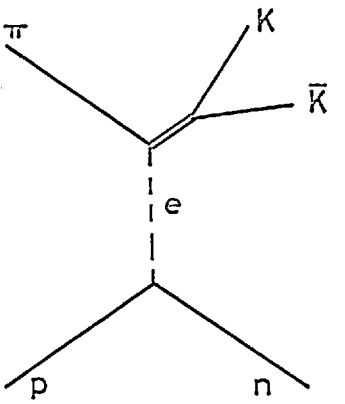

Incident beam (and exchanged particle)

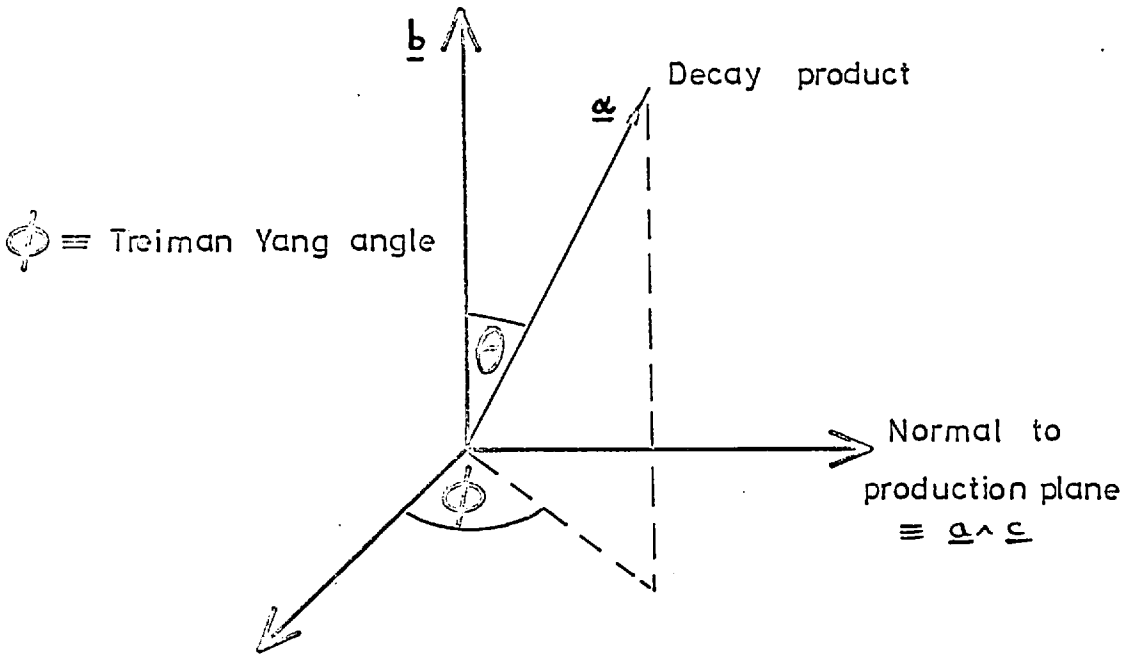

FIG. 6.6

THE DECAY ANGLES IN THE $K\bar{K}$ REST SYSTEM

FIG. 6.7

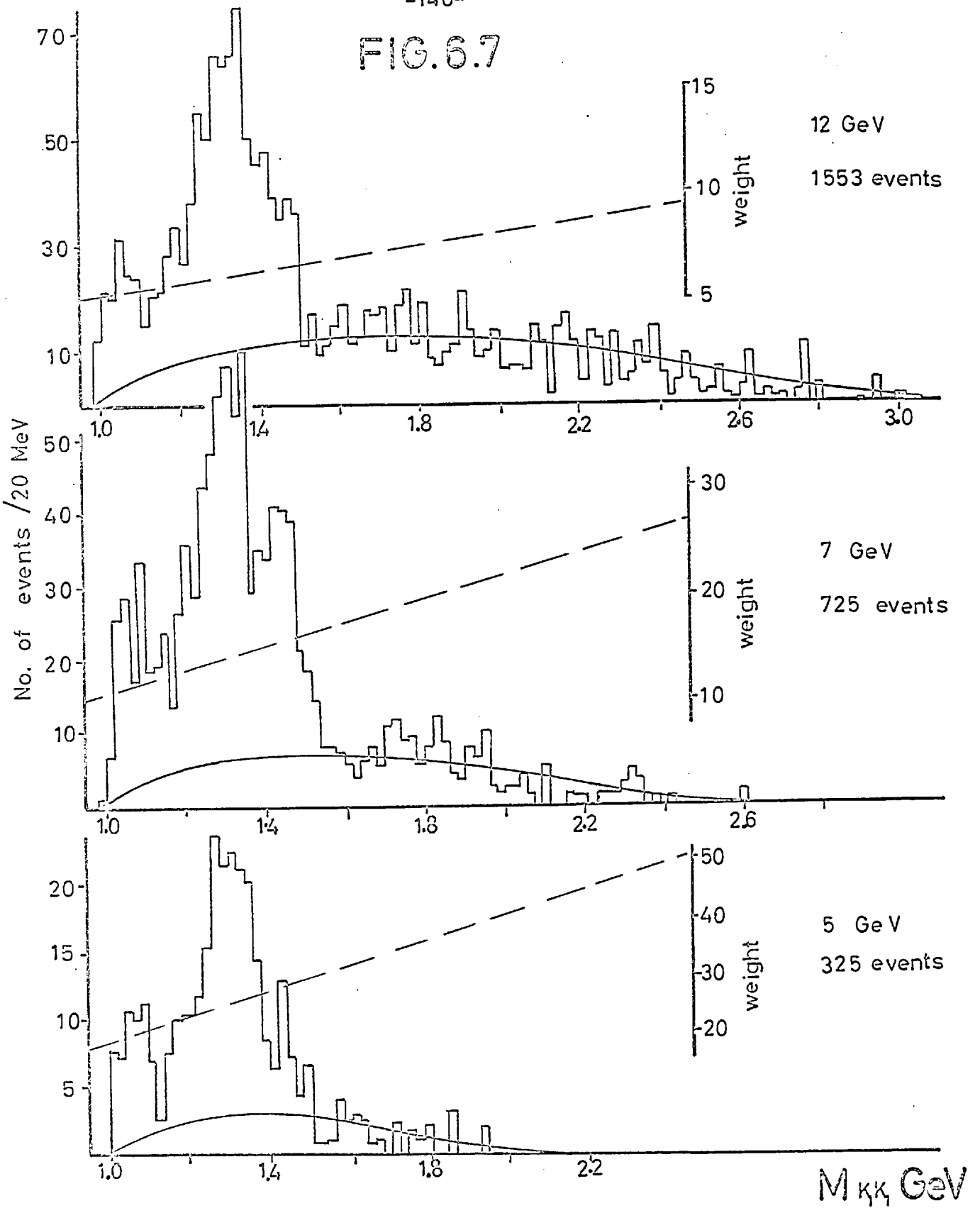

Mass of $K_1^0 K_1^0$

WEIGHTED HISTOGRAMS
Solid curves represent peripheral phase space

FIG. 6.8
weighted M_{KK} distribution
all data combined 2627 events

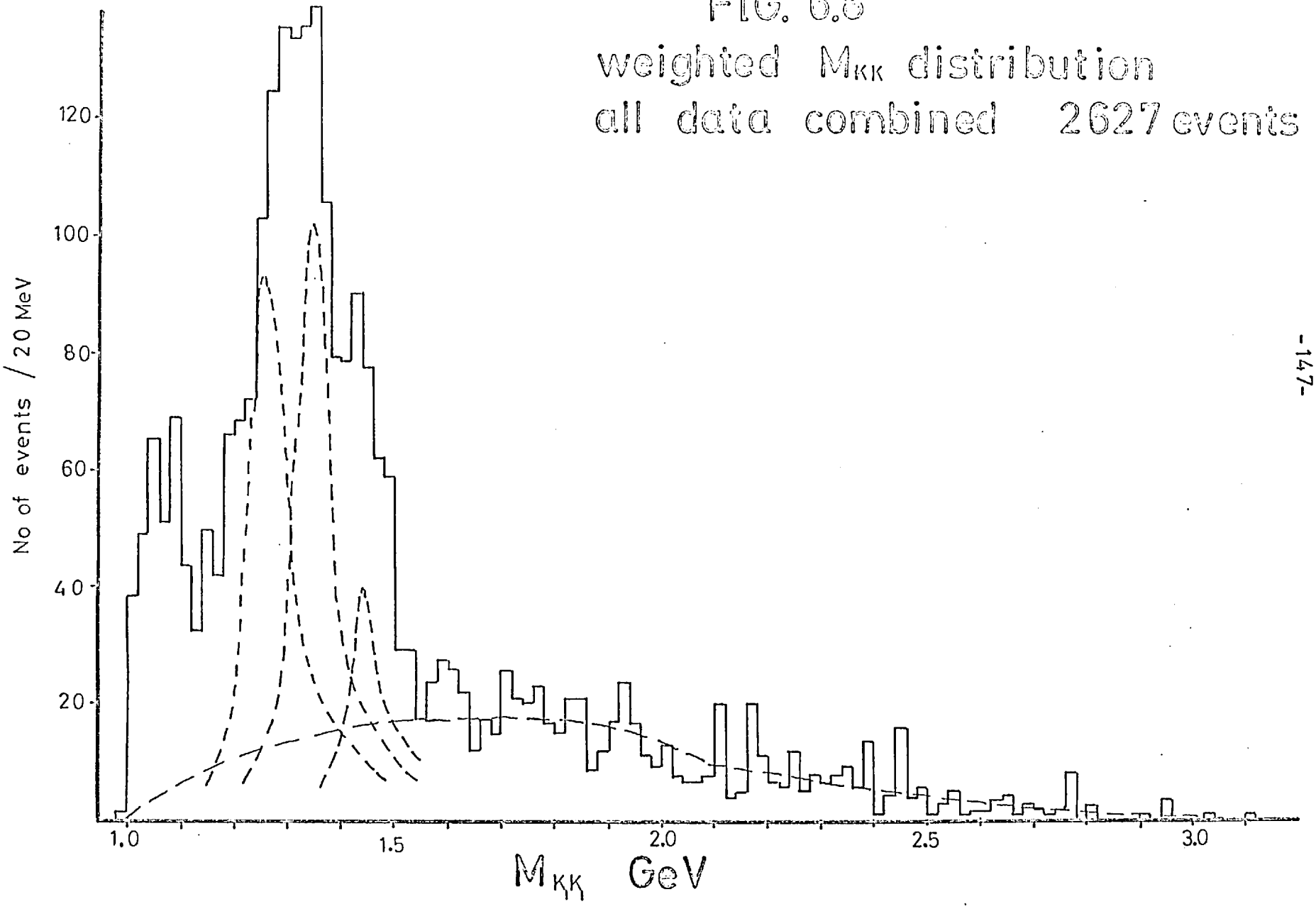

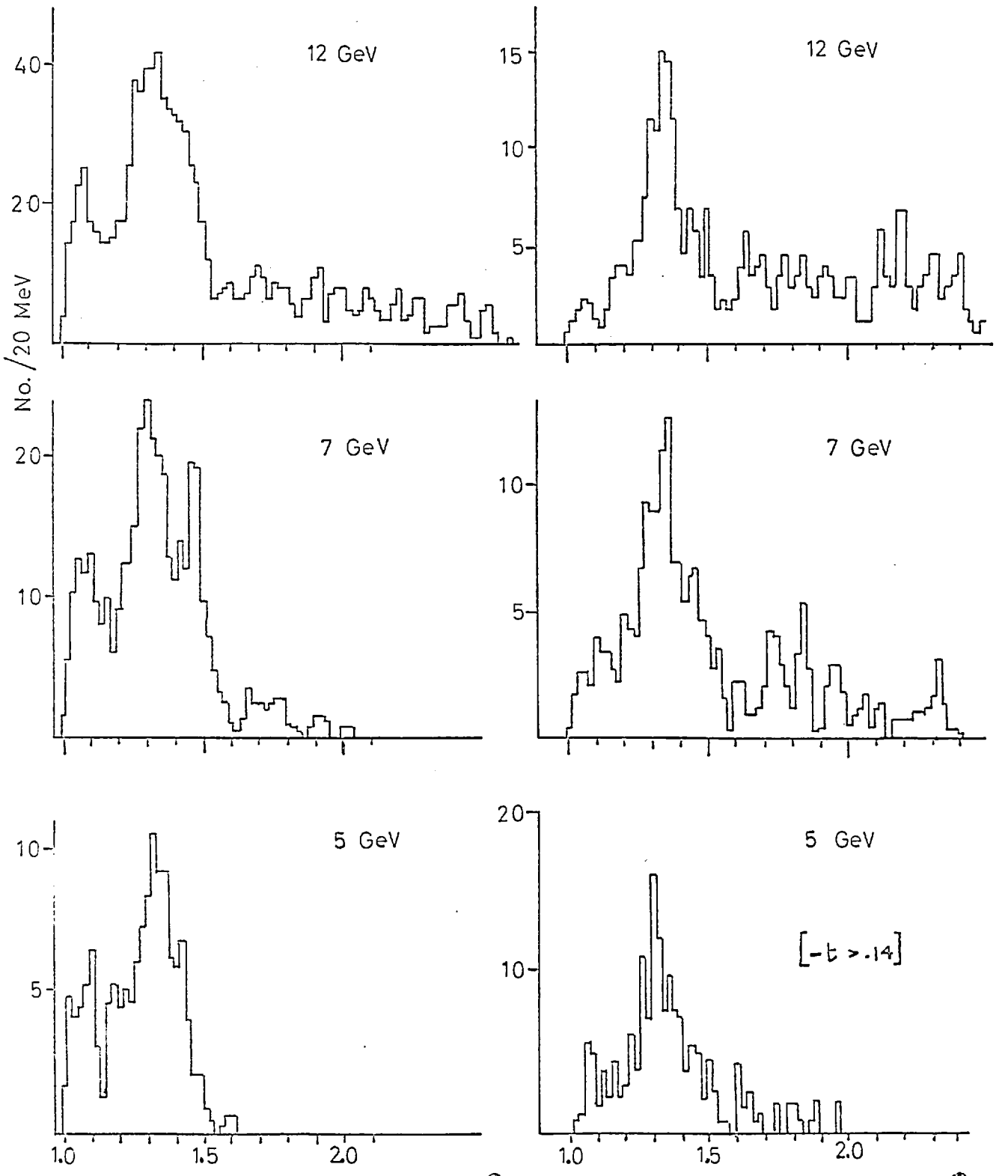

FIG. 6.9 KK mass spectra at high and low 't'

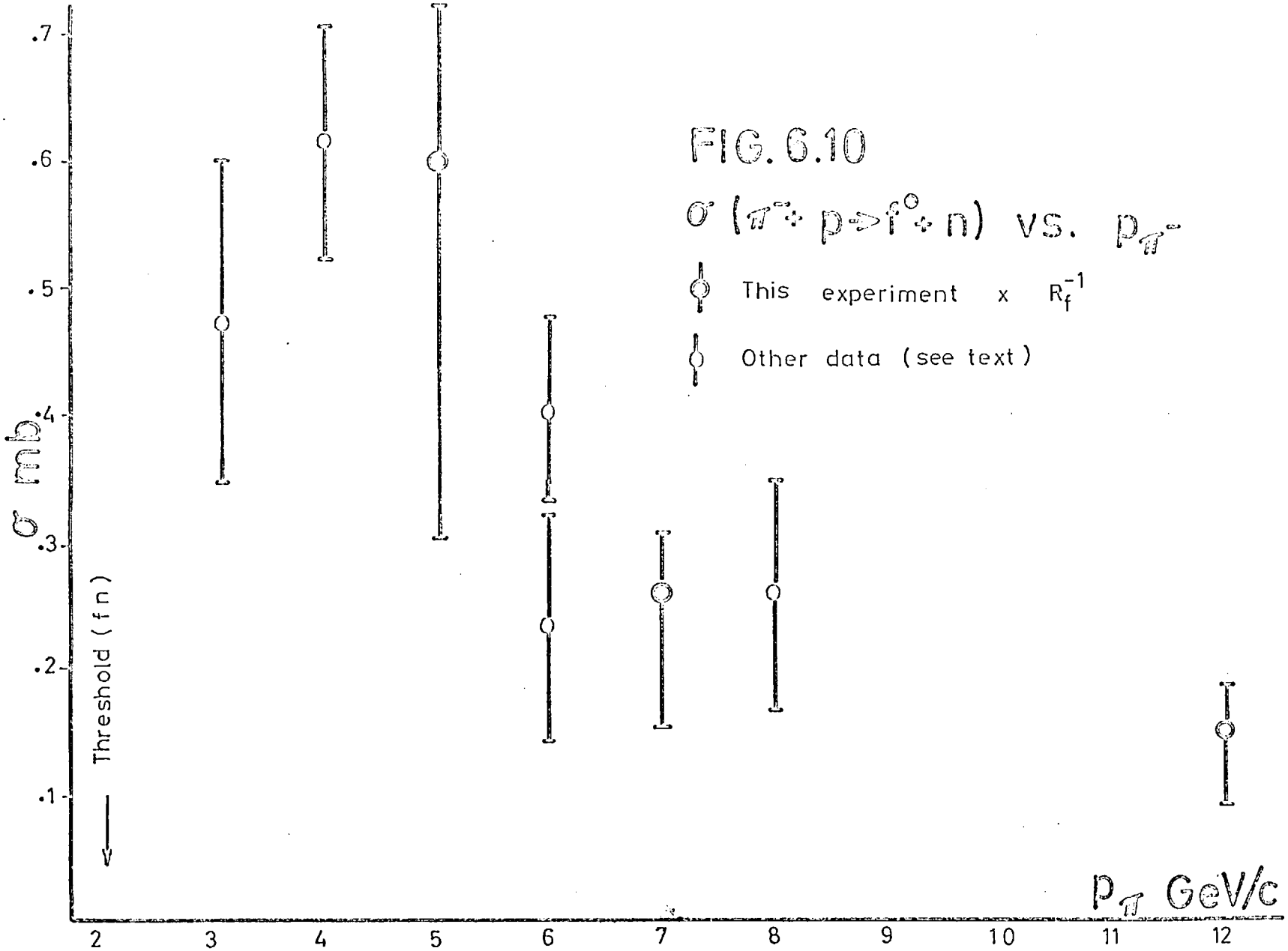

FIG. 6.10

$\sigma(\pi^- + p \to f^0 + n)$ vs. p_{π^-}

This experiment x R_f^{-1}

Other data (see text)

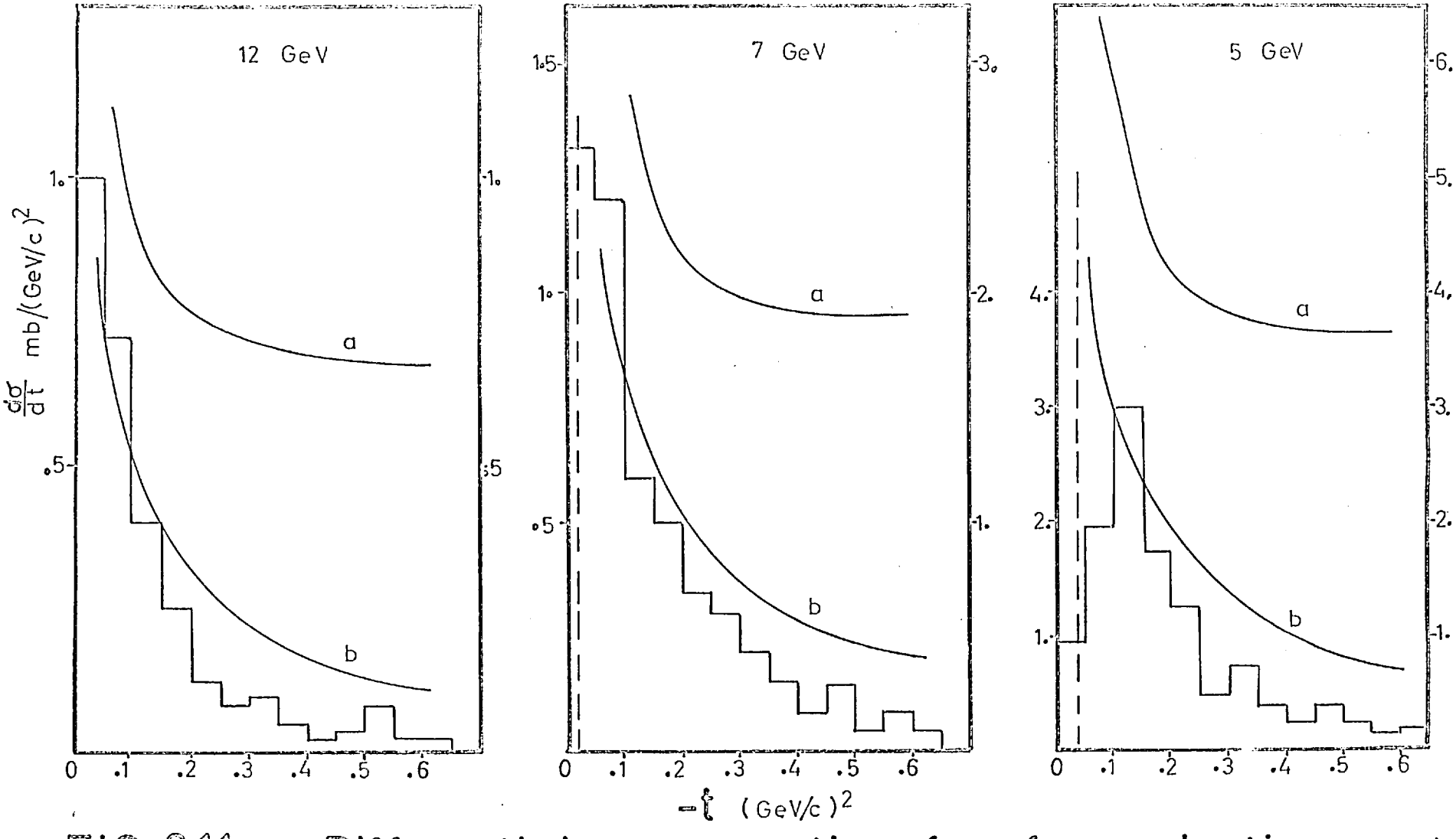

FIG. 6.11 Differential cross-section for f_0 production

COMPARISON WITH (a) BTM and (b) ABSORPTION MODEL (right-hand scale)

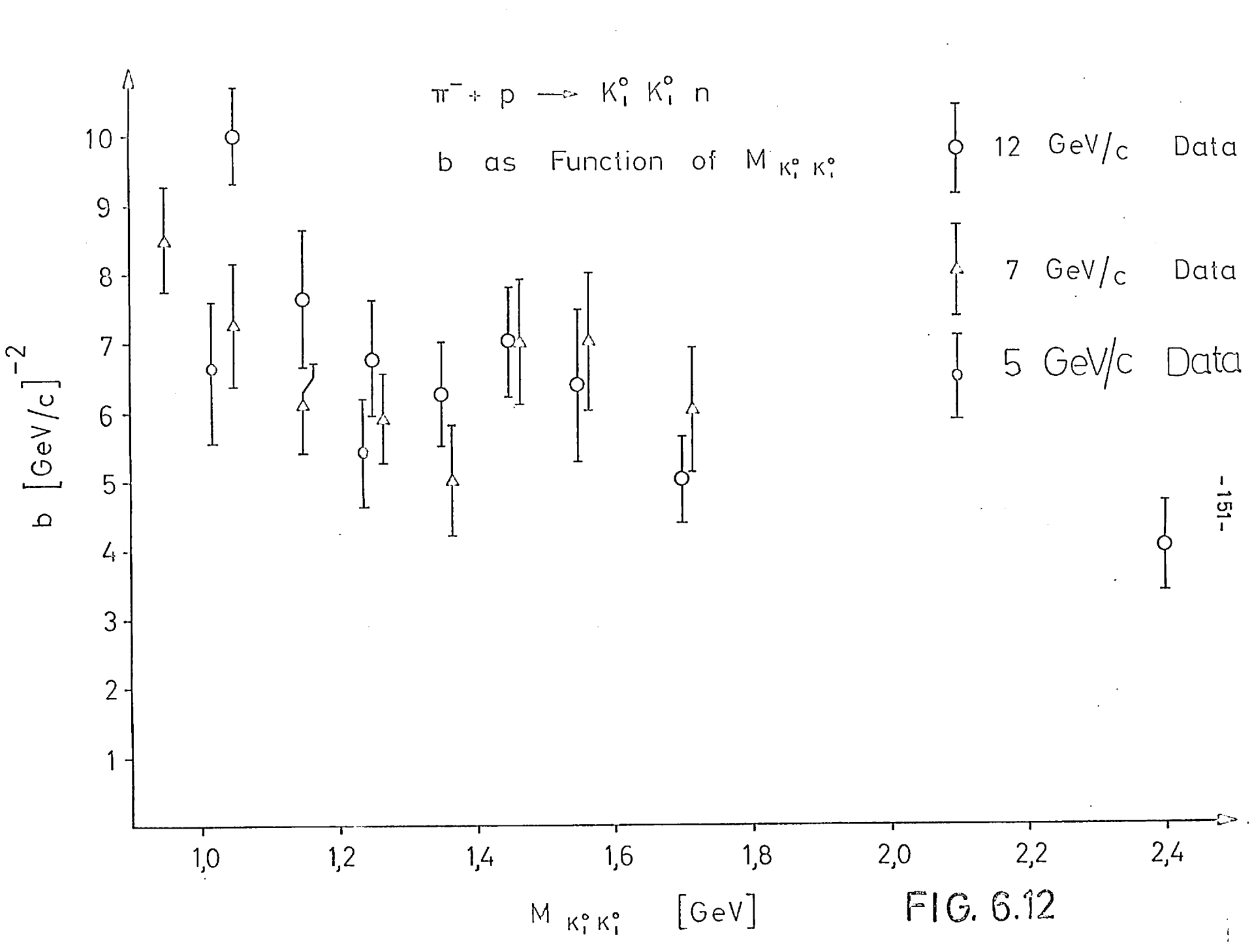
$\pi^- + p \longrightarrow K_1^0 K_1^0 n$
b as Function of $M_{K_1^0 K_1^0}$
12 GeV/c Data
7 GeV/c Data
5 GeV/c Data
b [GeV/c]$^{-2}$
$M_{K_1^0 K_1^0}$ [GeV]
1,0
1,2
1,4
1,6
1,8
2,0
2,2
2,4
1
2
3
4
5
6
7
8
9
10

FIG. 6.12

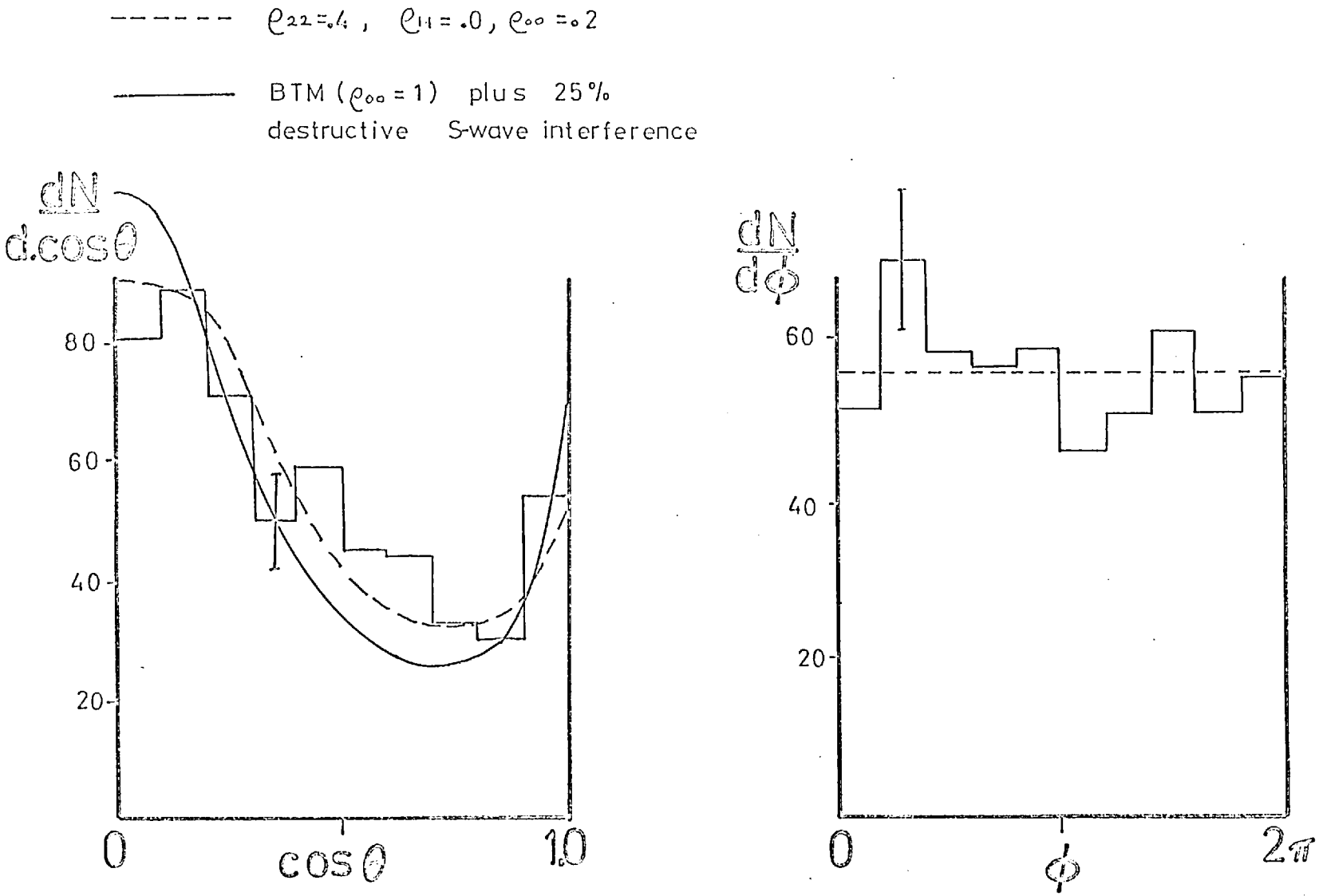

FIG. 6.13 f_0 decay angular distributions

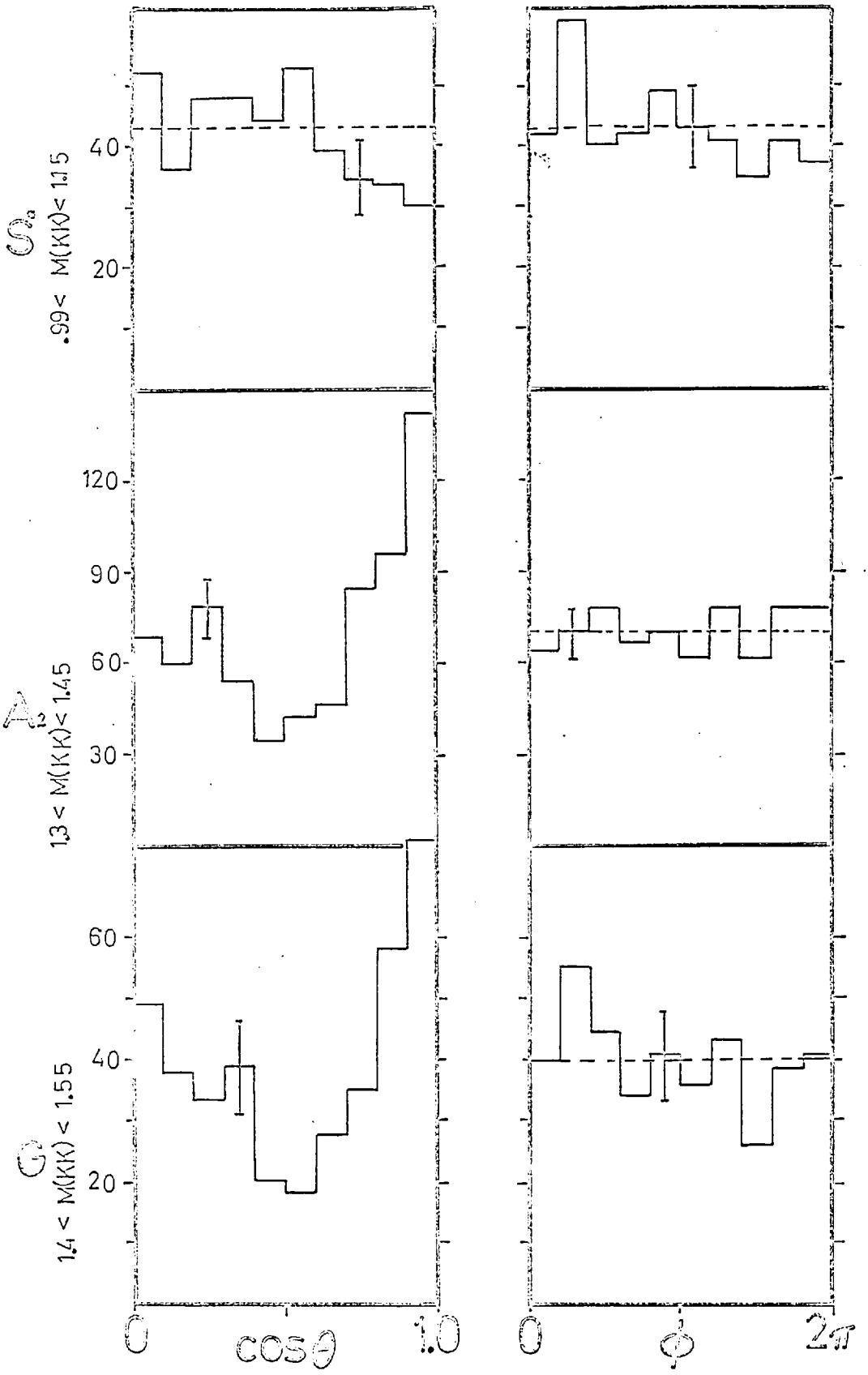

FIG. 6.14 Decay angular distributions

FIG. 6.15

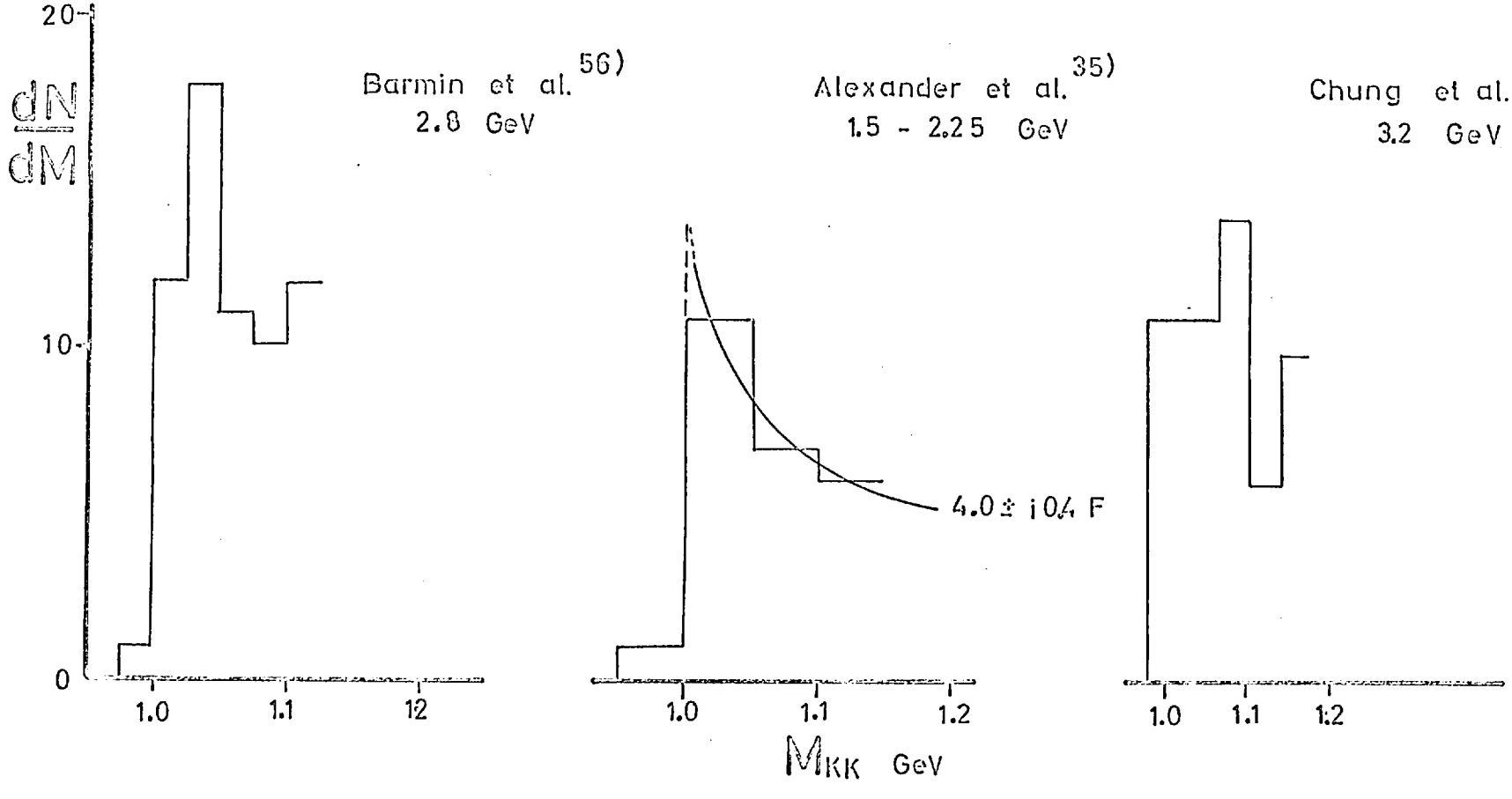

K_1K_1 threshold enhancement - other expts.

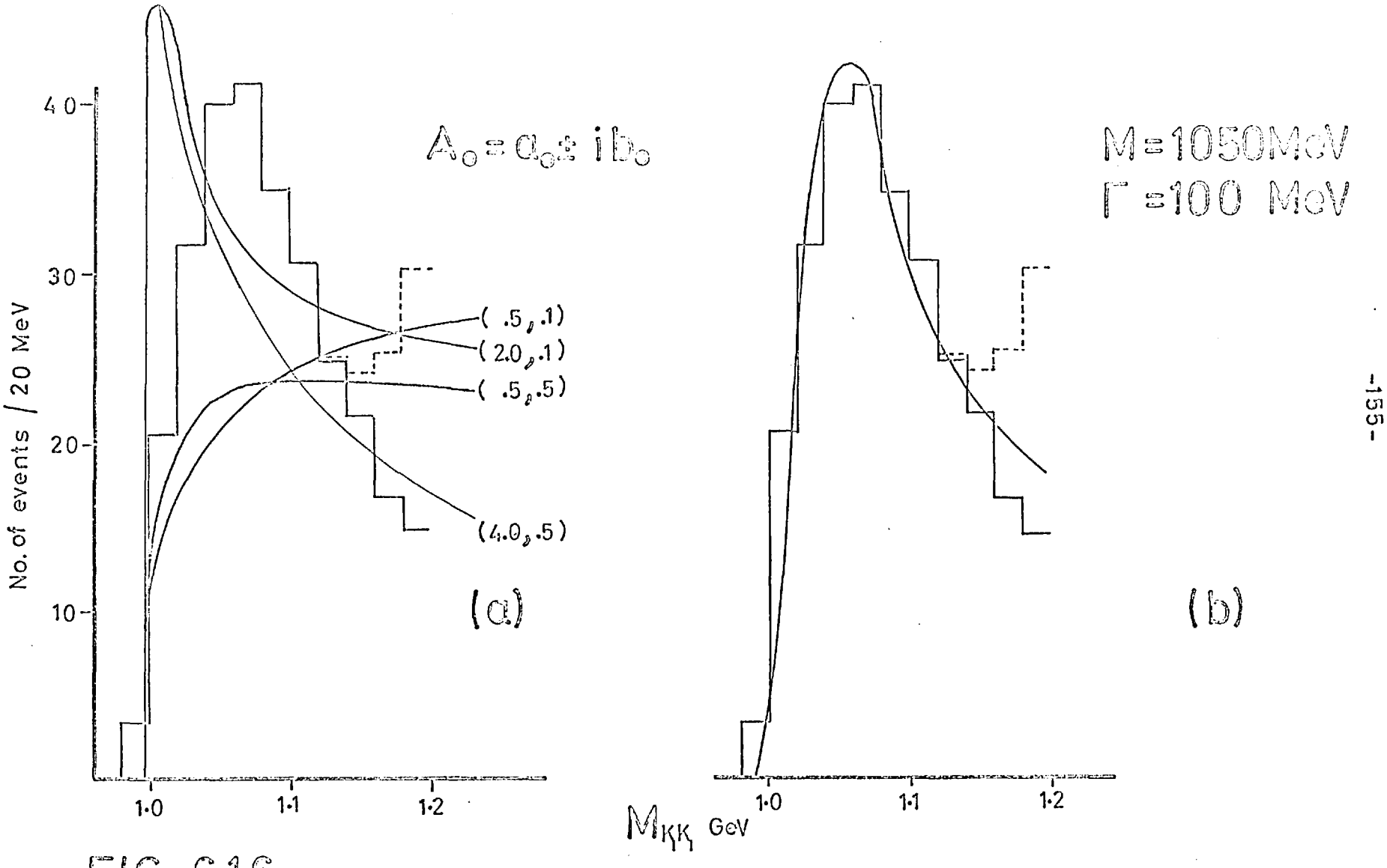

FIG. 6.16 The K_1K_1 enhancement close to threshold
(a) Large scattering length. (b) 0^+ resonance

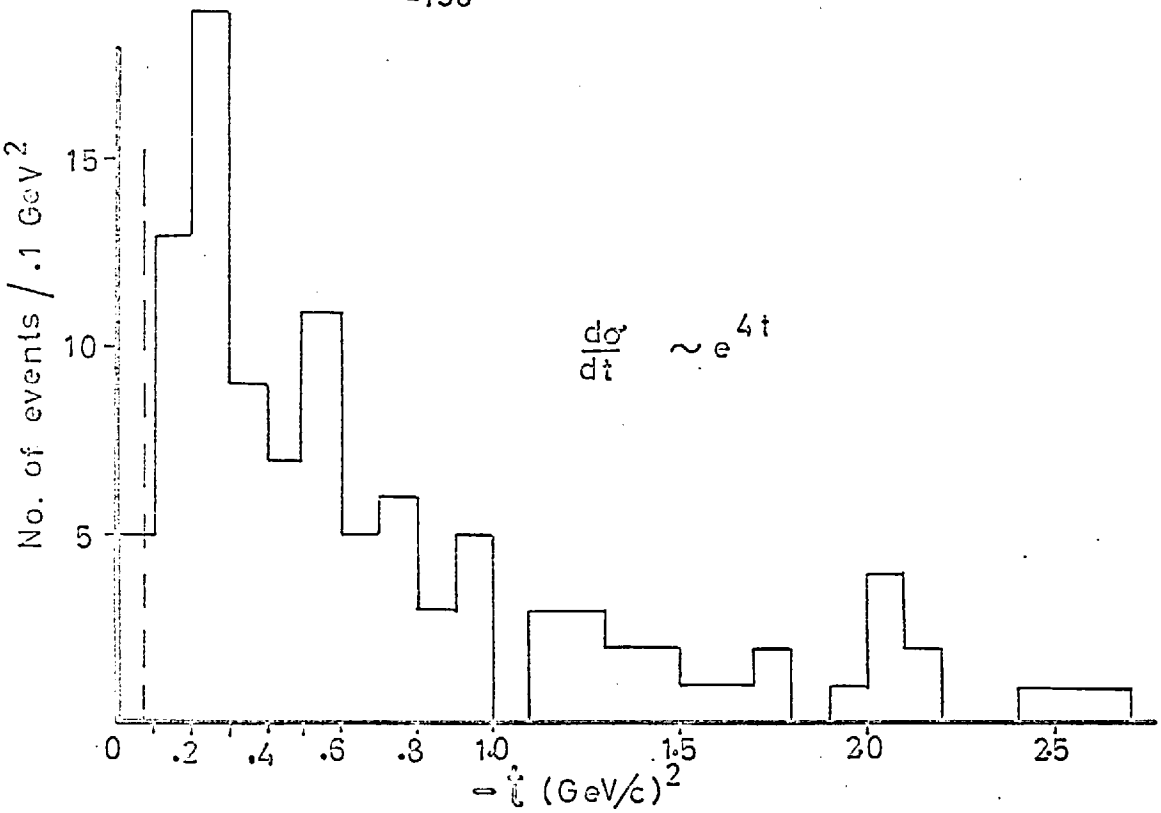

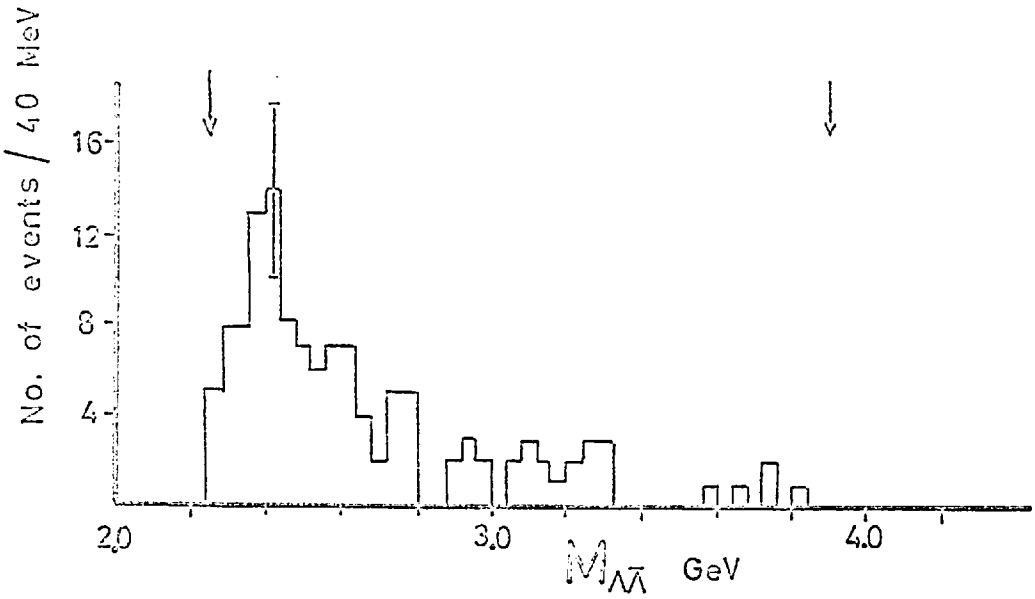

FIG. 6.17 $\pi^- + p \rightarrow \Lambda + \bar{\Lambda} + n$ (127 ev.)

(a) momentum transfer distribution

(b) $\Lambda\bar{\Lambda}$ effective mass

APPENDIX 1

THE MAXIMUM LIKELIHOOD

We consider a continuous variable, x, with a distribution of the form

$$f (x | \alpha_k) \qquad k = 1, \ldots N$$

From a series of M measurements x_m (m = 1, ...M) we require the best value of the N parameters, α_k, which describe the experimental distribution.

The probability that the result x_m be obtained from the m th measurement is simply

$$P_m = f (x_m | \alpha_k)$$

The joint probability for the M measurements is then

$$P = \prod_{m=1}^{M} f (x_m | \alpha_k) = L (\alpha_k)$$

This function of α_k is called the likelihood function. The best estimate of the parameters is obtained by maximising $L (\alpha_k)$. In practice numerical methods are used and it is more convenient to maximise the logarithm of the likelihood function,

$$W (\alpha_k) = \log L = \sum_{m=1}^{M} \log f (x_m | \alpha_k) .$$

APPENDIX 2

THE SPIN DENSITY MATRIX

The spin density matrix provides a convenient description of an incoherent mixture of pure quantum mechanical spin states.

A resonance of spin J in a pure state can be written :

$$\varphi^i = \sum_{m=-J}^{J} c_m^i \mid J , m >$$

and the expectation value of any operator Q is

$$<Q>^i = <\varphi^i \mid Q \mid \varphi^i> = \sum_{mm'} c_m^{i*} c_{m'}^i Q_{mm'}$$

In general the resonance is not in a pure state, but in a mixture of states, each of which occurs with a probability p^i.

The expectation value is now

$$\begin{aligned} <Q> = \sum_i p^i <Q>^i &= \sum_i p^i \sum_{mm'} c_m^{i*} c_{m'}^i Q_{mm'} \\ &= \sum_{mm'} Q_{mm'} \sum_i p^i c_m^{i*} c_{m'}^i \\ &= \sum_{mm'} Q_{mm'} \rho_{m'm} \\ &= Tr (Q \rho) \end{aligned}$$

Defined in this manner ρ is the $2J+1$ dimensional density matrix. The expectation value of any measurement that we choose to perform is determined once ρ is specified. ρ_{mm} is the weight with which the state $\mid J , m>$ is contained in the mixture.

We shall list some of the properties of ρ :

$$\mathrm{Tr}\,(\rho) = 1 \qquad \text{follows from normalisation}$$

$$\rho_{mm'} = \rho^{*}_{m'm} \qquad \text{follows from the definition}$$

$$\rho_{mm'} = (-1)^{m-m'}\,\rho_{-m,-m'} \qquad \text{follows from parity conservation.}$$

In the particular case of interest, $J = 2$:

$$2\,\rho_{22} + 2\,\rho_{11} + \rho_{00} = 1 \qquad \text{and the elements are real}$$

$$\rho_{1,-1} = \rho_{-1,1} \; : \text{ real}$$

$$\rho_{2,-2} = \rho_{-2,2} \; : \text{ real} .$$

APPENDIX 3

THE PERIPHERAL MODEL

i) The Born Term Model

In this appendix we write down some of the useful results[46] obtained by applying the Feynman rules to the diagram below.

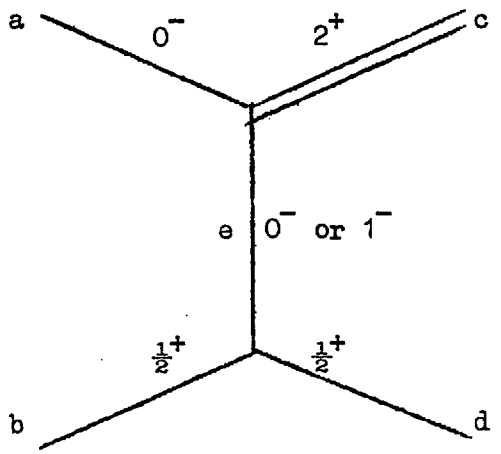

p^{a}_{μ} = 4-momentum of a .

$\varphi_{\mu\nu}$ = the wave function (in momentum space) for spin 2 .

The exchanged particle is pseudoscalar or vector.

The most general couplings at the meson vertex are

(a) $2^+0^-0^-$: $\frac{4g}{m_c} p^a_\rho \varphi^*_{\rho\sigma} p^a_\sigma = C^{PS}$

(b) $2^+1^-0^-$: $\frac{if}{m_c^2} \xi_\mu \varepsilon_{\mu\rho\gamma\delta} \varphi^*_{\rho\sigma} p^a_\sigma p^a_\gamma p^c_\delta = C^V$

and the decay widths for (a) and (b) are

$$\Gamma(a) = \frac{g^2}{4\pi} \cdot \frac{16}{15} \cdot \frac{P^5}{m_c^4}$$

P = 3-momentum of 0^- in rest frame of c .

$$\Gamma(b) = \frac{f^2}{4\pi} \cdot \frac{1}{10} \cdot \frac{Q^5}{m_c^4}$$

Q = 3-momentum of 1^- in rest frame of c .

The amplitudes for transition from initial to final state in the above diagram are

$$M^{PS} = G. \frac{\bar{u}(d)\ \gamma_5\ u(b)}{m_e^2 - t} \cdot C^{PS}$$

$$M^V = \frac{(G_V + G_T)}{m_e^2 - t} \cdot \bar{u}(d) \left[\gamma_\mu + \frac{i2G_T}{(G_V + G_T)} \cdot \frac{p^d_\mu}{m_b + m_d} \right] u(b).C^V$$

The differential cross section

$$\frac{d\sigma}{dt} = \frac{1}{64\pi s\, q^2} \cdot \frac{1}{2} \Sigma \left| M \right|^2$$

where s and q are the (c.m. energy)^2 and the initial state c.m. momentum.

For PS exchange the summation gives

$$\frac{d\sigma^{PS}}{dt} = \frac{G^2}{4\pi} \cdot \frac{g^2}{4\pi} \cdot \frac{8\pi}{3sq^2} \cdot \frac{a_c^4 [(m_b - m_d)^2 - t]}{m_c^2 (m_e^2 - t)^2} \quad \text{.....(A.3.1)}$$

and for V exchange

$$\frac{d\sigma^V}{dt} = \frac{(G_V + G_T)^2}{4\pi} \cdot \frac{f^2}{4\pi} \cdot \frac{\pi}{4sq^2} \cdot \frac{a_c^2}{m_c^4} \cdot \frac{1}{(m_e^2 - t)^2}$$

$$\cdot [[(m_b - m_d)^2 - t]\, a_c^2\, m_c^2 + \tfrac{1}{2}S\,[v^2 - y^2 \cdot \frac{t}{(m_b + m_d)^2}]] \ldots (A.3.2)$$

$y = 2\,G_T/G_V + G_T$ (the bed coupling has vector and

$v = 2 - y$ tensor components)

$S = s\,q^2 q'^2 \sin^2\theta$ (θ = c.m. production angle)

(q' = c.m. momentum in the final state)

The spin density matrix elements can be derived using the helicity representations of the amplitudes [60]. The elements are

(a) For PS exchange :

$$\rho_{00} = 1 \qquad \text{and all others} = 0$$

(b) For V exchange :

$$\rho_{11} = \rho_{-1,-1} = \tfrac{1}{2}$$
$$\rho_{1,-1} = \rho_{-1,1} \quad \text{and is a function of } t :$$
$$\text{all others} = 0 .$$

ii) The Absorption Model

The helicity amplitudes in the Born Approximation, $\langle \lambda_c \lambda_d | B(\theta) | \lambda_a \lambda_b \rangle$, can be developed in a partial wave expansion [60]. The effects of absorption in the initial and final state channels are included by weighting each partial wave amplitude by a factor

$$k(j) = \exp(i\,\delta_i(j)) \cdot \exp(i\,\delta_f(j))$$

The phase shifts, δ_i and δ_f , are determined from the elastic

scattering in the initial and the final states. It is assumed that the elastic cross section can be parametrised by :

$$\frac{d\sigma}{dt}_{el} = \frac{\sigma_{tot}^2}{16\pi} \cdot e^{At}$$

whence $$e^{2i\delta(j)} \sim 1 - C\, e^{-\gamma j^2}$$

$$C = \frac{\sigma_{tot}}{4\pi A}$$

$$\gamma = 1 / 2\, q^2\, A$$

It is usually assumed that the initial and final state elastic scattering parameters are equal. The $k(j)$ ' s are then completely determined. $C = 1$ corresponds to total absorption of the s-wave partial waves.

The effect of the factor $k(j)$ is to reduce the magnitude of the differential cross section, particularly at large values of $-t$. The density matrix elements are shifted slightly (up to $\sim$20 %) from their Born approximation values. They are all, in general, t dependent.

APPENDIX 4

DECAY ANGULAR DISTRIBUTIONS OF J = 0 AND 2 RESONANCES

The polar and azimuthal decay angles are defined in the rest frame of the resonance, c — see Figure 6.6.

$$\cos\theta = \hat{\underline{b}} \cdot \hat{\underline{\alpha}}$$

$$\cos\phi = (\hat{\underline{a}} \times \hat{\underline{c}}) \cdot (\hat{\underline{b}} \times \hat{\underline{\alpha}})$$

$$\sin\phi = (\hat{\underline{b}} \times (\hat{\underline{a}} \times \hat{\underline{c}})) \cdot (\hat{\underline{b}} \times \hat{\underline{\alpha}})$$

The angle ϕ is identical with the Treiman - Yang angle (which is defined in the rest frame of the incident pion).

The decay correlation $W(\cos\theta, \phi)$ is constrained by the conservation of parity in both the production and the decay. Angular distributions for arbitrary J are given in reference 61. We consider here the simplifications introduced if definite production mechanisms are assumed.

i) The decay $0^+ \rightarrow 0^- 0^-$:

$$W(\cos\theta, \phi) = 1/4\pi \quad \text{i.e. isotropic in } \cos\theta, \phi.$$

ii) The decay $2^+ \rightarrow 0^- 0^-$:

$$\begin{aligned} W(\cos\theta, \phi) = \frac{15}{16\pi} \Big[& \sin^4\theta \, (\rho_{22} + \rho_{2-2} \cos 4\phi) + \\ & \sin^2 2\theta \, (\rho_{11} - \rho_{1-1} \cos 2\phi) + 3\rho_{00} (\cos^2\theta - 1/3)^2 - \\ & 4 \sin^3\theta \cos\theta \, (\mathrm{Re}\,\rho_{21} \cos\phi - \mathrm{Re}\,\rho_{2-1} \cos 3\phi) + \\ & 2\sqrt{6}\, \mathrm{Re}\,\rho_{20} \sin^2\theta \, (\cos^2\theta - 1/3) \cos 2\phi - \\ & 2\sqrt{6}\, \mathrm{Re}\,\rho_{10} \sin 2\theta \, (\cos^2\theta - 1/3) \cos\phi \Big] \end{aligned}$$

$\rho_{mm'}$ are the spin density matrix elements.

If we use a Born Term Model to describe the production process and we limit the exchange to spin 0 or 1 all those terms with coefficients ρ_{2m} and ρ_{m2} vanish. Using the results from Appendix 3 we have :

For PS exchange alone

$$W(\cos\theta) = 5/8 \, (3\cos^2\theta - 1)^2 \quad \text{.....(A.4.1)}$$

$$W(\phi) = 1/2\pi \qquad \text{(the Treiman - Yang test)}$$

and for V exchange alone

$$W(\cos\theta) = \frac{15}{16} \sin^2 2\theta \quad \text{.....(A.4.2)}$$

$$W(\phi) = \frac{1}{2\pi} (1 - 2\rho_{1-1} \cos 2\phi) .$$

ACKNOWLEDGEMENTS

I wish to thank Professor C.C.Butler for the opportunity of working in the High Energy Group at Imperial College, and Professor P.Preiswerk for accepting me as a visitor in the Nuclear Physics Division at CERN.

It has been a pleasure to have Dr.J.P.Astbury as my supervisor. His guidance and encouragement, throughout all stages of my work, is most gratefully acknowledged.

The experiment described in this thesis has been performed by members of the CERN - ETH group ; I should like to express my gratitude to those with whom I participated - J.P.Astbury, W.Beusch, G.Finocchiaro, W.Fischer, B.Gobbi, A.Michelini, M.Pepin, E.Polgar, M.Pouchon, U.Valente and C.H.West.

Many others have contributed to the success of the experiment. These include the technicians and scanners at CERN, members of the Data Handling Division and operators of the Imperial College computer unit.

For financial support during the period 1962 - 1965 I thank the D.S.I.R. (now S.R.C.)

REFERENCES

1. A.Rosenfeld et al. Rev.Mod.Phys. 37, 633 (1965) and updated versions of these tables.
2. M.Gellman, Phys.Rev. 125, 1067 (1962)
3. Y.Ne'eman, Nuclear Phys. 26, 222 (1961)
4. S.Glashow and R.Socolow, Phys.Rev.Letters 15,329 (1965)
5. M.Ferro-Luzzi et al. Phys.Letters 12, 255 (1964)
6. CERN - College de France group — data reported at Oxford Int.Conf. on Elem.Part.(Supplement)(1965)
7. L.Durand III and Y.Chiu, Phys.Rev.Letters 14,329 (1965)
8. E.Fermi, Prog.Theoret.Phys.(Japan) 5,570 (1950)
9. See for example : Notes on Phase Space — O.Skjeggestad Proc. CERN Easter School (1964)
10. J.Jackson, Rev.Mod.Phys. 37, 484 (1965)
    G.Lynch et al. Phys.Letters 9, 359 (1964)
11. N.Sopkovich, Nuovo Cimento 26, 186 (1962)
12. K.Gottfreid and J.Jackson, Nuovo Cimento 34,735 (1964)
13. J.A.Newth, Repts.Progr.in Phys. 27,93 (1964)
14. K.Foley et al. CERN Filmless Spark Chamber Conf. CERN yellow report 64-30,11 (1964)
15. M.Vivargent et al. Nucl.Instr.and Methods 22,165(1963)
16. P.Duteil et al. Rev.Sci.Instr. 35, 1523 (1964)
17. C.West, Ph.D.Thesis. University of London (1965)
18. W.Beusch, CERN yellow report 65-21(1965)
19. P.Blackall,B.Powell and P.Zanella, "Spark Chamber analysis with HPD" CERN DD report DD/64 -5 (1964)
    D.Caldwell et al. Proc.Int.Conf.on Elem.Part. Sienna (1963)

20. A.Accensi et al. Phys.Letters 20, 557 (1966)

21. THRESH CERN track chamber programme library

22. GRIND " " " " "

23. A.Borsellino, Phys.Rev. 89, 1023 (1953)

24. J.Christenson, A.Clark and J.Cronin, IEEE Trans.Nucl.Sci. NS-11, 310 (1964)

25. A.Roberts, Int.Symp.on Nucl.Electronics, Paris (1963)

26. B.Rossi, "High Energy Particles" p.68, Prentice-Hall

27. F.Solmitz B.Johnson and J.Day, "Three View Geometry" Alvarez group programming note, p. 117

28. R.Gluckstern, Nuclear Instr.and Methods 24, 381 (1963)

29. V.Cook et al. Int.Conf.on High Energy Phys.CERN p.364(1962)

30. P.Bastien et al. " " " " " " " p.373(1964)

31. C.Peyrou, Aix-en-Provence Conf.Rep. CEN Saclay, 2, 103 (1961)

32. R.Williams, Preprint, Phys.Dept.Univ.of Washington (1966)

33. A.Bigi et al. Nuovo Cimento 33, 1249 (1964)

34. D.Crennell et al. Phys.Rev.Letters 16, 1025 (1966)

35. G.Alexander et al. Phys.Rev.Letters 9, 460 (1962)
A.Erwin et al. Phys.Rev.Letters 9, 34 (1962)

36. U.Maor and T.O'Halloran, Phys.Letters 15, 281 (1965)
R.Deck, Phys.Rev.Letters 13, 169 (1964)

37. J.Jackson, Nuovo Cimento 34, 1644 (1964)

38. G.Goldhaber, Lecture presented at Coral Gables Conf. on Symmetry Principles UCID 2469 (1965)

39. V.Barnes et al. Phys.Rev.Letters 15, 322 (1965)

40. S.Chung et al. Phys.Rev.Letters 15, 325 (1965)

41. Anglo-German collaboration, Phys.Letters 5, 153 (1963)

42. J.Viellet et al. Phys.Rev.Letters 10, 29 (1963)

43. CERN-Ecole Polytechnique and Orsay-Milan-Saclay collaborations Phys.Letters 17, 354 (1965)

44. F.Bruyant et al. Proc.Int.Conf.on High Energy Phys. Dubna p.442 (1964)

45. M.Elitzur et al. Phys.Rev.Letters 17, 420 (1966)

46. H.Hogassen et al. Nuovo Cimento 42, 323 (1966)

47. I.Derado et al. Phys.Rev.Letters 14, 872 (1965)

48. Y.Lee et al. Phys.Rev.Letters 12, 342 (1964)

49. V.Barnes ot al. Phys.Rev.Letters 16, 41 (1966)

50. S.Chung et al. Phys.Rev.Letters 12, 621 (1964)
Saclay-Orsay-Bari-Bologna collaboration, Phys.Letters 15,69 (1965)

51. Aachen-Berlin-CERN collaboration, Phys.Letters 12,356(1964)

52. J.Bronzon and F.Low, Phys.Rev.Letters 12, 522 (1964)

53. R.Armenteros et al. Proc.Int.Conf.on High Energy Phys. Dubna p.467 (1964)

54. R.Hess et al. Proc.Int.Conf.on High Energy Phys. Dubna p.422 (1964)

55. L.Montanet, CERN TC report 66-23 (1966)

56. V.Barmin et al. Preprint No.284 Dubna (1964)

57. G.Chew and F.Low, Phys.Rev. 113, 1640 (1959)

58. See for example Dalitz — Strange Particles and Strong Interactions p. 60, O.U.P.

59. K.Raman Phys.Rev. 149, 1122 (1966)

60. M.Jacob and G.Wick, Ann.of Phys. 7, 404 (1959)

61. K.Gottfried and J.Jackson, Nuovo Cimento 33, 309 (1964)